Hybrid Magnetometers for Unshielded Operation

Kristiaan Kuit

ISBN 978-90-365-3013-2

Hybrid Magnetometers for Unshielded Operation

Combining Hall Sensors with Superconducting Flux Concentrators

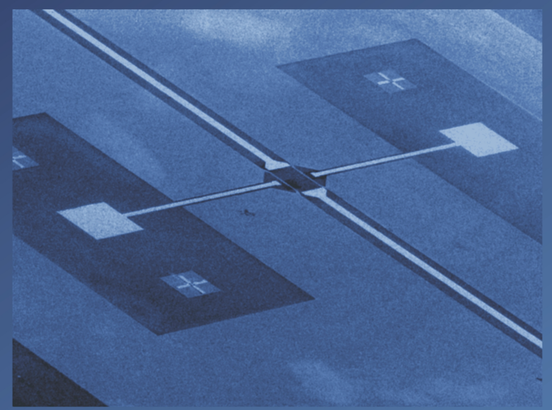

Kristiaan Kuit

Uitnodiging

Hierbij nodig ik u uit voor het bijwonen van de openbare verdediging van mijn proefschrift

op vrijdag 16 april
om 16:45 uur.

De verdediging zal plaatsvinden in zaal 4 van gebouw de Waaier van de Universiteit Twente. Voorafgaand aan de verdediging zal ik om 16:30 uur het proefschrif kort toelichten.

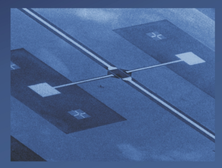

Vanaf 21:00 uur bent u van harte welkom op het feest in café de Pimpelaar op de Oude Markt in Enschede.

Kristiaan Kuit
Cesar Franckstraat 1-I
7557 EA Hengelo (ov.)
khkuit@gmail.com

Paranimfen:
Peter van Kats
Wietse Steffen

HYBRID MAGNETOMETERS FOR UNSHIELDED OPERATION

COMBINING HALL SENSORS WITH SUPERCONDUCTING FLUX CONCENTRATORS

Kristiaan Kuit

Ph.D. committee

Chairman / Secretary	
prof.dr. G. van der Steenhoven	University of Twente
Supervisor	
prof.dr. H. Rogalla	University of Twente
Assistant-supervisor	
dr.ir. J. Flokstra	University of Twente
Members	
prof.dr. P.H. Seidel	Friedrich Schiller University of Jena
prof.dr. P.H. Kes	University of Leiden
prof.dr.ing. B. van Eijk	University of Twente / NIKHEF
prof.dr. J. Schmitz	University of Twente
dr.ing. A.J.H.M. Rijnders	University of Twente

Front cover: Modified scanning electron microscope image of a doped Si hybrid magnetometer with a double concentrator layout.
Back cover: Modified scanning SQUID microscope image showing trapped vortices in thin film superconducting niobium strips.

The research described in this thesis was performed in the Faculty of Science and Technology and the MESA$^+$ Institute for Nanotechnology at the University of Twente. The work was financially supported by the dutch MicroNED program under project number 1-D-2.

Hybrid Magnetomters For Unshielded Operation (Combining Hall Sensors with Superconducting Flux Concentrators)
Ph.D. Thesis, University of Twente
Printed by Gildeprint Drukkerijen
ISBN 978-90-365-3013-2

HYBRID MAGNETOMETERS FOR UNSHIELDED OPERATION

COMBINING HALL SENSORS WITH SUPERCONDUCTING FLUX CONCENTRATORS

PROEFSCHRIFT

ter verkrijging van
de graad van doctor aan de Universiteit Twente,
op gezag van de rector magnificus,
prof.dr. H. Brinksma
volgens besluit van het College voor Promoties
in het openbaar te verdedigen
op vrijdag 16 april 2010 om 16:45 uur

door

Koendert Hendrik Kuit

geboren op 15 april 1981
te Ede

Dit proefschrift is goedgekeurd door de promotor:
prof. dr. H. Rogalla

en de assistent-promotor:
dr. ir. J. Flokstra

Voor mijn ouders

Table of Contents

CHAPTER

1

Introduction

Abstract

Magnetic field mapping of planets and the galaxy has been subject of research for numerous years, starting in the 1950s. Magnetic field sensor configurations on board spacecrafts consist, in most cases, of a vector sensor like a flux gate and a scalar sensor like an optically pumped or free precession magnetometer. Since satellites nowadays are becoming smaller, strong demands on the size weight and power consumption have to be imposed. Hall sensors or giant magneto resistances (GMR) have these properties but do not provide the desired sensitivity. The sensitivity can be enhanced by applying flux concentration by means of a high-T_c flux concentrator. These hybrid devices have been developed with bismuth Hall sensors and GMR's and are showing good sensitivities. The integration of semiconductors and superconductors like a doped Si Hall device and a high-T_c flux concentrator is believed to result in sensitive devices suitable for space applications.

1.1 Magnetism

The physical phenomenon that we nowadays know as magnetism has intrigued mankind since a very long time. The Chinese are reported to be the first to use the naturally magnetized mineral magnetite or lodestone as a compass which aligns itself with the earth magnetic field. These devices were probably not only used for navigation purposes but also to harmonize the buildings in accordance with the principles of the ancient Chinese practice of Feng Shui. There exists disagreement concerning when exactly the compass was invented but reports go back to even 2500 B.C. [1]. Marco Polo (1254 A.D. – 1324 A.D.) is believed to be the one taking this information to Europe in the 13^{th} century. However in the writings of the Greek, Thales (ca 624 B.C. – ca 546 B.C.) already wrote about the power of magnetite to attract iron. William Gilbert (1544 A.D. – 1603 A.D.) was the first one who realized that the Earth itself is in fact a huge magnet. His book, "De Magnete" which was published in 1600, is seen as the first scientific work on magnetism [2]. The relationship between electricity and magnetism was discovered by Hans Christian Ørsted (1777 A.D. – 1851 A.D.) who found that electric current could influence a compass needle. The relation between electricity and magnetism is further found in experiments by Ampère, Gauss and Faraday. Today we know that magnetic fields are widely present in nature which origin can be either from electrical currents or permanently magnetized material. In everyday practice we adopt magnetism to our benefit. Applications of magnetism range in a manner of speaking from refrigerator magnets to particle accelerators and from electric motors to medical applications like magnetic resonance imaging (MRI). If we look to magnetism in a bigger perspective we know that magnetic fields are present on Earth but also in space, the solar system and much further into the galaxy.

1.2 Magnetic Fields in Space

In space there are in principle two types of magnetic fields. On the one hand there are planetary magnetic fields which can be generated due to macroscopic currents in the liquid core or can come from permanently magnetized material in the crust of the planet [3]. On the other hand there is the Sun, also generating magnetic field due to the rapid expansion of its ionized corona [4, 5]. The Sun's magnetic field, carried by the solar wind is called the interplanetary magnetic field (IMF). The planetary magnetic field is interacting with the IMF creating a magnetosphere around the planet.

Planetary magnetospheres can roughly be divided into three groups. Atmospheresless bodies with no intrinsic magnetic field like for example the Earths moon. Bodies with an atmosphere but with a weak or no intrinsic field like Venus or Mars. And the third group, bodies with an atmosphere and an internal magnetic field, strong enough to deflect the IMF far above the surface. Examples of such bodies are Jupiter, Mercury but also Earth.

A schematic representation of the magnetosphere of the Earth is shown in figure

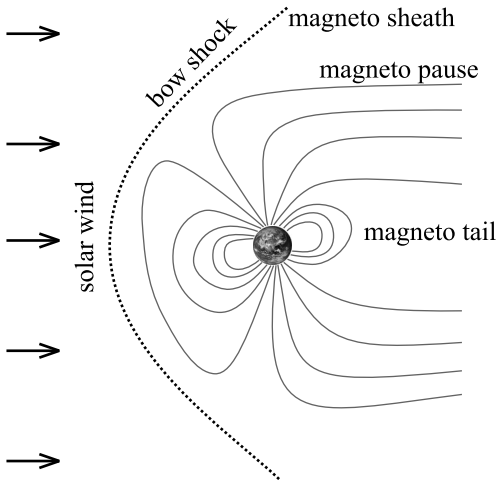

Figure 1.1: Schematic representation of the Earths magnetosphere. This illustrates the interaction between the magnetic dipole field of the planet and the solar wind pressing on the magnetic dipole field on the day side and extending the field on the night side of the planet.

1.1. In the front of the magnetosphere is the bow shock. This is in fact the region where the IMF is deflected from the planets magnetosphere. The bow shock is very similar to the bow wave of a boat as the bow of the ship passes through the water. The bow shock helps to force the solar wind to go around the magnetosphere. The magnetosheath is the region between the bow shock and the magnetopause and has properties distinct from either the solar wind or the magnetosphere, though the plasma and magnetic field observed in the magnetosheath area are clearly of solar origin. Below the magnetosheath is the magnetopause which can be considered to be the end of a planet's region of influence. If there was no solar wind the magnetic field of the planet would look much like a dipole. However the solar wind is pressing on the planets magnetic field causing a flattened part on the day side and a stretched part on the night side of the planet known as the magneto tail. The magnetospheres of dynamo like planets can be very large, much larger than the planet itself. For example the bow shock of the Earth is positioned about 13 earth radii towards the sun. Jupiter for example is a much bigger planet which moreover has a stronger intrinsic magnetic field which results in a magnetosphere 100 times larger than that of the earth [6]. Planets like for example Mars hardly have a magnetosphere. However the Martian magnetic field on the surface of the planet is still interesting as a subject of scientific research showing a probable ancient dynamo which left parts, close to the planets surface, magnetized [7, 8].

There have been numerous space missions exploring the magnetospheres of planets and missions for further investigation are still being planned. Planetary magnetic fields are worth the effort of investigation because it can give insight

into the matter and dynamics deep down. Remanent magnetic field on the surface tells us about the past behavior of the global field. Moreover investigation of the dynamics of dynamo like planets can give insight into the nonlinear chaotic process [3]. Above the planet's surface space missions give insight and understanding of energetically charged particle and plasma measurements from which fundamental information about the environment can be derived [9].

There is also rising interest in the magnetic field of the solar system [10] where the global interaction between the solar wind and the interstellar medium is investigated.

The planetary magnetic field, its magnetosphere or the magnetic field of the solar system can be measured with a magnetic field sensor which is revolved around the planet above the surface or which is launched into deep space. By recording the magnetic field and the position where it is measured a "map" of the planetary magnetic field can be obtained. Such magnetic field mapping started in the 1950s with balloons on Earth and later with rockets orbiting Earth but also with missions into deep space. Mariner 2 was the first spacecraft that performed a fly by at another planet and was launched in 1962. Magnetic field strengths encountered in space vary quite a lot. On Earth the magnetic field is $\sim$50 μT dependent on the position on the planet. The Galileo mission to Jupiter and its moons showed bow shock encounters of $\sim$1 nT while the magnetic field close to the planet surface is $\sim$400 μT [3, 11, 12]. Mars on the other hand has a very weak magnetosphere but locally on the planets surface the Mars Global Surveyor spacecraft measured patchy fields between 10^{-9} – 10^{-4} T [7, 8].

1.2.1 Magnetic Field Mapping in Space

Through the years numerous magnetometer configurations have been flown in space missions and are planned for future missions like the Galileo mission to Jupiter [11], Cassini Huygens to Saturn and its moon Titan [13, 14], Mars Global Surveyor to Mars [15], Ulysses to study the IMF [16], NEAR to the asteroid Eros [17], Messenger to Mercury [18], and Ørsted, CHAMP and SWARM to map the Earth magnetic field [19–22]. The platform for the mentioned space missions are satellites. Besides magnetometers these satellites carry numerous other sensors and steering and readout electronics. Due to the magnetic contamination of the satellites electronics systems, magnetometers are usually mounted on a long boom which can be over 10 m long. The magnetic contamination of the satellite is decreasing with the distance to the spacecraft and is not affecting the magnetic field measurement.

Magnetometers applied in space can be divided into two groups. The first group are the vector magnetometers which are by a large margin the most widely applied. This type of magnetometer not only gives information about the field strength but also on its direction. The device of choice is almost without exception a flux gate magnetometer which is sensitive in a single axis [23]. A vector value is obtained by a tri-axial configuration of 3 flux gates [11, 13, 16–19]. The relative field sensitivity, that means the sensitivity to detect variations in the magnetic

field, is sufficient for most applications. The absolute field accuracy of flux gates is however not always sufficient in typical applications and therefore the device needs to be calibrated. This is usually done with an absolute scalar magnetometer like a free precession or optically pumped magnetometer [13, 16, 20, 21].

A flux gate magnetometer consists of a small magnetically susceptible core wrapped by two coils, a sense coil and an induction coil. An alternating electrical current is passed through the induction coil, driving the core through an alternating cycle of magnetic saturation. This constantly changing field induces an induction voltage on the sense coil which is measured. In zero background field the voltage on the sense coil will match the current on the induction coil. In the presence of the field the saturation of the core is reached easier in alignment with that field and less easily in the opposite direction. This will cause an unbalance in the induction voltage on the sensing coil. Often, this voltage is integrated, yielding an output analog voltage, proportional to the magnetic field. The typical relative field resolution of these devices in space missions is $\sim$5 pTHz$^{-1/2}$ at 1 Hz. Flux gates exhibit zero level drift in time as well as temperature variations. The noise performance is affected by mechanical and thermal stresses which vary over time and with exposure to extreme environments.

As mentioned the device of choice for scalar magnetic field measurements is generally a free precession proton [20, 21] or an optically pumped magnetometer [13, 16]. Both devices rely on the measurement of the Larmor frequency which is linear and absolute dependent on the magnetic field via the gyromagnetic ratio which is known with great accuracy.

In a proton free precession magnetometer a hydrogen rich fluid is exposed to a relatively strong magnetic field causing the protons to align themselves with that field. When the field is switched off and the protons realign themselves with the ambient magnetic field they precess at the Larmor frequency directly proportional to the ambient field.

An optically pumped magnetometer contains a vapor cell filled with helium or an alkali metal gas like cesium or rubidium. The cell is irradiated with light from a discharge lamp or laser at the proper frequency to excite the atoms to a higher energy state. Due to a forbidden transition in the relaxation of the atoms, which becomes overpopulated, the gas cell becomes transparent to the irradiating beam. If the cell is then subjected to a RF-signal with energy appropriate to cause depopulation of this energy level, it will become opaque again and, block the transmission of light at the discharge lamp frequency. The typical noise performance of these two scalar magnetometers lies between 10 – 30 pT$_{\mathrm{rms}}$ over a bandwidth of 0 – 1 Hz.

1.3 Magnetic Field Mapping in Miniaturized Satellites

The evolution of satellites from the early satellites to the current generation shows a strong downscaling in size, weight and power consumption. Due to high launch-

ing costs which depend on the weight of the spacecraft it is desirable to cut on weight and indirectly also on the power consumption because a power consumption requires larger solar panels. This downscaling is showing further progression towards mini, micro, nano or even pico satellites. Qualification in these groups is often made on the weight of the spacecrafts which is typically 100 – 500 kg for mini, 10 – 100 for micro, 1 – 10 for nano and 0.1 – 1 kg for pico satellites. Examples of these miniaturized satellites are already flown nowadays. The Delfi-C3 mission is an example of such a mission. This space craft only weights 2.5 kg and was launched in 2008 [24]. More often a multi-satellite approach is considered which preferably should be launched in a single rocket. An example is the SWARM mission which is a constellation of three satellites, where two will fly at lower altitude, measuring the gradient of the magnetic field, and one satellite will fly at higher altitude. The expectations are that SWARM can measure the Earths magnetic field with unprecedented accuracy [22]. The magnetometers planned for the SWARM mission are in fact heritage from the Ørsted mission which was launched in 1999.

The current generation of magnetometers applied in space missions have sufficient sensitivity for desired applications and should be therefore suitable for applications in micro-satellites. The main drawback of such devices is in the weight and power consumption. The typical weight of a flux gate sensor applied in space missions is ∼0.5 kg with a power consumption of 2 W. The mass and power consumption of scalar magnetometers is even more significant. For example the Overhauser free precession magnetometer of the Ørsted mission weights 1 kg and consumes 4.5 W [20].

Great advances made in semiconductor technology integration techniques like very large scale integration (VLSI) and solid mounted devices (SMD) in the end of the last century make it possible to make smaller, lighter and less power consuming electronics systems for sensor readout [25].

On the sensor side, attempts have been made for miniaturization of flux gates and optically pumped magnetometers. Miniature chip scale optically pumped scalar magnetometers with a micromachined vapor cell filled with ^{87}Rb gas have been developed showing desirable characteristics [26–28]. The typical sensitivity of these devices goes down to 5 pTHz$^{-1/2}$ while the volume of the sensor is only 12 mm^3 and with a dissipation of 195 mW. These magnetometers can also be operated in a special regime where it acts as a vector magnetometer [29] however this only works at very low magnetic fields. Micro vector magnetometers like micro flux gates have been developed which rely on thin film deposition and photo lithography structuring processes [30–32]. Although these devices are smaller, lighter and less power consuming, the sensitity and stability is not sufficient enough with a value of about 25 nT$_{\mathrm{rms}}$ (20 mHz – 10 Hz).

In figure 1.2 an overview of several magnetic field sensors is given with their specific sensitivities and dynamic ranges together with some typical fields in space. Although the lowest field indicated in this graph is the bow shock of Jupiter in general the device sensitivity of space based magnetometers is ∼1 pTHz$^{-1/2}$. A thorough description of all the devices in this figure is given in [33] and in [34, 35]. Some of the sensors in figure 1.2 possess the required sensitivity for application in

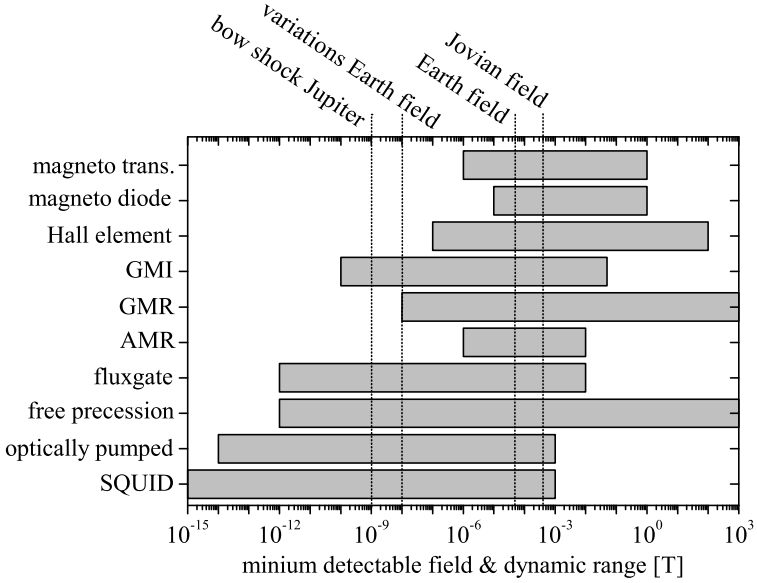

Figure 1.2: Overview of magnetic field sensors sensitivities and dynamic ranges and some typical magnetic fields in space. An extensive overview of all the sensors is given in [33]. The abbreviations stand for magneto transistor (magneto trans.), giant magneto impedance (GMI), giant magneto resistance (GMR), anisotropic magneto resistance (AMR) and superconducting quantum interference device (SQUID).

space.

Especially the superconducting quantum interference device (SQUID), which uses the Josephson effect looks a good alternative at first sight. A distinction should be made between low-T_c and high-T_c SQUIDs based on the critical temperature of the material where the device is constructed from. Low-T_c SQUIDs show unrivaled sensitivity. Due to the fact that these devices are chip based and are therefore small, light weight and moreover have a low power consumption they would be suitable for space. The fabrication of these devices is well developed resulting in good reproducible devices. Nonetheless except for specialized space missions these devices are not the first choice because they require liquid helium cooling and the cooler is heavy and power consuming [36]. The discovery of the high-T_c superconducting cuprate materials [37] in 1986 and later of $YBa_2Cu_3O_{7-\delta}$ (YBCO) [38] implied new possibilities for superconducting sensors in space. Due to reduced refrigeration requirements, high-T_c SQUIDs were proposed as an alternative sensor. Although high-T_c SQUIDs do not possess the sensitity of low-T_c SQUIDs they are still sensitity enough.

However high-T_c SQUIDs were never applied in space missions due to lack of reliability. The deposition of high quality thin films of YBCO on well matching

substrates such as for example $SrTiO_3$ (STO) is rather straight forward. However multiple layers of YBCO like for example YBCO/STO/YBCO for construction of flux transformers are found to be difficult to produce, showing problems with electrical integrity and $1/f$ noise properties. Even quite straightforward junctions like grain boundary junctions are not entirely routine showing irreproducibility due to the variability of the bicrystal substrates [39]. Since only a few sensors are required for operation in a spacecraft a batch of sensors can be produced and the best can be chosen to be actually used. However in space qualification testing the device needs to be cooled down. Since the device is rather vulnerable the warming up can cause a malfunction. This means that after testing there exists an uncertainty if the device will work again in a next cool down. This unreliability is caused by the active elements in the device, the Josephson junctions, which should be improved before it can be applied in space. The superconducting films on the other hand are stable over a long time. So in principle the application of high T_c superconducting sensors in space is possible as long as active elements like Josephson junctions are left out of the equation.

Hall elements for example can be chip based but do not require the desired sensitivity. Hall elements work due to the Hall effect which is the production of a voltage difference (the Hall voltage) across an electrical conductor, transverse to an electric current in the conductor and a magnetic field perpendicular to the current [40]. These devices are generally made of semiconductors or metals with a low carrier density and are widely applied.

The same sensitivity issue holds for giant magneto resistance (GMR) sensors. Giant magneto resistance is a quantum mechanical magneto resistance effect observed in thin film structures composed of alternating ferromagnetic and nonmagnetic layers [41]. The effect manifests itself as a significant decrease in electrical resistance in the presence of a magnetic field.

A way to improve the sensitivity of Hall elements and GMR devices is to apply flux concentration. With this technique the magnetic flux from a certain volume is concentrated at the position of the sensor. Locally the magnetic field is amplified which is improving the sensitivity of the sensor.

1.4 Flux Concentration

Basically two flux focusing techniques can be distinguished. The first technique uses two ferromagnetic plates spaced a small distance from each other [42–44]. The plates attract the magnetic field lines from the vicinity which results in a higher magnetic field in the gap between the plates. The typical layout of such a device is displayed in figure 1.3a). The ferromagnetic plates are shown in gray and the sensor itself in black. The sensor used in this setup should be sensitive in plane like for example a GMR and this is also the sensitive direction of the concentrator plates. A typical configuration is a setup of four identical GMRs in a Weathstone bridge, two in the sensors in the gap and two underneath the concentrator plates shielded from the field. Because all four sensors are identical, operation in a bridge

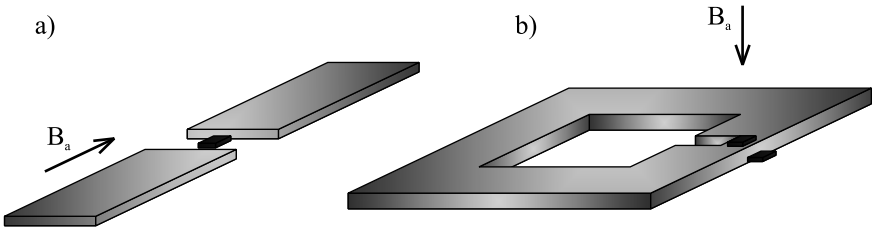

Figure 1.3: The two main principles of flux concentration. a) Ferromagnetic flux concentrators in gray with a sensor in the gap between the plates in black. b) Superconducting ring flux concentrator in gray with a sensor on top or next to the constriction dependent on the sensitive direction of the sensor.

setup cancels temperature influences. Figure 1.3a) shows two rectangular plates, this is an often applied approach but there are also examples where the plates are tapered towards the gap focusing the flux even more [45]. The main drawback is the hysteresis of the device due to complete or partially saturated magnetization. Moreover, the field gain obtained with such a setup is only about one order of magnitude.

The second flux concentration technique is displayed in figure 1.3b). It consists of a high T_c superconducting ring displayed in gray. When a magnetic field is applied all the magnetic field is screened out of the ring by a screening current. The ring contains a narrow constriction where the total screening current is forced through. Due to the local high current density the magnetic field in the vicinity of the constriction is also increased and that is where a sensor can be placed. Dependent on the sensitive direction of the sensor (in plane or perpendicular) the sensor can be placed on top of, or next to the constriction [46–50]. Note that both possible sensor positions are displayed in figure 1.3b). The field gain of such devices is strongly dependent on the desired magnetic field range but can go up to 3 orders of magnitude.

1.5 Motivation

Given the requirements for magnetometry in space missions and in particular in miniaturized satellites like micro-satellites, magnetometers based on a superconducting flux concentrator and a metal or semiconductor sensor are considered to be a good alternative. The resulting hybrid device possesses the desired sensitivity and moreover still contains the properties of low weight and power consumption. The suggestion to integrate high-T_c materials with semiconductors, whose properties such as carrier mobility and thermal conductivity both exhibit maximum values in the same operation temperature region as high-T_c superconducting materials, was posed already in 1992 but did not show any continuation [51]. As mentioned since high-T_c superconducting materials are used, the device cooling is not seen as an unsurmountable problem anymore. Moreover recent developments

in micro coolers are further taking away refrigeration constraints [52]. Hybrid magnetometers with GMR and bismuth (Bi) Hall devices were developed and showed good and promising results. The devices based on the GMR sensors being the device with the best sensitivity. The substitution of Bi to doped silicon (Si) is believed to give orders of magnitude better sensitivity and moreover the possibility to vary the doping density and with that the device sensitivity and resistance.

In this thesis the development of a hybrid magnetometer based on a doped silicon Hall device and and a YBCO flux concentrator is presented. The application of such devices in unshielded environments is investigated. This includes a thorough investigation on vortex trapping in narrow superconducting strips. Hybrid magnetometers with Bi Hall devices are produced. These devices did not show the desired sensitivity however some interesting features on the flux concentrator were observed.

1.6 Thesis Outline

In chapter 2 the operation of flux concentrators in an unshielded environment is investigated. A cool down of the device in such an environment will cause magnetic flux in the form of Abrikosov vortices pinned in the superconducting body. Thermally activated motion of the vortices gives rise to $1/f$ noise [53, 54]. This noise can be reduced by dividing the superconducting body into thin strips. The resulting strips have a certain critical induction below which no vortex trapping occurs, resulting in an ambient field range in which these sensors can be effectively operated. In this chapter a theoretical model for the critical field is derived and experimental verification performed on niobium (Nb) and YBCO strips with a scanning SQUID microscope [55].

In chapter 3 the theoretical properties of hybrid magnetometers are derived. The theoretical temperature dependent carrier density and mobility are used to derive the optimal doping density. Moreover the optimum sensor shape considerations are presented, divided in a part on the sensor, the concentrator and the combination of both.

Chapter 4 deals with the experimental aspects of fabrication. First trials of these devices contained Bi Hall sensor which was later substituted for doped Si. In the introductory part of the chapter an overview of the devices is given with respect to the device fabrication. The deposition of Bi is presented in the first section showing the results of optical inspection of the deposited layers as well as electrical characterization. The two main challenging production steps in the hybrid magnetometer based on the doped Si Hall device is the doping implantation into Si and the deposition of the high-T_c superconductor on Si. In the second section simulations on the doping distribution in Si are presented combined with experimental verification by Hall and resistivity measurements. In the third section the pulsed laser deposition of YBCO on Si is discussed.

In chapter 5 hybrid magnetometers in practice are discussed. This is preceded by a theoretical prediction of the $1/f$ noise contribution due to the thermal move-

ment of vortices in the superconducting body. This is followed by a discussion on the characterization measurements of Bi Hall sensor based hybrid magnetometers. A measurement method to obtain several of the characteristic values is presented after which the actual results are discussed. In the last section the doped Si Hall based devices are discussed.

CHAPTER

2

Vortex Trapping in Thin Film Superconducting Strips

Abstract

Magnetic field sensors constructed from superconducting films, like for example SQUIDs and hybrid magnetometers, which are used in unshielded environments can exhibit higher $1/f$ noise characteristics. This noise is caused by the thermally activated movement of trapped flux vortices in the superconducting body. By dividing the body into narrow strips this noise can be suppressed since the strips have a certain critical magnetic field below which no vortex trapping occurs. A model for the critical field is derived including the pairing energy. Direct experimental testing with a scanning SQUID microscope on $YBa_2Cu_3O_{7-\delta}$ and Nb strips showed excellent agreement between model and measurements. Also a model for the vortex density above the critical field is derived which showed reasonable agreement with the measurements. Statistical analyzes of the trapping distribution revealed trapping in the center of the strips for relatively low inductions and in two parallel rows for higher inductions. The transition magnetic induction corresponds with simulations from literature.

2.1 Introduction

Superconductors are materials which loose all there electrical resistance below a certain critical temperature T_c. Cooper pairs are pairs of two weakly coupled electrons that are responsible for the superconducting behavior. The distance between the electrons in a Cooper pair is given by the coherence length ξ. When a superconductor is brought in a magnetic field it should behave as an ideal diamagnet except for the London penetration depth λ which characterizes the typical distance that a magnetic field can penetrate a superconductor. This means that the magnetic field is expelled from the superconductor which is called the Meissner effect [56]. Not all superconductors behave exactly the same in magnetic fields and they can be divided into two groups, type-I and type-II. The difference between the two types expresses itself in the critical magnetic field of the material. A type-I superconductor has a single critical magnetic field H_c while a type-II material exhibits two critical magnetic fields H_{c1} and H_{c2}.

In figure 2.1 the critical field versus the temperature for a type-II superconductor is displayed. Below H_{c1} in type II and H_c in type I superconductors the material is in the superconducting state and above H_{c2} in type II and H_c in type I superconductors the material is in the normal state. In type-II superconductors there exists an intermediate state between the normal and the Meissner state which is called the mixed state. In this region the superconductor is only partially expelling the magnetic field and is not behaving as an ideal diamagnet. In this regime flux vortices can be trapped in the material. A flux vortex is represented by a magnetic field line of $1\Phi_0$ penetrating the superconductor and thus creating

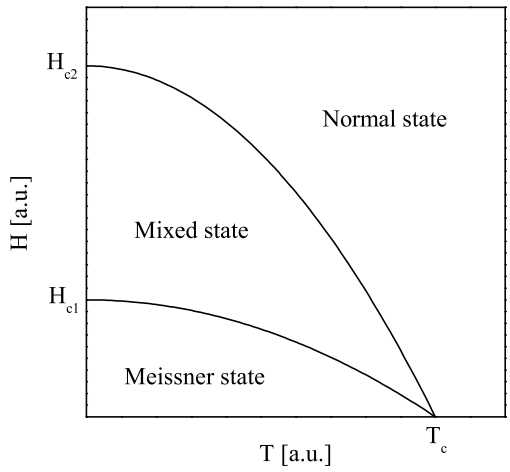

Figure 2.1: Schematic graph of the critical field for type-II superconductors versus the temperature. Below H_{c1} the material is in the superconducting or Meissner state. In between H_{c1} and H_{c2} the material is in the mixed or vortex state and above H_{c2} in the normal state.

a small normal conducting core. Around the field line a circulating supercurrent is flowing which is roughly decreasing exponentially with the distance to the core.

To which group a superconductor belongs is determined by the Ginzburg-Landau parameter $\kappa=\lambda/\xi$. When $\kappa \leq 1/\sqrt{2}$ the material is classified as a type-I superconductor and if $\kappa \geq 1/\sqrt{2}$ as a type-II superconductor [57]. The most commonly used superconductors in electronics like for example Nb, MgB_2 and the copper oxide cuprates are all type-II. The diagram shown in figure 2.1 is in practise much more complicated for cuprate superconductors [58]. In this chapter vortex trapping is discussed that demonstrates itself very close to the critical temperature in relatively weak magnetic fields. This makes the exact content of the phase diagram less important as long one can assume that in a cooldown at the superconducting transition, first the mixed state is entered.

There are a few mechanisims which are responsible for the creation of vortices in superconducting materials like transport currents, magnetic fields and local temperature changes [59]. In practice, real samples have finite size and naturally possess geometric energy barriers that can trap magnetic flux during the cooling process. Moreover samples contain defects and grain boundaries which can pin vortices. Pinned or trapped vortices are nearly always observed in thin-film type-II superconductors, even when cooled in relatively low magnetic fields. Understanding such pinning and trapping effects is important for superconducting electronics applications. The theoretical treatment of vortex trapping is possible for well defined geometries since the energy barriers that play a role can be derived. Theoretical treatment of pinned vortices in defects and grain boundaries is more complex since the resulting energy wells are difficult to theoretically predict. However by analyzes on the vortex spatial distribution it is possible to make an qualitative estimation of the severeness of the defects.

The work in this chapter is motivated by applications of high-T_c superconducting sensors such as superconducting quantum interference devices (SQUIDs) [60] and hybrid magnetometers based on high-T_c flux concentrators [46]. These sensors are used in a broad field of applications, such as geophysical research [61] and biomagnetism [62]. Since in these applications the ambient magnetic field is measured shielding by for example a superconducting can is not possible. The sensitivity of these sensors is limited by $1/f$ noise in such an unshielded environment. The dominant source of this noise is the movement of vortices trapped in the sensor. Noise measurements have been performed on SQUIDs cooled down in a magnetic background field and show higher low frequency noise for higher cool down fields [54, 60, 63]. There are techniques to reduce the noise by introducing artificial pinning cites with for example antidot arrays [64, 65]. Moreover this noise can be eliminated by dividing the high-T_c body into thin strips. The strips have a certain critical induction below which no vortex trapping occurs, resulting in an ambient field range in which these sensors can be effectively operated. Vortex trapping is investigated in thin-film $YBa_2Cu_3O_{7-\delta}$ (YBCO) and Nb strips in order to incorporate the results in a hybrid magnetometer based on a YBCO ring tightly coupled to, for example, a giant magneto resistance (GMR) or Hall sensor.

Models for the critical induction of thin-film strips have been proposed by Clem

[66] and Likharev [67]. Both models show a strip width dependency but differ in the pre-factors and the model proposed by Likharev also has a coherence length dependency. Indirect experimental testing of these models was done by observing noise in high-T_c SQUIDs as a function of strip width and induction [53, 54, 60]. SQUIDs with slotted washers were used in these experiments. Measurements showed a sudden increase of the low frequency noise with increasing the magnetic induction indicating the critical field of the strips in the washer. It should be emphasized that the induction mentioned here is the magnetic induction during cooling, which is the notation from here onwards. More direct experimental verification of these models was presented by Stan et al. [68] using scanning Hall probe microscopy (SHPM) on Nb strips by actually imaging the vortices in the strips. Both experiment and theory found that the critical induction varied roughly like $1/W^2$, W being the strip width. However, the experimental [68] and theoretical [66, 67] pre-factors multiplying this $1/W^2$ dependence differed significantly.

In this chapter a new model for vortex trapping in narrow superconducting strips is derived which takes into account the role of thermally generated vortex-antivortex pairs. To test this model scanning SQUID microscopy (SSM) [55] measurements were performed on thin-film YBCO and Nb strips. Excellent agreement exist between the dependence of critical induction on strip width and the present model for both experiments on YBCO and Nb. In agreement with previous work and as predicted by the model presented in this thesis, it was found that in YBCO the number of vortices increased for inductions above the critical induction linearly with the difference between the applied induction and the critical induction. In a follow-up to the paper of Stan et al., Bronson et al. [69] presented numerical simulations for the vortex distribution in narrow strips. These simulations showed that for inductions just above the critical induction the vortices are trapped in the centers of the strips. For higher inductions the vortices formed more complex ordered patterns, first in two parallel rows, then for higher inductions in larger numbers of parallel rows. Statistical analysis were performed of the vortex distribution in the SSM measurements and agreement was found with this model.

2.2 Theory

Whether or not a vortex gets trapped in a strip is determined by the Gibbs free energy. This energy exhibits a dip in the center of a superconducting strip for applied inductions above a certain critical value. This dip gives rise to an energy barrier for the escape of the vortex. The models proposed by Clem [66] and Likharev [67] differ from the present model only in the minimum height of the energy barrier required to trap vortices.

2.2.1 The Gibbs Free Energy of a Vortex in a Strip

Consider a long, narrow, and thin superconducting strip of width W in an applied magnetic induction B_a. The vortex trapping process occurs sufficiently close to the

superconducting transition temperature that the Pearl length $\Lambda = 2\lambda^2/d$, where d is the film thickness, is larger than W. In this limit there is little shielding of an externally applied magnetic induction B_a. The resultant superconducting currents in the strip can be calculated using the fluxoid quantization condition [70]:

$$\int\int \vec{B} \cdot d\vec{S} + \mu_0 \lambda^2 \oint \vec{J}_\mathrm{s} \cdot d\vec{s} = N\Phi_0. \tag{2.1}$$

In this equation the first integration is over a closed surface S within the superconductor, the second is over a closed contour surrounding S, $\vec{B}$ is the magnetic induction, $\vec{J}_\mathrm{s}$ is the supercurrent density, N is an integer, and μ_0 the magnetic permeability. If we take the strip with its long dimension in the y direction, with edges at $x = 0$ and $x = W$, and an applied induction perpendicular to the strip in the z direction, a square closed contour can be drawn with sides at $y = \pm l/2$ and $x = W/2 \pm \Delta x$. If we assume uniform densities n_v and n_a of vortices and antivortices in the film, with $n = n_\mathrm{v} - n_\mathrm{a}$ being the excess density of vortices over antivortices, the first integral in equation (2.1) becomes $2B_\mathrm{a}\Delta x l$, the second becomes $2J_\mathrm{s} l$, $N = 2nl\Delta x$, and the supercurrent induced in response to the applied induction is:

$$J_y = -\frac{1}{\mu_0 \lambda^2} \left(B_\mathrm{a} - n\Phi_0\right)\left(x - W/2\right). \tag{2.2}$$

The assumption of a uniform density of vortices is good at high trapping densities, and at zero density, but is incorrect at low densities, as will be discussed later. Equation (2.2) differs from the expression given in [66] by the term $-n\Phi_0$: As vortices are nucleated in the film, they reduce the screening currents induced in the film by the applied induction. In the work of Clem zero vortex density is assumed. The equation derived in [66] for the Gibbs free energy of an isolated vortex (upper sign) or an antivortex (lower sign) at a position x inside the strip is then slightly modified as [71, 72]:

$$G(x) = \frac{\Phi_0^2}{2\pi\mu_0\Lambda} \ln\left[\frac{\alpha W}{\xi} \sin\left(\frac{\pi x}{W}\right)\right] \mp \frac{\Phi_0 \left(B_\mathrm{a} - n\Phi_0\right)}{\mu_0 \Lambda} x\left(W - x\right). \tag{2.3}$$

The Gibbs free energy consists of two terms. The first term, which is independent of the applied magnetic induction B_a, is calculated to logarithmic accuracy, as it includes only the kinetic energy of the supercurrents, and it is equal to $\Phi_0 I_\mathrm{circ}/2$, where I_circ is the supercurrent circulating around the vortex. This term, which has a dome shape and decreases monotonically to zero as the vortex reaches a distance $\xi/2$ from the edges of the strip, is also equal to the work that must be done to move the vortex from its initial position at $x = \xi/2$ or $x = W - \xi/2$ to its final position at x against the Lorentz forces of attraction between the vortex and an infinite set of negative image vortices at $-x + 2mW$, $m = 0, \pm 1, \pm 2, ...$ Here ξ is the coherence length, which is assumed to obey $\xi \ll W$. We also assume that the vortex core radius is ξ, such that the constant $\alpha = 2/\pi$ as in [66]. Other values of α, such as $1/\pi$ as in [72], or $1/4$ as in [67] correspond to different assumptions regarding the core size. The second term in equation (2.3) is the interaction energy between a vortex

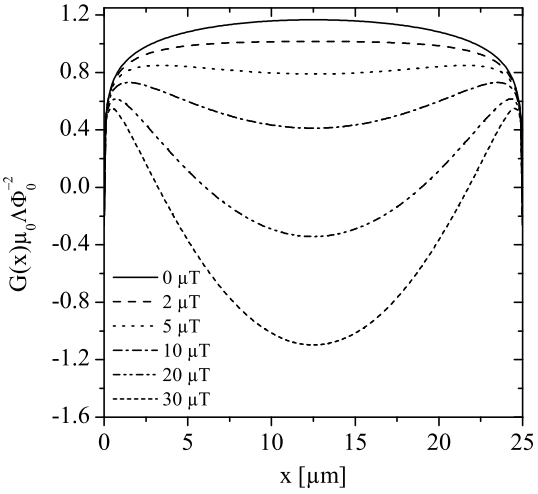

Figure 2.2: Gibbs free energy of an isolated vortex $G(x)$ (in units of $\Phi_0^2/\mu_0\Lambda$) [equation (2.3)] vs. x in a strip of width $W = 25$ μm for applied magnetic induction $B_\mathrm{a} = 0$, 2, 5, 10, 20, 30 μT for $n = 0$ and $\xi = 10.39$ nm.

(upper sign) or an antivortex (lower sign) and the screening currents induced by the external magnetic induction. It is the negative of the work required to bring a vortex (or antivortex) in from the edge against the Lorentz force due to the induced supercurrent given in equation (2.2). The upper sign in equation (2.3) corresponds to the fact that J_y tends to drive vortices into the film, and the lower sign indicates that antivortices are driven out. When B_a is sufficiently large, this term makes a minimum in $G(x)$ in which vortices can be trapped. For wider strips this minimum occurs at lower values of the induction. Equation (2.3) is displayed in figure 2.2 for several applied inductions. In this case $W = 25$ μm and $\xi = 10.39$ nm corresponding to the coherence length of YBCO at the temperature where the vortices are trapped. How this coherence length is obtained is discussed further on in this chapter.

2.2.2 Previous Models for the Critical Induction

There are two existing models which predict the critical induction for vortex trapping when the applied perpendicular magnetic induction is small ($B_\mathrm{a} \sim \Phi_0/W^2$). In these models the Gibbs free energy from equation (2.3) is used in the limit of $n \to 0$. The critical induction model by Likharev [67] states that in order to trap a vortex in a strip the vortex should be absolutely stable. This happens when the Gibbs free energy in the middle of the strips equals zero, which corresponds with the first critical field, and leads to

$$B_\mathrm{L} = \frac{2\Phi_0}{\pi W^2} \ln\left(\frac{\alpha W}{\xi}\right), \tag{2.4}$$

where α is the constant in equation (2.3).

Another model for the critical induction is proposed by Clem [66], who considers a metastable condition. In this view vortex trapping will occur when the applied magnetic induction is just large enough to cause a minimum in the Gibbs free energy at the center of the strip, $d^2G(x)/dx^2 = 0$ at $x = W/2$, leading to

$$B_0 = \frac{\pi\Phi_0}{4W^2}. \tag{2.5}$$

2.2.3 Critical Field Model Including the Pairing Energy

The model proposed here is intermediate between the models presented in [66] and [67]. As the strip is cooled just below the superconducting transition temperature T_c, thermal fluctuations cause the generation of a high density of vortex-antivortex pairs. Similar to the processes determining the equilibrium densities of electrons and holes in semiconductors, the equilibrium densities of vortices and antivortices very near T_c are determined by a balance between the rate of generation of vortex-antivortex pairs, the rate of their recombination, and the rates with which vortices are driven inwards and antivortices are driven outwards by the current J_y. Accordingly, very close to T_c, the densities n_v and n_a of vortices and antivortices equilibrate such that their difference $n = n_v - n_a$ is very nearly equal to B_a/ϕ_0 and the current J_y, see equation (2.2), is practically zero. When $B_0 < B_a < B_L$, it is energetically unfavorable for vortices and antivortices to be present in the strip, and as the temperature decreases and the energy scales of the terms in equation (2.3) increase, the densities of both vortices and antivortices decrease. While vortices and antivortices continue to be thermally generated, the antivortices are quickly driven out of the strip by the combination of the self-energy and field-interaction energy (note the lower sign in equation (2.3)). The antivortex density thus becomes much smaller than the vortex density and becomes so small that the recombination rate is negligible. The value of $n \approx n_v$ drops below B_a/ϕ_0. Although when $B_0 < B_a < B_L$ it is energetically unfavorable for a vortex to be present in the strip, the vortex's Gibbs free energy has a local minimum at the center of the strip and the vortex must overcome the energy barrier before it can leave the strip. Since the energy required to form a vortex-antivortex pair is given by the pairing energy: [73]

$$E_{\text{pair}} = \frac{\Phi_0^2}{4\pi\mu_0\Lambda}, \tag{2.6}$$

the vortex-antivortex pair generation rate is given by a pre-factor times the Arrhenius factor $\exp(-E_{\text{pair}}/k_B T)$, where k_B is the Boltzmann constant. The vortex escape rate is given by an attempt frequency times a second Arrhenius factor $\exp(-E_B/k_B T)$, where E_B is the difference in the Gibbs free energy between the local maximum and the minimum in the center of the strip. Since E_B and E_{pair} have the same temperature dependences because $1/\Lambda$ is proportional to $T_c - T$, the vortex generation rate and its rate of escape will be exactly balanced at all temperatures aside from a logarithmic factor in the ratio of the two pre-factors

when E_{B} and E_{pair} are equal. This occurs at a critical magnetic induction B_{K} which is the solution of the equation

$$\max\left[G(x) - G(W/2)\right] = E_{\mathrm{pair}}, \tag{2.7}$$

which leads to the condition

$$\max\left\{\ln\left[\sin\left(\frac{\pi x}{W}\right)\right] + \frac{2\pi B_{\mathrm{a}}}{\Phi_0}\left[\frac{W^2}{4} - x\,(W-x)\right]\right\} = \frac{1}{2}, \tag{2.8}$$

where the maximum value of the left-hand side of the equation is taken with respect to x. This equation can be solved numerically, resulting in [74]

$$B_{\mathrm{K}} = 1.65\frac{\Phi_0}{W^2}. \tag{2.9}$$

As the temperature decreases, Λ decreases and becomes much less than W. This means that once the vortices are trapped in the local minimum and are clustered around the middle of the strip, the potential well in which they sit changes shape. Recall that the calculation of both terms in equation (2.3) assume that Λ is larger than W. It would not even be possible to magnetically image the vortices in the vicinity of the freeze-in temperature because the local field produced by each vortex is then so spread out. However, as the temperature decreases, the number of trapped vortices per unit length remains fixed and the applied field remains constant. For $n >> 1/W^2$, the distribution of vortices (averaging over the intervortex spacing) takes on a dome-like shape, and vortex-free zones appear at the edges of the strip. The z component of the local magnetic induction should then be described by the equations given in section 2.1 of [75]. The field distribution in a single strip containing a central vortex dome in which the current density is zero is closely related to the field distribution of a pair of parallel coplanar strips with a gap between them [76–78].

In figure 2.3 the Gibbs free energy is plotted for Nb in figure 2.3a) and YBCO in figure 2.3b) for magnetic inductions of $B_{\mathrm{a}} = 0$ and the model values of equations (2.4), (2.5) and (2.9) for 25 μm wide strips with $\alpha = 2/\pi$. The axis on both graphs are the same for better comparison. In the $B_{\mathrm{a}} = 0$ case only the first term of equation (2.3) is playing a role. Due to the difference in coherence length which is $\xi = 320$ nm for Nb and $\xi = 10.39$ nm for YBCO at the temperature where the vortices are trapped, the Gibbs free energy shows a higher dome shape for YBCO. The temperature dependent coherence length at the trapping temperature is determined with the two fluid model which is further discussed in section 2.3.2. For the model values of equation (2.5) and equation (2.9) the parabolic of the second term in equation (2.3) that is subtracted from the dome shape gives the same behavior on the Gibbs free energy. The critical fields for 25 μm wide strips are $B_0 = 2.60$ μT and $B_{\mathrm{K}} = 5.46$ μT. The model values of equation (2.4) are $B_{\mathrm{L}} = 8.24$ μT for Nb and $B_{\mathrm{L}} = 15.46$ μT for YBCO. This makes the energy well for YBCO much deeper. For a matter of fact this is strongly dependent on the strip width.

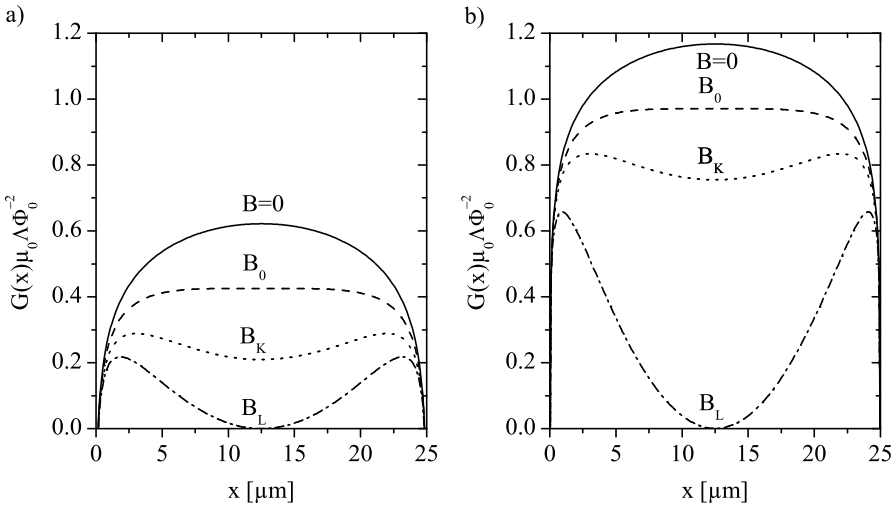

Figure 2.3: Gibbs free energy of an isolated vortex $G(x)$ (in units of $\Phi_0^2/\mu_0\Lambda$) (equation (2.3)) vs. x in a strip of width $W = 25$ μm for $B = 0$ (solid line) and the model values of equation (2.4) (dash dotted line), (2.5) (dashed line) and (2.9) (dotted line) for a) Nb and b) YBCO.

2.2.4 Behavior Above the Critical Induction

Because in the present model the screening current density of equation (2.2) and the Gibbs free energy of equation (2.3) depend on n, the areal density of vortices (when no antivortices are present), we can expect that for applied inductions B_a well above the critical induction B_K the balance between the rates of vortex generation and escape occurs when

$$B_\mathrm{a} - n\Phi_0 = B_\mathrm{K} = 1.65\frac{\Phi_0}{W^2}, \tag{2.10}$$

which can be inverted to give the density n of trapped vortices as a function of applied induction,

$$n = \frac{B_\mathrm{a} - B_\mathrm{K}}{\Phi_0}. \tag{2.11}$$

2.3 Measurements on YBCO and Nb Thin Film Strips

2.3.1 Measurement Setup and Samples

Measurements have been performed on YBCO and Nb thin film strips by means of a scanning SQUID microscope (SSM) [55, 79]. With this measurement technique

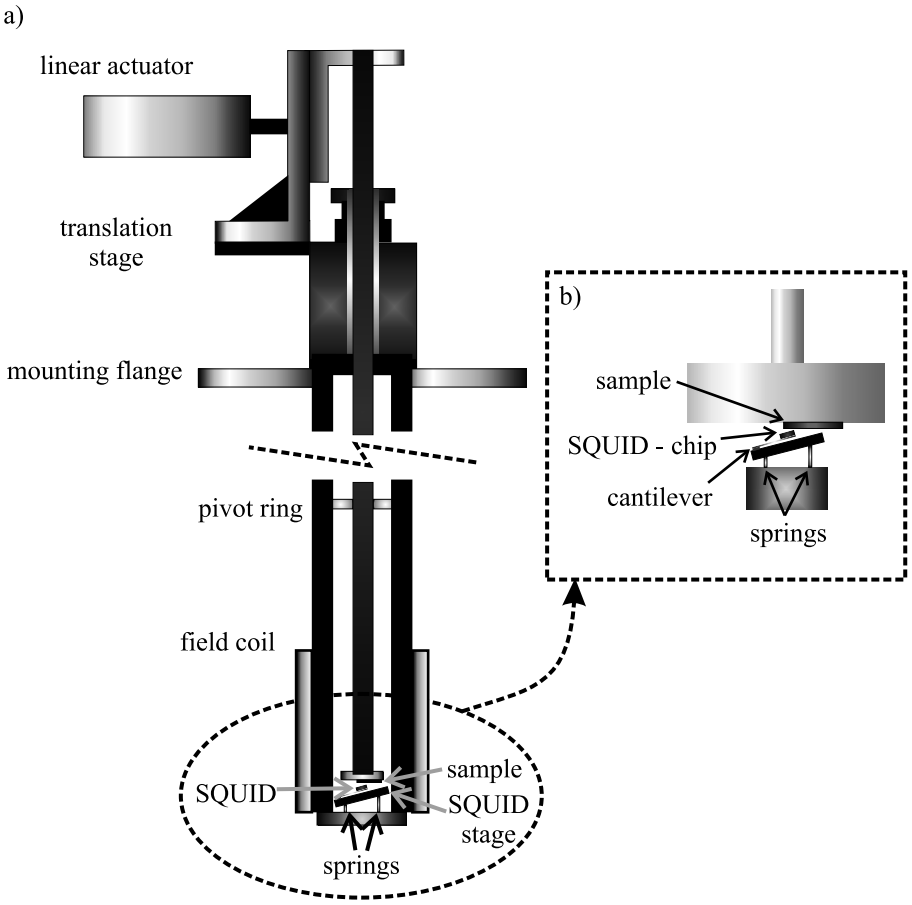

Figure 2.4: Setup of the scanning SQUID microscope. a) General overview of the system with the linear actuator and the transfer of the motion to the sample. b) Setup of the SQUID sensor (adapted from [79].)

a SQUID sensor with a small pickup loop is used to measure the local magnetic induction while scanning the surface of a sample resulting in the spatial distribution of magnetic induction. A schematic overview of the setup is shown in figure 2.4a).

The system is in fact an insert which is placed in a bath cryostat. The part below the mounting flange is in the cryostat with liquid helium and the part above the mounting flange is at room temperature. The linear actuators and a translation stage, which can move in the x, y and z direction, translate the movement to the sample by means of a rod and via a pivoting ring. In figure 2.4b) a magnification of the bottom part of the insert is displayed. On the top part the sample mount is displayed which is connected to the rod. So in practice the sample itself is moving

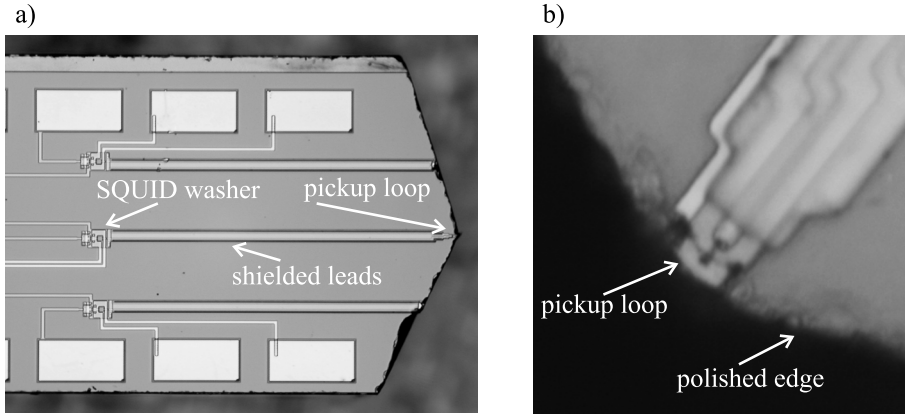

Figure 2.5: Optical images of the SQUID sensor used in the scanning SQUID microscope. a) Overview image showing the SQUID washer, the pickup loop and the shielded connection wires to the coupling coil. b) Magnification of the pickup loop which is defined by focused ion beam milling.

while the SQUID is stationary. On the bottom part the SQUID mount is visible. The SQUID is glued on a flexible cantilever and on a socket which can be tilted upwards to make optimum contact with the sample.

In figure 2.5 optical images of the SQUID sensor are displayed. In figure 2.5a) an overview of the SQUID is shown. There are 3 SQUIDs on a single substrate but in this case only the one in the center is used. The actual SQUID is located at the left. On top of the washer of the SQUID an incoupling coil is placed. The leads extend to the right part of the image and are shielded. On the right at the edge of the substrate is the pickup loop. A magnification of this loop is shown in figure 2.5b). In the image the outermost part of the sample is visible with at the end the pickup loop. The leads that extend to the right upper corner of the image go to the SQUID. The SQUID used in the SSM was made at the Hypres foundry [80]. Due to the minimum line widths possible to make with photolithography in this process the pickup loop still has a significant effective area. To decrease the effective area and hence improve the spatial resolution of the sensor the pickup loop is defined by focused ion beam (FIB) milling and had an effective area of 10-15 μm^2 which was determined during imaging. The substrate of the SQUID sensor is polished in such a way that the pickup loop is completely on the edge of the sample as is shown in both figure 2.5a) and b). As mentioned the SQUID sensor is tilted upwards. By doing this the pickup loop is as close as possible to the sample. Moreover the SQUID itself is not very close to the sample and therefore does not interfere with the measurement.

A magnetic induction perpendicular to the sample was produced by a solenoid coil which was placed around the sample and the SQUID. The desired magnetic induction is applied well above the critical temperatures of the SQUID sensor and the sample and after that both are cooled to 4.2 K. Many different induction values

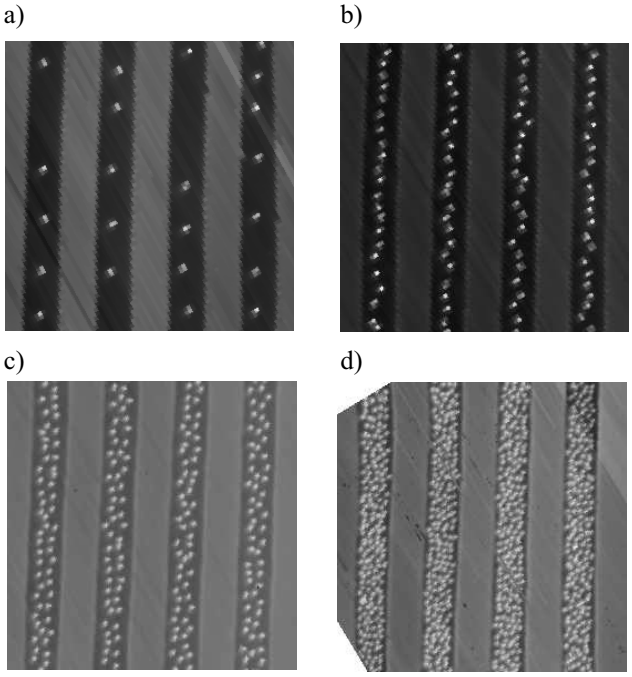

Figure 2.6: Scanning SQUID microscope images of 35μm wide YBCO strips cooled in magnetic inductions of a) 5 μT, b) 10 μT, c) 20 μT, and d) 50 μT.

have been applied to the sample and for every value the sample was warmed up to well above T_c.

Three samples with a pulsed laser deposited 200 nm thin film of YBCO were prepared on an $SrTiO_3$ (STO) substrate. The samples were structured by Ar ion etching. Two samples only contained a single strip width; 6 μm on one sample and 35 μm on the other. These were mainly used in measurements on the vortex density. The third sample contained a wide variety of widths varying from 2 to 50 μm and was mainly used in measurements to determine the critical induction. All deposited films were of high quality with optimized deposition conditions resulting in a high T_c of about 90 K. The critical fields of the samples with the same strip width were in very good agreement.

A Nb sample was made with DC-sputtering on an STO substrate also with a film thickness of approximately 200 nm. This sample was also structured with Ar ion etching into a large variety of strip widths varying from 2 to 50 μm.

In figure 2.6 SSM images are displayed of 35 μm wide YBCO strips for several inductions from 5 to 50 μT. The strips in these images are darker than their surroundings. This difference is caused by a change in the inductance of the SQUID sensor as it passed over the superconducting strip. The bright dots are trapped vortices. As the induction values increase the vortex density also increases

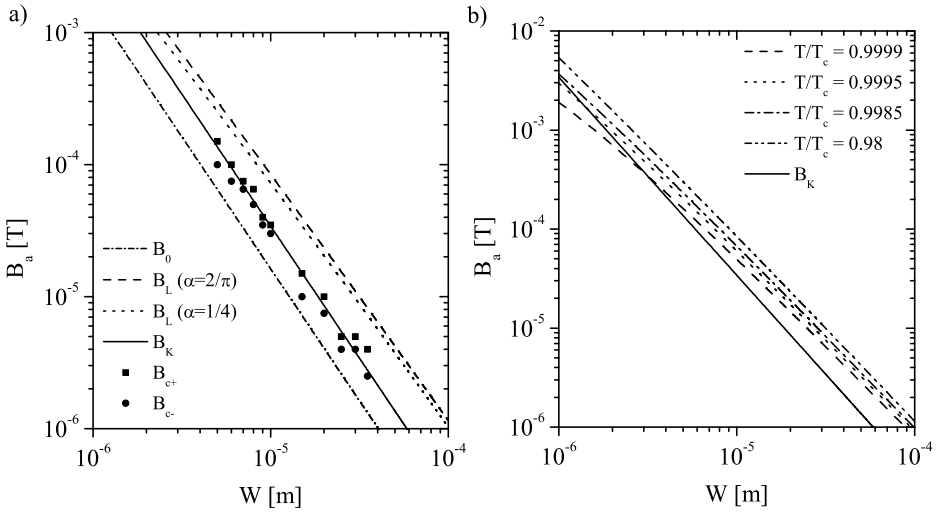

Figure 2.7: a) Critical inductions for vortex trapping as a function of strip width for YBCO strips. The squares represent B_{c+}, the lowest inductions in which trapped vortices were observed, and the dots are B_{c-}, the highest inductions in which trapped vortices were not observed. The dashed-dotted line is the metastable critical induction B_0 (equation (2.5)), the short-dashed and long-dashed lines are B_L (equation (2.4)), the absolute stability critical inductions calculated at a trapping temperature $T_{tr} = 0.98T_c$, with the constant $\alpha = 2/\pi$ [66] or $\alpha = 1/4$. [67] The solid line is B_K (equation (2.9)). b) Variation of the prediction of equation (2.4) (using $\alpha = 2/\pi$) for the vortex exclusion critical induction on trapping temperature (dashed lines). The solid line is B_K (equation (2.9)).

until it becomes difficult to distinguish, by imaging, one vortex from the other like in figure 2.6d). In figure 2.6a) and figure 2.6b) it is clear that at low trapped vortex densities the vortices tended to form one single row in the center of the strip where the energy is lowest. In figure 2.6c) two parallel lines have been formed, but with some disorder.

2.3.2 Critical Induction vs. Strip Width

The critical inductions for strips of YBCO and Nb have been measured on strips varying from 6-40 μm in width. The results of the measurements of the critical induction vs. strip width for YBCO strips are displayed in figure 2.7a) together with the predicted dependencies of the various models. Measurements on strips narrower than 6 μm were unreliable because the critical induction was so high that the operation of the SQUID degraded. The critical induction values for 40 and 50 μm wide strips was smaller than the uncertainty in the applied induction.

There are two data sets in figure 2.7a) for each strip width. The upper set

indicates the lowest induction at which vortices were observed trapped in the strip, and the lower set indicates the highest induction at which vortices were not observed. This provides an upper and lower bound for the actual critical induction. It should be noted that the distance between the data points B_{c+} and B_{c-} is determined by the choice of the induction value applied in this specific measurement and can be decreased by applying more induction values in between. It is apparent from this log-log plot that the critical induction depends on the strip width as a power law. The best chi-square fit of the experimental data to the one parameter power law $B_c = a\Phi_0/W^2$ yielded $a = 1.55 \pm 0.27$. This is to be compared with $a = 1.65$ for the present model of equation (2.9), plotted as B_K in figure 2.7a). It should be emphasized that there were no fitting parameters in plotting B_K.

Comparison of the experiment with the models of equations (2.5) and (2.9) is straightforward, since they are only dependent on the strip width. In order to evaluate equation (2.4) one must make an estimate of the temperature at which vortex freezout occurs because of the temperature dependence of ξ. This dependency is given by the two fluid model expression:

$$\xi(T) = \frac{\xi(0)}{\sqrt{1-(T/T_c)^4}}. \tag{2.12}$$

The trapping temperature T_{tr} for which holds that $T_{tr}/T_c = 0.98$, used in figure 2.7a) for both B_L curves, was calculated by Maurer et al. [81] for YBCO. In addition $\xi_{YBCO}(0) = 3$ nm, a critical temperature of $T_c = 93$ K, and the two-fluid expression for the temperature dependence of the coherence length, result in $\xi(T_{tr}) = 10.39$ nm. Analysis of equation (2.4) shows that a T_{tr} closer to T_c could give better agreement between theory and experiment for some strip widths. However the difference in slopes between theory and experiment becomes larger for higher T_{tr}, making it appear unlikely that this is the correct model for these results. The dependence of the Likharev model predictions on T_{tr} is displayed in figure 2.7b) for $\alpha = 2/\pi$. For lower T/T_c ratios the curve moves further away from experiment. For YBCO is experminentally shown that the two fluid model of equation (2.12) is in fact not valid. The power of the T/T_c term is shown to be ≈ 2 instead of 4 [82, 83]. Evalution of the model values of the B_L curves for the depicted T/T_c ratios in figure 2.7b) and for both power values shows that the spread is larger when the exponent 4 but the curves lie close together and are all significantly different from the model values of equation (2.5) and (2.9).

The results of the measurements of the critical induction vs. strip width for Nb strips are displayed in figure 2.8. The data is organized in the same fashion as in figure 2.7. Also for this material there is good agreement between the measurement and the model values from equation (2.9). The trapping temperature of $T/T_c = 0.9985$ used in this figure for the model proposed by Likharev [67] was experimentally determined by Stan et al. [68] by Scanning Hall Probe Microscopy (SHPM). In the same paper the critical field for Nb strips of 1.6, 10 and 100 μm was measured. Also comparison between these measurements and the model val-

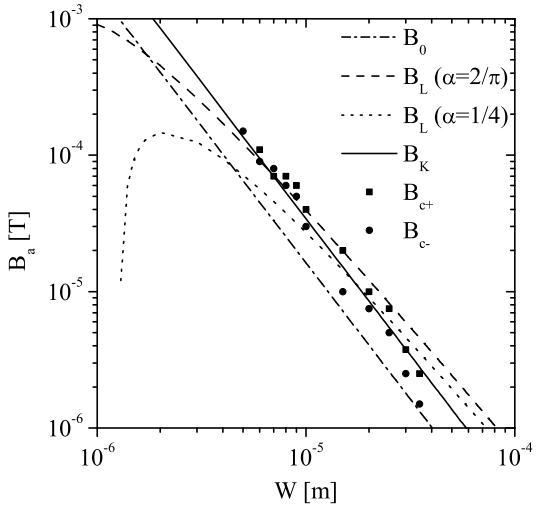

Figure 2.8: Critical inductions for vortex trapping as a function of strip width for Nb strips. The squares represent B_{c+}, the lowest inductions in which trapped vortices were observed, and the dots are B_{c-}, the highest inductions in which trapped vortices were not observed. The dashed-dotted line is the metastable critical induction B_0 (equation (2.5)), the short-dashed and long-dashed lines are B_L (equation (2.4)), the absolute stability critical inductions calculated at a trapping temperature $T_{tr} = 0.9985T_c$, with the constant $\alpha = 2/\pi$ [66] or $\alpha = 1/4$ [67]. The solid line is B_K (equation (2.9)).

ues from equation (2.9) showed good agreement. Using $\xi_{Nb}(0) = 38.9$ nm results in the value $\xi_{Nb}(T = T_{tr}) = 320$ nm used for the B_L curves in figure 2.8. In this case there are some strip widths where there exists agreement between the model values of equation (2.4) and the measurement, however over the whole strip width range the model values of equation (2.9) fit much better. The best chi-square fit of the experimental data to the one parameter power law $B_c = a\Phi_0/W^2$ yields $a = 1.63 \pm 0.42$. This also corresponds with the expected value of $a = 1.65$.

Based on the results on the measurements on YBCO and Nb strips it can be concluded that the critical field only depends on the width of the strip and is independent of the coherence length.

2.3.3 Trapped Vortex Density vs. Applied Induction

In figure 2.9 the experimentally determined density of trapped vortices in YBCO as a function of the applied induction for two strip widths is displayed. This density depends nearly linear on the difference between the induction and the critical induction, with a slope of nearly Φ_0^{-1}. This is in agreement with the work on Nb strips by Stan et al. [68].

The 35 μm strip width data can be fit to a linear dependence of the vortex

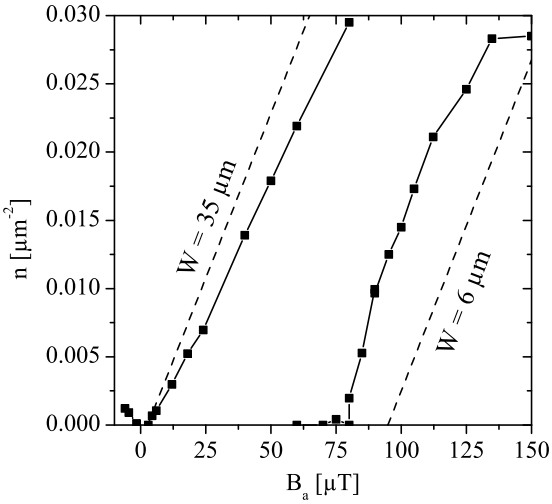

Figure 2.9: Plot of the number density of vortices trapped in YBCO strips 35 μm and 6 μm wide as a function of the applied magnetic induction (squares). The dashed lines are the predictions of equation (2.11), without any adjustable parameters.

density n on B_a with a slope of $(3.86 \pm 0.08) \times 10^{14}$ $(\mathrm{Tm}^2)^{-1} = (0.80 \pm 0.017)\Phi_0^{-1}$, with an intercept of 3.8 ± 1.3 μT. The dashed line in figure 2.9 is the prediction of the present model of equation (2.11) without any fitting parameters. Reasonable agreement exists between the present model and measurements. In the case of the 6 μm strips, there is an apparent saturation in the vortex density for inductions higher than 130 μT. This may, however be an artifact due to the finite resolution of our SQUID sensor. The direction of the applied induction was reversed for three points in the $W = 35$ μm strip data to check for an offset in the applied induction. Such an offset, if present, was small, as indicated by the symmetry of the data around zero induction.

2.3.4 Vortex Spatial Distribution

The local minimum in the Gibbs free energy at $W/2$ of equation (2.3) makes it energetically favorable for vortices to be trapped in the center of the strip. However, as the vortex density increases, the vortex-vortex repulsive interaction makes it energetically more favorable to form an Abrikosov-like triangular pattern. Simulations on the trapped vortex position in strips was described by Bronson et al. [69]. In particular they predict that there should be a single line of vortices for inductions $B_\mathrm{c} < B_\mathrm{a} < 2.48 B_\mathrm{c}$. Above this induction range a second line of vortices is predicted to form. As the induction is increased further additional lines of vortices are predicted to form into a nearly triangular lattice.

The distribution of vortices trapped in the strips at various inductions has been

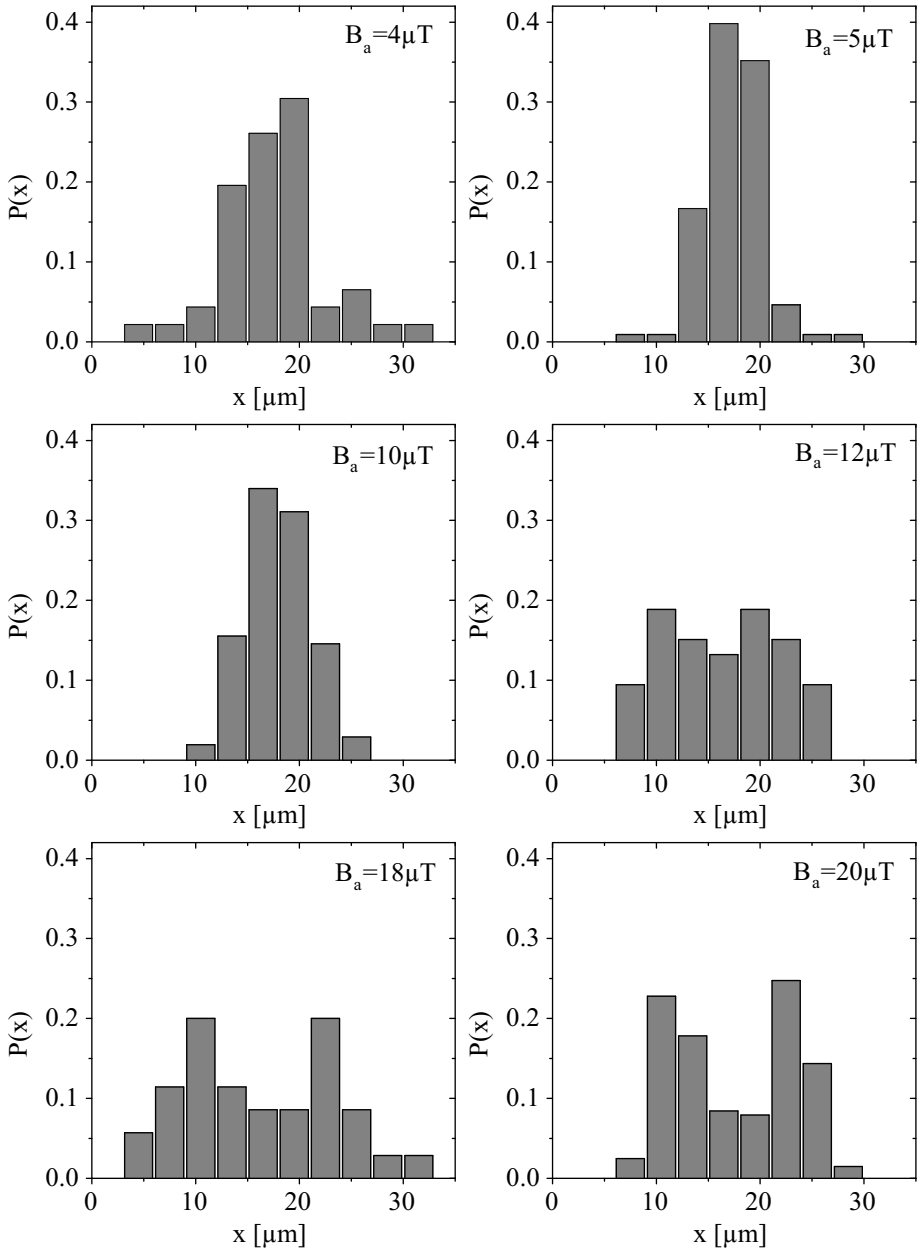

Figure 2.10: Histograms of the probability of trapping as a function of the lateral vortex position in a 35 μm wide YBCO strip at various inductions. At low inductions the vortices are trapped in a single row near the center of the film, but above an induction of about 10 μT they started to reorder. At an induction of 18 μT the vortices were trapped in two relatively well defined rows.

investigated in YBCO as well as Nb. As can be seen from the images of figure 2.6, even though there was significant disorder in the vortex trapping positions, there was also some apparent correlation between the vortex positions. An example can be seen in figure 2.10, where a histogram is displayed of the lateral positions of vortices trapped in the 35 μm wide YBCO strip for several inductions. At low inductions, the vortex lateral position distribution peaked near the center of the film because the vortices were aligned nearly in a single row. At a second critical induction of $B_{c2} = 11 \pm 1$ μT the distribution started to become broader. At 18 μT there were two clear peaks in the distribution, corresponding to two rows. Using the value of $B_c = 3.8 \pm 1.3$ μT for the critical induction of the 35 μm wide strips from the linear fit of the vortex density vs. applied induction curve of figure 2.9, $B_{c2} = (2.89 + 1.91 - 0.93)B_c$ was found. This is consistent with the prediction of $B_{c2} = 2.48B_c$ of Bronson et al. [69]. In the same paper the critical induction for the transition from the two-row to the three-row regime is given to be $B_{c3} = 4.94B_c$. This gives $B_{c3} = 18.77 \pm 6.42$ μT using the same value for B_c. In the measurements no evidence was observed for a three row regime. It was not possible to perform analysis at higher fields than reported here because of limitations to the spatial resolution of the SSM.

Evidence has been observed for longitudinal ordering. In figure 2.11a)-c) histograms are displayed of the longitudinal distances Δy between vortices in the 35 μm wide YBCO strip for various inductions. As expected the inter-vortex spacing distributions became narrower as the inductions increased, since the vortex mean spacings decreased. However the distributions became narrow faster than their means as the induction was increased, indicative of longitudinal ordering, until the second critical induction B_{c2} of approximately 10 μT was reached. At that induction the relative distribution width $\delta(\Delta y)/<\Delta y>$ has a discontinuous jump as a second row starts to form. A similar decrease in the relative longitudinal distribution width with increasing induction is observed in the 6 μm wide YBCO strip, although the spatial resolution of the SSM was not sufficient to resolve vortices at the second critical induction for this width.

In theory there should be longitudinal ordering independent of the magnetic induction. After all, the Gibbs free energy is independent of the position along the strip and the only interaction that plays a role is the interaction between the vortices. Differences in longitudinal ordering as a function of the magnetic induction could arise from local minima of the Gibbs free energy caused for example by defects in the material. For relatively low inductions vortices can easily be trapped in defects since the interaction between the vortices is small because the separation between the vortices is large. For higher magnetic inductions the number of vortices and likewise the interaction between the vortices increases. This could mean that the vortices are more likely to trap at positions determined by the minimization of the vortex-vortex energy than at positions determined by local defects.

To support this theory the distribution in YBCO has been compared with Nb. In figure 2.12 two SSM images are shown from YBCO in figure 2.12a) and Nb in figure 2.12b) at approximately 10 μT. From these images it is evident that the

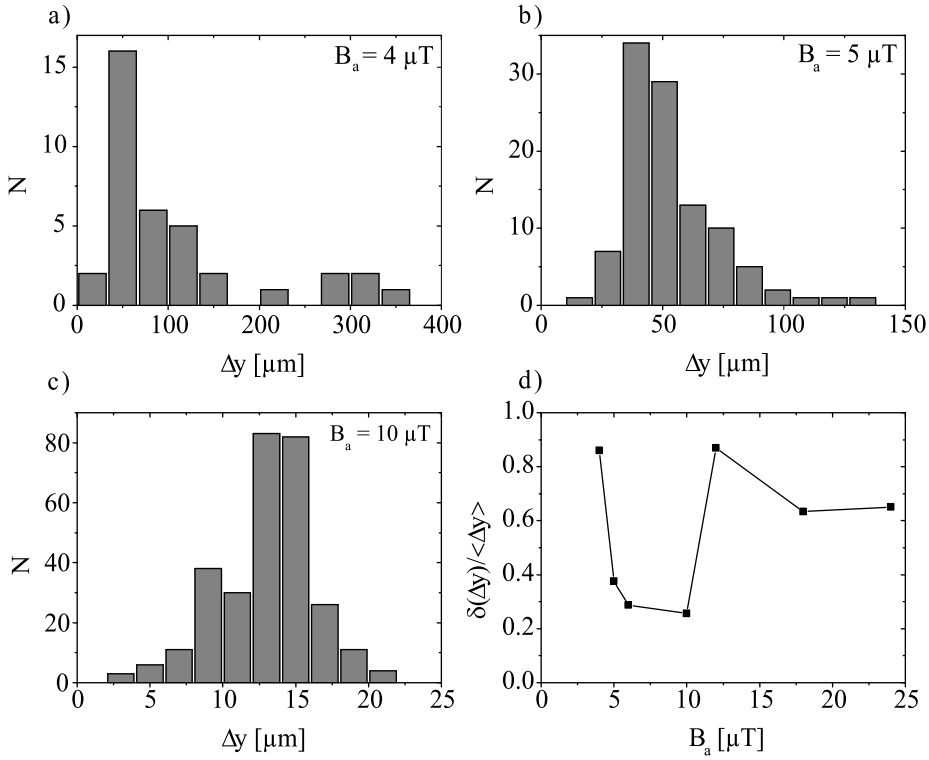

Figure 2.11: (a-c) Histograms of the longitudinal spacing between vortices trapped in a 35 μm wide YBCO strip for selected inductions. (d) Plot of the standard deviation of the distribution of longitudinal spacings, divided by the mean of this distribution, as a function of induction. The relative widths of the distributions became narrower as the induction increases, indicative of ordering in a single row, until at a critical induction of about 10 μT there was an abrupt increase in the relative width as two rows started to form.

ordering of the vortices differs for the two materials. The vortices are more homogeneously distributed in the center of the strips for the Nb strips. Also the spacing along the length of the strip is more homogeneous compared to YBCO. Statistical analyses were carried out in lateral and longitudinal direction to compare the different trapping distributions.

The histograms of the lateral distribution for YBCO and Nb are displayed in figure 2.12c) and figure 2.12d), respectively. Obviously the trapping positions are more narrowly distributed around the center of the strip in Nb. The standard deviation (STD) of the histograms is used to provide a quantitative measure of this distribution. For YBCO and Nb the STDs are respectively 2.58 μm and 1.42 μm. Comparison of the STDs at different magnetic fields showed no field dependency and were always of comparable values. The longitudinal vortex distribution for

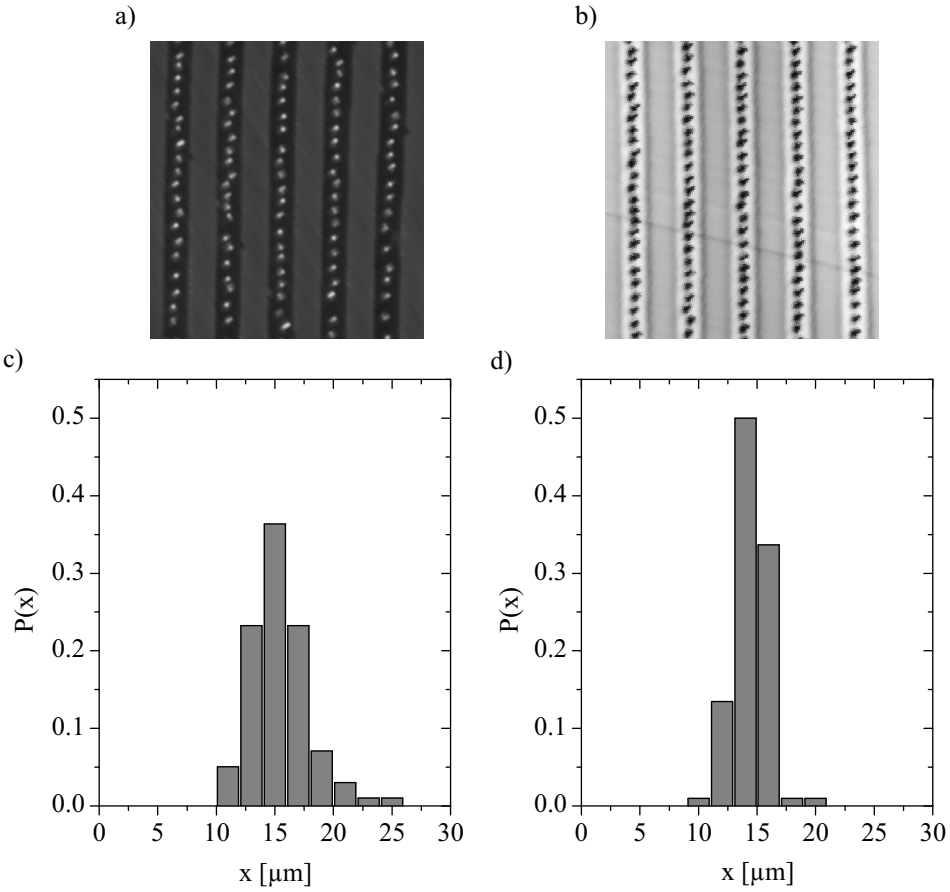

Figure 2.12: SSM images of 30 μm wide strips of a) YBCO and b) Nb cooled down in a magnetic field of approximately 10 μT. The field for the Nb strips was slightly higher than for the YBCO strips. Histograms of the lateral vortex distribution of 30 μm wide strips at 10 μT for c) YBCO and d) Nb. The histogram for the Nb strips is evidently narrower with a standard deviation of 1.42 μm compared to 2.58 μm for the YBCO strips.

the two materials is investigated as a function of the magnetic field. In figure 2.13 the normalized standard deviation versus the vortex density n is displayed [84]. The dataset used in this analysis did not have exactly the same strip width for the two materials. However, when the longitudinal vortex distribution is analyzed versus the vortex density, this is not important. For both materials the longitudinal ordering is improving when the field is increased, which means that the STD is decreasing faster than the average distance between the vortices. For relatively high fields the ordering is better for Nb than for YBCO. For relatively low fields there is not enough data available to draw strong conclusions. As was mentioned

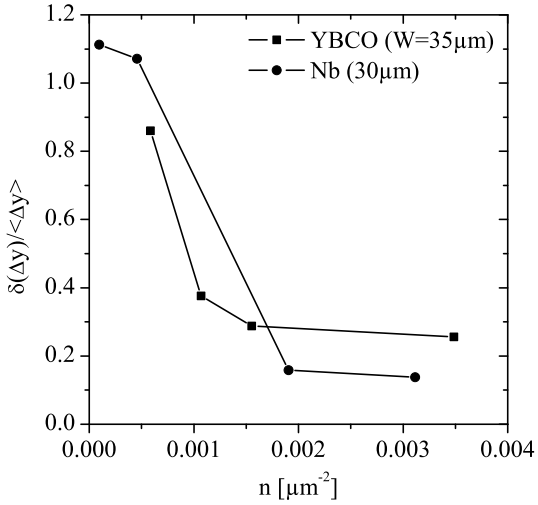

Figure 2.13: Normalized standard deviation of the longitudinal vortex distribution versus the width for 30 μm Nb strips and 35 μm YBCO strips. The normalized standard deviation is the standard deviation divided by the mean distance between the vortices.

previously, the YBCO layer was deposited by laser ablation at a substrate temperature of 780 °C, resulting in a polycrystalline film with domains of ∼200 nm. The Nb film was sputtered at room temperature, also resulting in a polycrystalline film but with smaller domains of ∼20 nm. It is most likely that the combination of smaller grains and larger coherence length leads to larger coupling between the domains in Nb than in YBCO. Therefore a large number of deep additional wells in the Gibbs free energy cannot be expected for Nb. On the other hand, YBCO is a more complex material, which will exhibit more defects and many more deep additional wells can be assumed. This could explain the larger STDs in the YBCO strips in the lateral as well as the longitudinal direction.

2.4 Summary

In this chapter vortex trapping in thin film type-II superconducting strips has been discussed. A new model for the critical magnetic induction above which vortices will be trapped in the strips is derived. In this model the energy required to create a vortex anti-vortex pair is included. Experiments on vortex trapping in narrow YBCO and Nb strips using a scanning SQUID microscope, as well as previous measurements on Nb, [68] showed that the critical induction for the onset of trapping corresponds very good with the predictions by the model. From the Gibbs free energy, the vortex density above the critical field was directly derived. Measurements showed a reasonable fit between model and experiments.

Statistical analyses on the vortex distribution have been carried out. This incorporated the lateral and longitudinal distribution on YBCO as well as Nb strips. The lateral vortex distribution in YBCO strips showed a single row of trapped vortices trapped in the centre of the strip at relatively low inductions and evidence for trapping in two parallel rows for magnetic inductions above a certain second critical induction. The transition induction value corresponded with values found in literature. Analyses on the longitudinal trapping distribution in YBCO and Nb strips showed that the trapping became more homogeneous along the strip as the magnetic induction increased. This suggests that the trapping occurs in defects and grain boundaries for low values of the magnetic induction while the repelling vortex interaction increases and becomes more dominant as the magnetic induction increases. Comparison between the distribution in Nb and YBCO showed a more homogeneous ordering in Nb which can most likely be attributed to growth of Nb in smaller grains combined with the larger coherence length.

The critical field model and the corresponding measurements provides a maximum magnetic field below which SQUIDs and hybrid magnetometers can effectively be operated. These results will be incorporated in the designs of hybrid magnetometers presented in the next chapter. The model and corresponding measurements of the vortex density above the critical field can provide insight in the expected noise when the sensor is operated in an unshielded environment above the critical field. The statistical vortex distribution analyzes are not directly applicable in sensor designs or on its operation but provide a better understanding of the physical properties that play a role in the distribution like the film quality and the material.

CHAPTER

3

Hybrid Magnetometers: Device Theory

Abstract

In hybrid magnetometers the sensitivity of a normal conducting sensor like a Hall element or a GMR sensor is enhanced with a superconducting flux concentrator. A theoretical model for the optimization of the sensor, the concentrator and the combination of both is derived. As a sensor a doped Si Hall device is considered. Parameters like the carrier density and mobility vs. the temperature are investigated. Several dopants are compared and an optimal doping density is obtained where attention is paid to the resulting device sensitivity and resistivity. A double concentrator layout is considered which gives a better coupling to the sensor compared to a single one where both approaches have the same total area. Finite element simulations are used to determine the effective area and total inductance of the resulting rectangular flux concentrators in case of the double layout.

3.1 Introduction

Hybrid magnetometers consist of a normal conducting magnetic field sensor like for example a Hall element or magnetoresistive sensor e.g. a giant magnetoresistance (GMR) coupled to a superconducting flux concentrator. Such sensors can not compete in sensitivity with for example low-T_c superconducting quantum interference devices (SQUIDs) [85] as is shown in figure 1.2. The sensitivity of the device can effectively be enhanced by applying flux concentration, which means that the flux of a certain area is collected and focused on the sensor. Typical fields of application can then be for example non-destructive evaluation (NDE) [47], biomagnetism [86] or space.

The principle of flux concentration is relatively simple. The flux concentrator is a superconducting ring. When a field is applied to the ring a screening current will screen all the field from the ring. A narrow constriction is constructed in the ring through which all the current is forced. At this specific point in the vicinity of the constriction the magnetic field generated by the screening current is higher than the applied background magnetic field and this is where a sensor is positioned. From a sensitivity point of view the size of the concentrator should be maximized, since in this way more flux can be collected, however it should be noted that this also increases the spatial field resolution. For practical reasons the device presented in this thesis is fabricated on a 1×1 cm^2 substrate as will be discussed later in this chapter. The spatial resolution of the device is determined by the effective area of the concentrator and never exceeds the mentioned subtrate dimensions. As discussed in chapter 1, the aimed field of operation of the sensors discussed in this thesis is space and an increase in spatial resolution does not pose a problem.

Reports have been made about a high temperature superconductor Hall magnetometer based on a bismuth (Bi) Hall device and $YBa_2Cu_3O_{7-\delta}$ (YBCO) flux concentrators [46, 47]. These devices can reach a maximum sensitivity of 2.3 VT^{-1} and have a field resolution of 1 nTHz$^{-1/2}$ with a maximum magnetic field of about 18 μT at 77 K. The aimed field of operation for these sensors is in NDE.

Hybrid magnetometers with GMR sensors and with niobium (Nb) or YBCO flux concentrators are other examples of such devices as shown in [48–50, 87]. The device with the YBCO concentrator reported on showed a field sensitivity of 32 fTHz$^{-1/2}$ at 4.2 K which is in the range of high-T_c SQUIDs [86]. At 77 K the same devices reach a sensitivity of about 100 fTHz$^{-1/2}$. The aimed field of operation for this sensor is in the biomagnetism area, especially for magnetoencephalography (MEG).

In this thesis the development of a hybrid magnetometer with a doped silicon (Si) Hall device is presented as an alternative for these designs. Compared to the work of Schmidt et al. [46] doped Si has a higher Hall coefficient compared to Bi. This is beneficial since the sensitivity of the Hall sensor is linearly dependent on the Hall coefficient. Moreover the Hall coefficient can, more or less, be tuned because it is determined by the doping density which can be varied at will.

In this chapter a theoretical derivation of the expected sensitivities and field

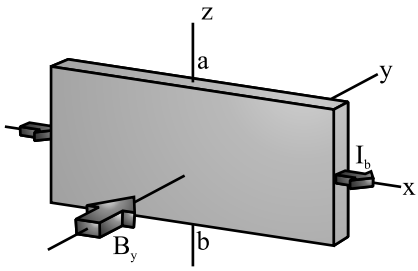

Figure 3.1: Schematic representation of a setup for Hall effect measurements. A bias current I_b is passed through the Hall sensor in the x direction and a magnetic field B_y is applied to the sensor in the y direction. The Hall voltage can be measured between points a and b.

ranges is presented. In the first section the Hall device will be discussed from a material point of view showing the influence of the carrier density and mobility. After that the transition is made to a more practical approach describing the concentrators, the coupling with the sensor and the sensor shape considerations. A comparison between a single concentrator and a double concentrator layout is shown and the sensitivity of the device is presented.

3.2 Hall Effect in Semiconductors

Hall devices are well known magnetic field sensor which are used in a wide area of applications. The Hall effect was discovered by Edwin Hall in 1879 [40] and describes the generation of a electric potential across a current conducting strip in a magnetic field. In this section the Hall effect will be treated in order to come to the application in doped silicon Hall devices.

If we consider the situation as shown in figure 3.1 of a long current conducting strip, with current I_b, in a magnetic field B_y, a voltage can be measured across the strip between a and b given by:

$$V_\mathrm{H} = \frac{I_\mathrm{b} B_y}{ned} = R_\mathrm{H} \frac{I_\mathrm{b} B_y}{d}. \tag{3.1}$$

Here d is the thickness of the strip, n the carrier density and e the unit charge. The carrier density and unit charge can be rewritten to the Hall coefficient which is given by $R_\mathrm{H} = (ne)^{-1}$. In the case of Hall effect in semiconductors the Hall coefficient is positive for hole type and negative for electron type carriers. If the current is carried by both electrons and holes the Hall coefficient is given by:

$$R_\mathrm{H} = \frac{p\mu_\mathrm{p}^2 - n\mu_\mathrm{n}^2}{e(p\mu_\mathrm{p} + n\mu_\mathrm{n})^2} \tag{3.2}$$

for electron density n and mobility μ_n and hole density p and mobility μ_p [88].

The resistance of the device between the current contacts is given by:

$$R = \frac{\rho l}{bd} \tag{3.3}$$

where ρ is the specific resistance of the material, b the width and l the length. In the general form, when one assumes that there are both n and p type carriers the specific resistance is:

$$\rho = \frac{1}{e(n\mu_{\mathrm{n}} + p\mu_{\mathrm{p}})}. \tag{3.4}$$

The carrier density in semiconductors depends strongly on the temperature and is determined by the dopant material, dopant density and the temperature by the relations:

$$n \approx \frac{2N_{\mathrm{D}}}{1 + \sqrt{1 + 4\frac{N_{\mathrm{D}}}{N_{\mathrm{eff}}^{\mathrm{C}}} e^{E_{\mathrm{d}}/k_{\mathrm{B}}T}}}, \tag{3.5}$$

$$p \approx \frac{2N_{\mathrm{A}}}{1 + \sqrt{1 + 4\frac{N_{\mathrm{A}}}{N_{\mathrm{eff}}^{V}} e^{E_{\mathrm{a}}/k_{\mathrm{B}}T}}}, \tag{3.6}$$

where N_{D} and N_{A} are the density of impurity atoms and E_{d} and E_{a} the ionization energies respectively for donors and acceptors. $N_{\mathrm{eff}}^{\mathrm{C}}$ and $N_{\mathrm{eff}}^{\mathrm{V}}$ are the partition function for translational motion in three dimensions given by:

$$N_{\mathrm{eff}}^{\mathrm{C}} = 2\left(\frac{2\pi m_{\mathrm{n}}^{*} k_{\mathrm{B}} T}{h^2}\right)^{3/2} \tag{3.7}$$

$$N_{\mathrm{eff}}^{\mathrm{V}} = 2\left(\frac{2\pi m_{\mathrm{p}}^{*} k_{\mathrm{B}} T}{h^2}\right)^{3/2} \tag{3.8}$$

where $m_{\mathrm{n}}^{*} = 0.26 m_0$ and $m_{\mathrm{p}}^{*} = 0.39 m_0$ are the effective electron and hole mass respectively in Si, m_0 being the mass of a free electron. The relations of equations (3.5) and (3.6) hold for typical impurity concentrations in which the individual donors, in n-type, or acceptors, in p-type materials, do not influence each other. Secondly it is assumed that these are pure n-type or p-type semiconductors, so the concentration of other impurity types than the one considered is assumed to be small. At high temperatures the intrinsic carrier concentration becomes dominant but this is not included in equations (3.5) and (3.5). However, this device will be operated at 77 K which is far below the temperature where the intrinsic carriers outnumber the dopant carriers.

In figure 3.2a) the model values of equations (3.5) and (3.6) at 77 K are displayed. For the low doping range all materials show the same behavior with $n = N_{\mathrm{D}}$ or $p = N_{\mathrm{A}}$, which is called the saturation range. For higher doping levels the so-called freeze out region is entered where not all the impurity atoms are contributing to the carrier density. The increase in carrier density in this region goes with $\approx \sqrt{N_{\mathrm{A}}}$ or $\approx \sqrt{N_{\mathrm{D}}}$ dependent on the doping type. The differences between

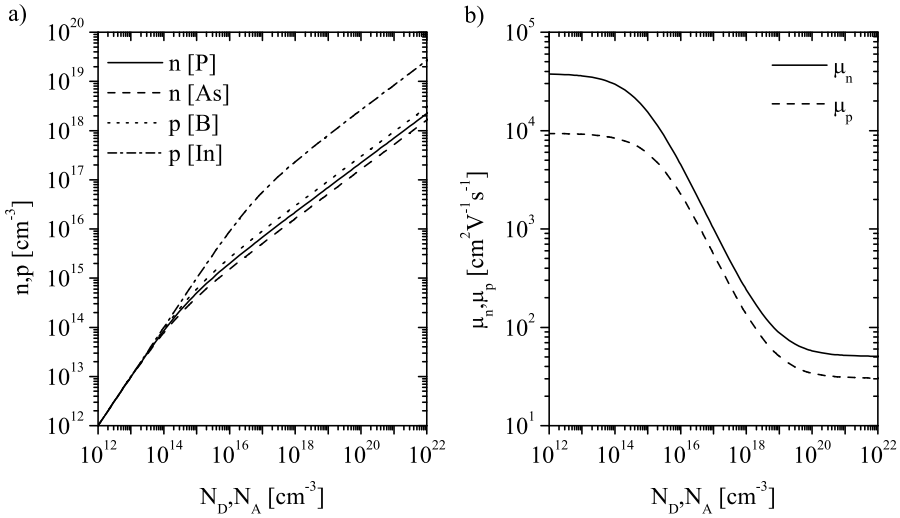

Figure 3.2: a) Model values of the carrier density vs. impurity density at 77K based on equations (3.5) and (3.6) for n-type, Phosphorous and Arsenic, and p-type, Boron and Indium doping. b) Model values of the carrier mobility vs. impurity density at 77 K for n-type and p-type materials based on equation (3.9).

the several doping materials is determined by the ionization energies and by the effective hole and electron masses.

The mobility of the carriers is determined by the mean free path length of the carriers which is limited by scattering. Distinction can be made between impurity and lattice scattering. Theoretical analysis shows that the mobility due to lattice scattering $\mu_{\mathrm{L}} \sim T^{-3/2}$ while the mobility due to impurity scattering $\mu_{\mathrm{I}} \sim T^{3/2}$ [89]. Mnatsakanov et al. [90] derived an universal analytical approximation for the carrier mobility for the most common semiconductor materials as a function of temperature and impurity density which is:

$$\mu(N,T) = \mu_{\max}(T_0)\frac{B(N)\left(\frac{T}{T_0}\right)^{\beta}}{1+B(N)\left(\frac{T}{T_0}\right)^{\alpha+\beta}} \tag{3.9}$$

where $B(N)$ is:

$$B(N) = \left[\frac{\mu_{\min}+\mu_{\max}\left(\frac{N_g}{N}\right)^{\gamma}}{\mu_{\max}-\mu_{\min}}\right]\Bigg|_{T_0} \tag{3.10}$$

with $T_0 = 300$ K. Here, N is the impurity density so N_{A} or N_{D} depending on the doping type. In the table below the rest of the parameters are given for silicon. The parameter $\mu_{\max}$ characterizes mobility in lightly doped samples, where the

Table 3.1: Material dependent parameters for equations (3.9) and (3.10), adapted from [90].

Carrier type	$\mu_{\max}$ [$\mathrm{cm^2V^{-1}s^{-1}}$]	$\mu_{\min}$ [$\mathrm{cm^2V^{-1}s^{-1}}$]	N_{g} [$\mathrm{cm^{-3}}$]	α	β	γ
Electrons	1414	68.5	9.2×10^{16}	2.42	0.26	0.71
Holes	470.5	44.9	2.2×10^{17}	2.20	0.36	0.72

principal scattering mechanism is scattering on lattice vibrations, whereas $\mu_{\min}$ characterizes mobility under heavy doping conditions, when impurity scattering dominates. γ is determined by the semiconductor material and α and β are associated with the temperature dependencies of the lattice and impurity scattering respectively. The parameters for n-type and p-type doped Si are given in table 3.1.

In figure 3.2b) the model values for the mobility are displayed. Unlike the carrier density the mobility differs only between the doping type, n or p, but not between all individual materials. Furthermore it is obvious that for a certain doping density the n-type material shows a higher mobility. So electrons are more mobile than holes which intuitively can be understood.

3.3 Practical Hall Devices

The Hall voltage is linearly dependent on the bias current as follows from equation (3.1). However the bias current is limited by the maximum power that can be dissipated in the device or even more in general the power density. Because the thickness is much smaller than the length and width it suffices to define a dissipated power density per unit of area. The power is given by $P = I_{\mathrm{b}}^2 R$ and the power density per unit of area is given by $P_{\mathrm{d}} = P/lb$. When these two expressions and equation (3.3) are substituted in equation (3.1), an expression can be derived which gives the Hall voltage as a function of the power density in the device:

$$V_{\mathrm{H}} = R_{\mathrm{H}} B_y b \sqrt{\frac{P_{\mathrm{d}}}{\rho d}}. \tag{3.11}$$

3.3.1 Device Geometry

The thickness d and width b of the device are the only geometry variables in equation (3.11). The Hall device used in this model is assumed to be infinitely long with infinitely narrow voltage sensing contacts. When devices with finite length and voltage sensing contact widths are considered the voltage potential lines are influenced having a negative effect on the sensitivity. These effects can

be taken into account by introducing a geometry factor G for which holds [91]:

$$G = \frac{U_{\mathrm{H_G}}}{U_{\mathrm{H}}}. \tag{3.12}$$

Here $U_{\mathrm{H_G}}$ is the Hall voltage with the correction for the geometry. G is unity for infinitely long Hall elements with infinitely narrow voltage contacts and smaller than unity for finite dimensions. For a rectangular Hall device geometry with $l/b > 1.5$, $s_{\mathrm{v}}/b < 0.18$ where s_{v} is the voltage contact width and the sensing contacts are in the middle of the device the geometry factor can be approximated by [92]:

$$G = \left[1 - \exp\left(-\frac{\pi l \theta_{\mathrm{H}}}{2b\tan(\theta_{\mathrm{H}})}\right)\right]\left[1 - \frac{2s_{\mathrm{v}}\theta_{\mathrm{H}}}{\pi b\tan(\theta_{\mathrm{H}})}\right], \tag{3.13}$$

where θ_{H} is the Hall angle which describes the rotation of the equipotential lines in the Hall device. For θ_{H} holds that $\tan(\theta_{\mathrm{H}}) = R_{\mathrm{H}} B_y \rho^{-1}$. When the applied magnetic field is small $\theta_{\mathrm{H}} \to 0$ and $\theta_{\mathrm{H}}/\tan(\theta_{\mathrm{H}}) = 1$.

For very small Hall angles, short samples ($l < b$) and narrow sensing contacts $s_{\mathrm{v}} \ll l$, G can be approximated by [93]:

$$G = 0.74\frac{l}{b}. \tag{3.14}$$

3.3.2 Hall Devices in an Inhomogeneous Magnetic Field

The Hall voltage expression of equation (3.1) assumes a homogeneous field over the sensor. In this particular case where the magnetic field is coming from a current carrying wire the field on the sensor is not homogeneous. The effective field on the sensor $B_{y,\mathrm{eff}}$ is given by the integral of the field over the width of the sensors:

$$B_{y,\mathrm{eff}} = \frac{1}{b}\int_{b_0}^{b_0+b} B_y(z)dz, \tag{3.15}$$

where b_0 and $b_0 + b$ represent the outer dimensions with respect to the width of the device. This form is based on the same coordinate system as figure 3.1. Suppose

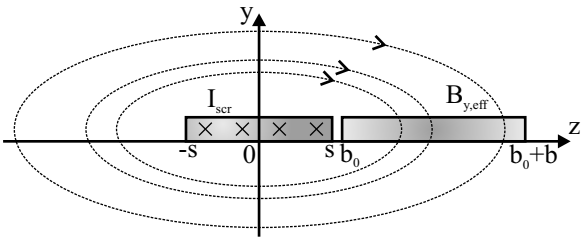

Figure 3.3: Schematic representation of the magnetic field of a current carrying strip with width $2s$ on a Hall device of width b

we assume a strip with width $2s$ from $-s$ to s as displayed in figure 3.3 carrying a I_{scr} homogeneously distributed over the cross section of the strip. The field next to the strip $B_y(z)$ is [46]:

$$B_y(z) = \frac{\mu_0 I_{\mathrm{scr}}}{4\pi s} \ln\left(\frac{z+s}{z-s}\right) \quad \text{for } z < -s \wedge z > s. \tag{3.16}$$

Substitution of equation (3.16) in (3.15) yields after integration:

$$\begin{aligned} B_{y,\mathrm{eff}} = \frac{\mu_0 I_{\mathrm{scr}}}{4\pi b s}\Big\{&(-b_0 - s)\ln(b_0 + s) + (b_0 + b + s)\ln(b_0 + b + s) \\ &+(b_0 - s)\ln(b_0 - s) + (-b_0 - b + s)\ln(b_0 + b - s)\Big\}. \end{aligned} \tag{3.17}$$

3.4 Superconducting Flux Concentrators

A superconducting ring is used as a flux concentrator. The flux that is screened out of the hole of the concentrator is $\Phi = B_{\mathrm{a}} A_{\mathrm{eff}}$ where A_{eff} is the effective area. The screening current generated by the flux is $I_{\mathrm{scr}} = \Phi / L_{\mathrm{tot}}$ where $\mathrm{L_{tot}}$ is the total inductance of the ring. By substituting the first expression in the second an expression for the screening current as a function of the inductance, applied field and effective area is obtained:

$$I_{\mathrm{scr}} = \frac{B_{\mathrm{a}} A_{\mathrm{eff}}}{L_{\mathrm{tot}}}. \tag{3.18}$$

This form can be substituted in equation (3.17) and one can see that $B_{y,\mathrm{eff}} \propto A_{\mathrm{eff}}/L_{\mathrm{tot}}$. Now a relation between the effective field and the background field is obtained. However this is only the field generated by the current in the constriction and so the total field on the sensor is $B_{y,\mathrm{eff}}$ from equation (3.17) plus the background field B_{a}. This combined and substituted in equation (3.11) gives:

$$V_{\mathrm{H}} = R_{\mathrm{H}} b \sqrt{\frac{P_{\mathrm{d}}}{\rho d}} \left(B_{\mathrm{a}} + B_{y,\mathrm{eff}}\right). \tag{3.19}$$

3.4.1 Effective Area and Inductance

From the relation in equation (3.19) follows that optimum performance can be obtained when the quotient $A_{\mathrm{eff}}/L_{\mathrm{tot}}$ is maximized. In literature the inductance and effective area of a square washer with outer diameter D and and inner diameter d have been derived. The inductance consists of two main contributions, the hole inductance L_{h} and the slit inductance L_{s}. The hole inductance is solely determined by the diameter of the hole with respect to the the outer diameter and is given by the following set of equations:

$$L_{\mathrm{h}} = \frac{2}{\pi}\mu_0 \left(d + \frac{D-d}{2}\right)\left[\ln\left(1 + \frac{2d}{D-d}\right) + \frac{1}{2}\right] \quad \text{for } \frac{2d}{D-d} > 10 \quad [94] \quad (3.20)$$

$$L_{\mathrm{h}} = \frac{2}{\pi}\mu_0 d\left[\ln\left(5 + \frac{2d}{D-d}\right) + \frac{1}{4}\right] \quad \text{for } 1 < \frac{2d}{D-d} < 10 \quad [95] \quad (3.21)$$

$$L_{\mathrm{h}} = 1.25\mu_0 d \quad \text{for } 1 > \frac{2d}{D-d} \quad [96] \quad (3.22)$$

The slit inductance is determined by the length of the slit and is typically $L_{\mathrm{s}} = 0.4$ pH/μm. The total inductance of the concentrator is given by the sum of these two contributions so $L_{\mathrm{tot}} = L_{\mathrm{s}} + L_{\mathrm{h}}$.

For square washers the effective area is given by:

$$A_{\mathrm{eff}} = cdD, \quad (3.23)$$

where c is a constant close to unity [97, 98]. Both the total inductance and the effective area are used in the optimization of the concentrator design as discussed further on in section 3.5.2.

3.5 Overall Device Parameters and Design

3.5.1 The Sensor

In the search for optimal Hall devices one is looking for a material with a low carrier density because this gives a high Hall coefficient. On the other hand it is desirable to restrict the device resistance. High device resistances cause high offset voltages due to misalignment of the voltage contacts or anisotropy. Moreover, even relatively small bias currents will result in high voltage drops between the current contacts which requires specialized current sources. The relation between Hall coefficient and device resistance can be derived from equations (3.2) and (3.4) and is $\rho = R_{\mathrm{H}}/\mu$ when one assumes a Hall element with only one type of charge carriers. This shows that high Hall coefficients result in high device resistances and that this resistance can only be limited by the mobility which should be maximized however this is determined by the doping density. Further analysis of equation (3.11) shows that for maximization of the Hall voltage $R_{\mathrm{H}}/\sqrt{\rho}$ or in terms of carrier density and mobility: μ/n should be maximized. In figure 3.4 μ/n vs. the doping density and the normal resistance is shown for several dopant species. Figure 3.4a) shows that irregardless of the dopant species decreasing the density results in an increase in μ/n. This variation in dopant density and therefore a variation in carrier density and mobility also results in a change of the resistance which is displayed in figure 3.4b). An interesting region is visible between $10^{-1} < \rho < 10^{1}$ Ωcm where a variation of the dopant density results in a variation of μ/n but not so much in a change of ρ. Outside this region in general the n-type dopants result in the highest μ/n given a specific resistance value.

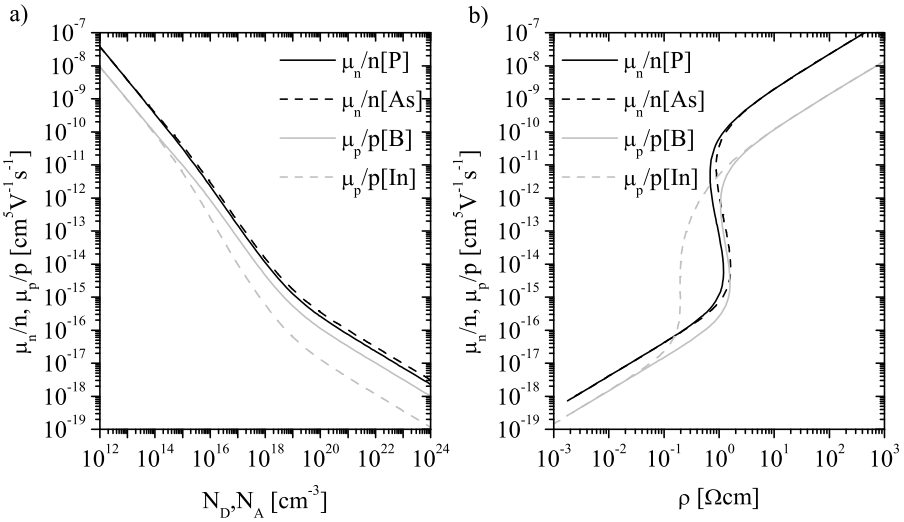

Figure 3.4: μ/n versus the dopant density in a) and the normal resistance in b). The n-type dopants are displayed in black and the p-type dopants in gray.

Besides the choices that have to be made based on the material properties there are also geometrical variables. The geometrical correction factor of equation (3.13) shows that the correction factor approaches unity when the Hall sensor is long with respect to the width and if the voltage contact width is minimized. Equation (3.19) shows that the sensitivity is improved when the width of the device is increased. Increasing the width and the length of the device however also means that the total power dissipated also increases due to the assumed power density limit and therefore a trade-off has to be made.

The width of the sensor is chosen to be $b = 250$ μm and the length $l = 400$ μm. For this device SIMOX SOI wafers are used [99]. SOI stands for silicon on insulator and these wafers consist of a film of single crystalline Si separated by a layer of SiO_2 from the bulk substrate. There are numerous ways to produce such wafers and one technique is by separation by implantation of oxygen (SIMOX). The main advantage of SIMOX SOI wafers is that it is available with very thin top layers. For these devices the top layer was $d = 50$ nm which directly can be translated as the thickness of the Hall device discussed in this section. The reason that SOI substrates are used is twofold. The Hall device is defined by ion implantation which results in very well defined doping profile when applied to SOI wafers. Moreover the concentrator is made of YBCO deposited by pulsed laser deposition which shows much better growth characteristics due to a relaxation of the thermal stress in the SiO_2 interlayer. Doping implantation in and YBCO deposition on SOI wafers will be discussed in more detail in chapter 4. Substitution of these values in equation (3.13) yields $G \approx 0.9$. The width of the sensing contacts is 10 μm. In principle it is possible to make this smaller with standard lithography processes

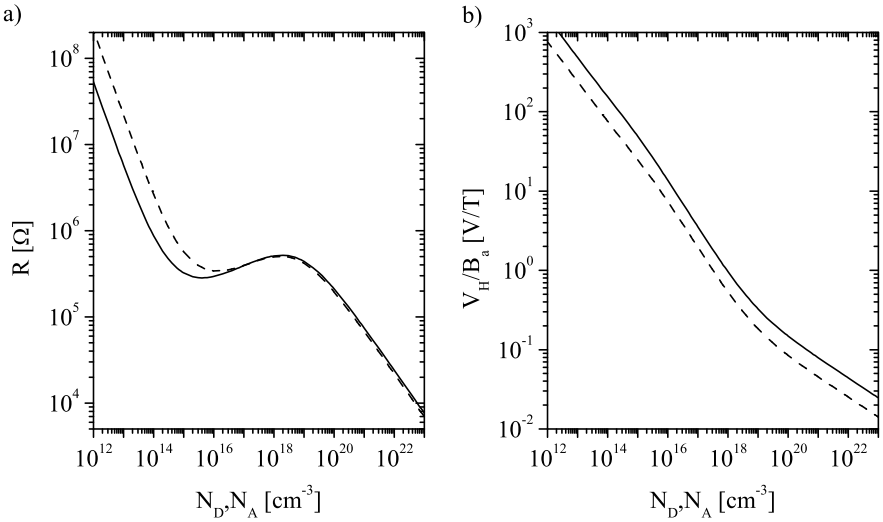

Figure 3.5: Resistance a) and field sensitivity b) versus the dopant density for a device with $d = 50$ nm, $l = 400$ μm and $b = 250$ μm at $T = 77$ K. The solid lines show the results for arsenic doping and the dashed line for boron doping

however narrower contacts will also drastically increase the resistance between the sensing contacts.

In figure 3.5 the device resistance and the field sensitivity are displayed vs. the doping density of arsenic (solid line) and of boron (dashed line) at $T = 77$ K. The power density limit for this plot is $P_\mathrm{d} = 100$ kW/m^2 which means that the power dissipated in the device is $P = 10$ mW. From a sensitivity as well as a device resistance point of view arsenic (As) doping is preferred because of the higher sensitivity and lower resistance for the lower part of the doping range. In the doping interval of $10^{15} - 10^{17}$ cm^{-3} a minimum in the device resistance takes place. The optimum arsenic doping is $N_\mathrm{D} \approx 4{\times}10^{15}$ cm^{-3} which gives $R = 283$ kΩ and a sensitivity $V_\mathrm{H}/B_\mathrm{a} = 23$ VT^{-1} [100]. Given the power density limit the bias current is $I_\mathrm{b} = 0.18$ mA and the voltage over the device $V = 53$ V which are acceptable values for multi purpose current sources. This would be an improvement of a factor of 575 compared to the sensitivity of 40 mVT^{-1} obtained in the work of Schmidt et al. [46].

3.5.2 The Concentrator

In section 3.4.1, expression (3.23) shows that the outer diameter of the concentrator should be as large as possible. For practical reasons the device is fabricated on a 10×10 mm^2 substrate. As mentioned, the concentrator is deposited with pulsed

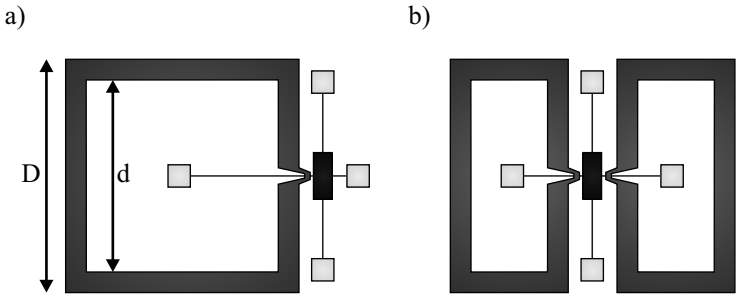

Figure 3.6: Schematic representation of a hybrid magnetometer based on a single (a) and a double (b) concentrator. The concentrator is visible in dark gray, the Hall sensor in black and the voltage and bias current connections in light gray.

laser deposition. This choice for the substrate size was made since the sensor has to be mounted on a heater and the deposition is only homogeneous in a small area, which is determined by the shape of the plasma plume. Due to bad reproducibility of structures close to the edge of the substrate, in general structures made on 10×10 mm^2 substrates do not exceed 8×8 mm^2. Because the concentrator is much larger than the sensor, the space needed for the sensor is neglected in this section. Equation (3.17) shows that the best coupling between concentrator and sensor is obtained when the width of the constriction is minimized. Intuitively this can be understood because the current through the constriction is brought closer to the sensor. The minimum width of the constriction is determined by the critical current density of the superconductor J_c and the desired maximum magnetic field of the device B_{max}. A higher applied magnetic field results in a higher screening current which is limited by the critical current density. The minimum width of the constriction is given by:

$$2s = \frac{B_{max} A_{eff}}{J_c d L_{tot}}. \tag{3.24}$$

When the concentrator effective area A_{eff} is maximized this means that s also increases which results in a decreased coupling. Instead of using a single concentrator it is however possible to use a double concentrator layout as schematically shown in figure 3.6.

Figure 3.6a) shows a single square flux concentrator. For this design the analytical expressions from section 3.4.1 can be used to obtain the best A_{eff}/L_{tot} ratio by varying the inner diameter d. However an approach with two concentrators as displayed in figure 3.6b) demands rectangular structures. To my best knowledge there has been statistical modeling of inductances [101] but are no analytical expressions for the effective area and total inductance available for rectangular washers.

Finite element simulations on the effective area A_{eff} and the total inductance L_{tot} for square and rectangular washers were performed in Comsol [102] and Sonnet [103]. The effective area of the washer is determined with Comsol. In the model

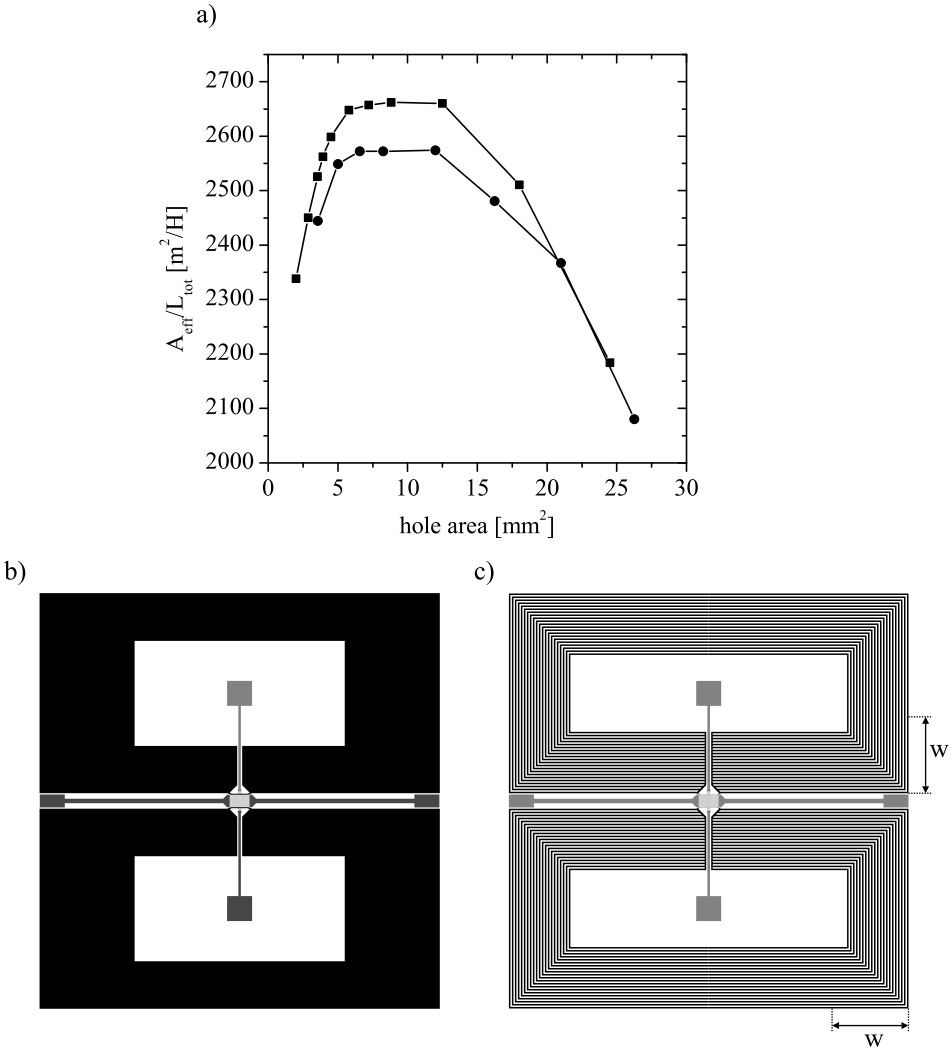

Figure 3.7: a) $A_{\text{eff}}/L_{\text{tot}}$ vs. the hole area for the design shown in figure b) (squares) and in figure c) (dots). b) Resulting optimum design with a hole area of 8.82 mm^2 c) Optimum design for a concentrator with identical width w with a 8.25 mm^2 hole.

a magnetostatic environment is assumed where there are no currents flowing in the material. In ideal superconductors the relative magnetic permeability $\mu_r = 0$, in the model $\mu_r \rightarrow 0$ is assumed. In the simulation a magnetic field is applied perpendicular to the washer. The problem is visualized by magnetic field lines. Outside the effective area the magnetic field is guided to the outside of the washer and within the effective area it is guided through the hole. Note that the model is not taking into account any screening effects and therefore the field lines pass through the hole of the washer. The inductance is determined with Sonnet. This program is a high frequency electromagnetic solver where a superconductor is interpreted by including a kinetic induction term which is taken from [104].

To test the quality of the simulations these are first performed for square washers. Comparison between the finite element simulations of the effective area with Comsol and model values of equation (3.23) shows that the difference in values does not exceed 10 %. Also the simulations of the inductance in Sonnet showed a reasonable fit with the model values of equations (3.20)–(3.22). The optimum hole size was found to be between $D/3 \leq d \leq D/2$. Because this approach can at least give a qualitative estimation of the optimum ratio between hole size and outer dimension this is also applied on the rectangular washers.

The results for $A_{\text{eff}}/L_{\text{tot}}$ vs. the hole area of a rectangular washer are displayed in figure 3.7a). In the simulations the outer dimensions of the concentrator are $4{\times}8$ mm^2. The squares represent a hole with the same aspect ratio as the outer dimensions comparable to the schematic representation in figure 3.7b). The circles represent a situation where the distance between the outside and inside is kept the same, denoted with w in figure 3.7c). In this situation the concentrator is slotted. The resulting narrow strips have certain critical magnetic field below which no flux vortices are trapped. This is important when these devices are operated in an unshielded environment and the thermal movement of trapped flux vortices result in deterioration of the 1/f noise properties. The conditions for vortex trapping are discussed in more detail in chapter 2. The best $A_{\text{eff}}/L_{\text{tot}}$ ratio is obtained for the situation of figure 3.7b) with a hole area of 8.82 mm^2. Figure 3.7c) shows the optimum hole size with identical width and an area of 8.25 mm^2.

3.5.3 Overall Device

The maximum magnetic field $B_{\max}$ of the device is determined by the width of the constriction as was already shown in equation (3.24). From equation (3.19) one can derive that the highest Hall voltage can be obtained by minimizing s and maximizing b. In figure 3.8a) the field sensitivity V_H/B_a versus the width of the sensor b is displayed for several dynamic ranges varying between $1\ \mu\text{T} < B_{\max} < 100\ \mu\text{T}$. The black lines represent the model values for the double concentrator layout which are always larger than the values of the single concentrator layout shown in gray. In this analysis the geometrical correction factor of equation (3.13) is not included since this would also require a variation of the length of the device.

For the concentrator a critical current density $J_c = 2 \times 10^6$ Acm^{-2} is assumed and a thickness of 400 nm which is the best critical current density and maximum

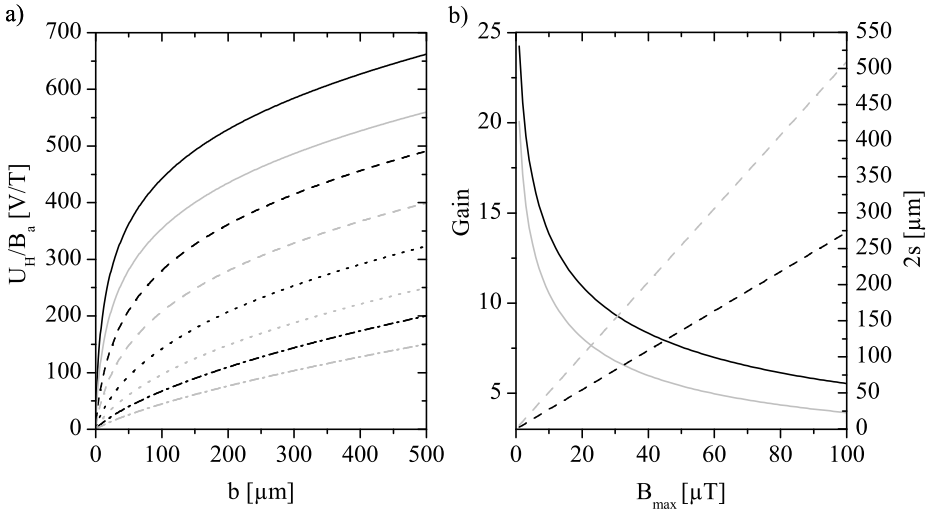

Figure 3.8: a) Field sensitivity vs. sensor width for $B_{\max} = 1$ μT (solid), $B_{\max} = 5$ μT (dashed), $B_{\max} = 25$ μT (dotted) and $B_{\max} = 100$ μT (dash-dotted). The black lines represent the double concentrator and the gray lines the single concentrator design. b) Field gain (solid) and s (dashed) vs. the dynamic range. Again the black lines represent the double concentrator and the gray lines the single concentrator approach.

thickness for YBCO films deposited on SOI reported on [105]. The single concentrator layout has an outer diameter of $D = 8$ mm with a hole of $d = 3$ mm. The model values for the double concentrator layout are based on the design of figure 3.7b). The difference in model values between this design and the design of figure 3.7c) is marginal especially compared to the results for the single concentrator and therefore not shown in the graph. Except for the width of the sensor the dimensions and material properties of the Hall element are the same as in section 3.5.1. For every dynamic range the double concentrator layout shows the best sensitivity. Moreover this graph illustrates that the width of the sensor should be maximized. However as already mentioned this also means that the length should be increased which increases the power dissipated in the sensor. For the graph in figure 3.8b) an intermediate width of the sensor is chosen of $b = 250$ μm as in section 3.5.1. The gain of the double concentrator is for the whole dynamic range about a factor of $\sim$1.5 more sensitive than the single concentrator approach. On the right axis of the graph the width of the constriction $2s$ is shown versus the dynamic range. Because $A_{\text{eff}}/L_{\text{tot}}$ is smaller for the double concentrator layout the increase is less compared to the single concentrator design for an increasing dynamic range.

For the overall sensitivity of this design the field gain of corresponding dynamic range has to be multiplied with the sensitivity of the Hall sensor of 23 VT^{-1} as derived in section 3.5.1.

3.6 Summary

In this chapter a theoretical model for hybrid magnetometers has been presented and discussed. The carrier density and mobility as a function of the doping density and temperature in doped Si and its effect on the Hall sensor sensitivity and resistance are presented. Considerations are made for practical Hall devices. This includes considerations on the shape and the doping density. A lower doping density yields a lower carrier density which is beneficial for the the sensor sensitivity. However it also means that the sensor resistance increases and a consideration on the maximum allowable device resistance value and dissipated power should be made. In theory the Hall sensor can reach a sensitivity of 23 VT^{-1} while the resistance of the device is 283 kΩ.

It should be noted that due to the relatively low doping density it is likely that the semiconductor metal interfaces in the electrodes suffer from the Schottky effect. This can partly be overcome by choosing an appropriate electrode material with a relatively low work function like for example Ti. A second possibility would be injecting a higher dopant dose in the Hall element at the connections which also limits the resulting barrier height.

The coupling between the sensor and the concentrator is investigated and considerations are made between the device maximum field of operation and the gain which can be obtained by the concentrator. Depending on the required maximum magnetic field the gain can be between 5 and 30. The difference in gain between a single and a double concentrator layout using the same area has been investigated. The double concentrator yields a factor $\sim$1.5 in gain for the same device size.

CHAPTER

4

Experimental Aspects of Fabrication

Abstract

The fabrication process of hybrid magnetometers in general comprehends well developed techniques. Some of the less trivial production steps are highlighted. RF sputtering of Bi is investigated for the Bi hybrid magnetometer . The resulting films were rather rough. Measurements showed Hall coefficient and specific resistance values that reasonably correspond with those from reports in literature with other deposition techniques. Doping implantation in Si and YBCO growth on Si were investigated for application in the doped Si hybrid magnetometer. By means of simulations the optimum dose and acceleration voltage for implantation were determined. Samples were doped with As and B and were characterized by means of Hall and van der Pauw measurements. YBCO films on SOI wafers were grown with pulsed laser deposition. Yttrium stabilized Zirconia (YSZ) and CeO_2 were used as buffer layers to provide the correct growth orientation and lattice match and to prevent diffusion of oxygen.

4.1 Introduction

For the fabrication of hybrid magnetometers several thin film techniques were used. Most of the techniques are well known and do not need any further clarification. For an extensive overview one can refer to [106]. This chapter deals with the more challenging production steps which are not so straightforward. Two magnetometer designs have been developed. The fabrication process of the first design which consists of a $YBa_2Cu_3O_{7-\delta}$ (YBCO) flux concentrator and a bismuth (Bi) Hall element is more or less comparable with the process followed in the work of Schmidt et al. [46]. The second design is based on a doped silicon (Si) Hall device and also has a YBCO flux concentrator. First an overview of the magnetometers will be given with respect to the fabrication process and stacking of the subsequent films. After that some critical fabrication steps are highlighted. This will start with RF sputtering of Bi which is obviously the Hall sensor material of the first design. This is followed by two section on the fabrication of the doped Si based device. First doping implantation in Si is discussed and after that YBCO pulsed laser deposition on Si.

4.1.1 Hybrid Magnetometer with a Bi Hall Device

The Bi Hall device hybrid magnetometer is fabricated on a $SrTiO_3$ (STO) substrate. The YBCO concentrator is deposited by pulsed laser deposition. Pulsed laser deposition of YBCO on STO is a well known process which results in high quality films with a critical temperature of ∼92 K. On top of the YBCO a gold (Au) layer is sputtered. This film prevents diffusion of oxygen from the YBCO layer to either the SiO_2 or Bi layer deposited later in the process. The YBCO/Au is structured by argon (Ar) ion milling. On top of that a SiO_2 layer is deposited by RF-sputtering and structured by a lift-off photolithography process. The SiO_2 creates an isolating bridge over the constriction of the concentrator so the voltage lead of the Bi Hall device can make a connection with the voltage readout contact. The Bi film is deposited and structured by the same technique.

Figure 4.1 shows the layout and cross section of the most important part of the device, around the sensor. Figure 4.1a) shows the stacking of the subsequent layers along the dotted line of the scanning electron microscope (SEM) image of figure 4.1b). On top of the substrate the two voltage contacts indicated on the left and right with V^+ and V^- and the constriction between those two is visible in dark gray. The actual Hall device is in between the constriction and the voltage contact V^-. The rest of the Bi is the voltage contact wire to the V^+ connection.

Bi can be deposited by several techniques and is known to be a difficult material in thin films since it is hard to grow smooth films. In section 4.2 the investigation to the optimal deposition conditions of Bi is discussed.

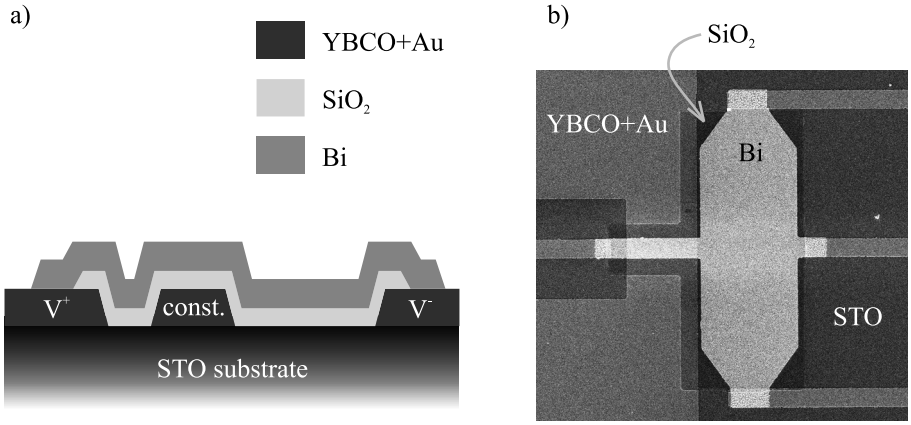

Figure 4.1: a) Cross section of the stacked layers for the Bi Hall device based hybrid magnetometer showing the sensor and the constriction indicated by the dotted line in b). On top of the substrate the two voltage contacts indicated on the left and right with V^+ and V^- and the constriction between those two is visible in dark gray. b) SEM image of the sensor part of a Bi Hall device based hybrid magnetometer.

4.1.2 Hybrid Magnetometer with a doped Si Hall Device

The doped Si Hall device hybrid magnetometer is fabricated on a silicon on insulator (SOI) substrate. These devices all have a double concentrator layout as discussed in chapter 3. A cross section of the stacked layers is shown in figure 4.2.

The first production step concerns the implantation of dopants in the top Si layer of the SOI wafer. Implantation in Si and in particular in SOI wafers is highlighted in section 4.3. The second step is the pulsed laser deposition of the YBCO flux concentrator. In the deposition process one or two buffer layers of Yttrium stabilized Zirconia (YSZ) or YSZ/CeO_2 are added. The concentrator is structured by a photolithography process and H_3PO_4 wet etching. The contacts between the Hall element and the electrodes are made by Ar ion etching through the YSZ and CeO_2 layer. Due to a large difference in thermal expansion coefficients and lattice parameters, pulsed laser deposition of YBCO on Si is not straightforward. This process step is further discussed in section 4.4. The actual Hall element is in between the two constrictions as displayed in figure 4.2. The rest of the implanted area is, comparable to figure 4.1, for the voltage readout connections. These connections are made of titanium (Ti) covered with a Au electrode. Both layers can be deposited by in situ RF-sputtering and are structured by a lift-off photolithography process. In figure 4.2 the voltage connections are displayed on top of the doped region.

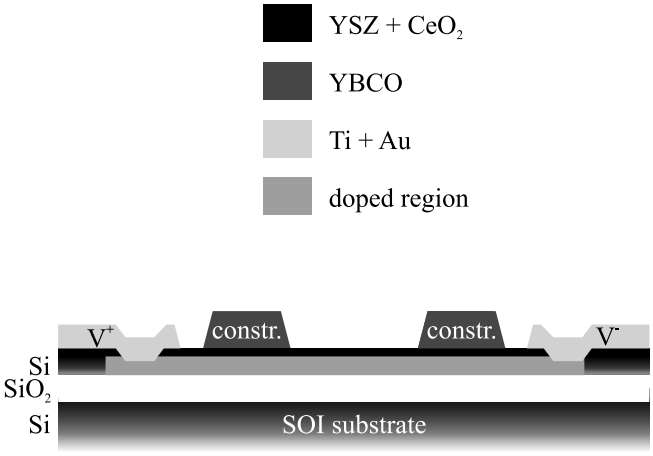

Figure 4.2: Cross section of the stacked layers for the doped Si Hall device hybrid magnetometer showing the part around the sensor comparable to the situation in figure 4.1 but now with two concentrators.

4.2 Bismuth Deposition

Bi is the metal element with the lowest carrier density in the periodic system. Combined with the property that it has a relatively high carrier mobility, since it is a metal, it is suitable as a Hall sensor material. Since the 1960s investigations concerning Bi film growth were motivated by both ordinary and quantum size effect studies. In literature reports have been made on the deposition of Bi by various techniques like PLD [107–109], DC-sputtering [109], RF-magnetron sputtering [110], thermal evaporation [46], electro deposition [111] and molecular beam epitaxy (MBE) [112, 113].

In general the cited articles all show rough films with grains or droplet like particles varying in size from ∼50 nm up to particles of several tens of micrometers, dependent on the deposition conditions. Rough films are for the aimed application in this thesis not by definition a problem as long as a closed current path can be realized. Not all cited papers mention the electrical transport properties, however comparison of these properties for the different deposition techniques are essential to draw conclusions on the best deposition technique for this material. The best morphological and, when available, electrical properties were obtained when the substrate was slightly warmed up to ∼400 K during deposition.

In the work of Schmidt et al. [46], Bi was used as a Hall sensor material in a hybrid magnetometer and was deposited by thermal evaporation. The Bi film is grown on top of a sputtered CeO_2 insulating layer and a Hall coefficient of $R_H = 1.3\ \mathrm{cm^3C^{-1}}$ and a specific resistance of $\rho = 1250\ \mu\Omega\mathrm{cm}$ were obtained at $T = 77$ K. Kim et al. [110] deposited Bi by RF-magnetron sputtering on glass substrates. At a deposition temperature of $T_{dep} = 400$ K the best films were obtained with

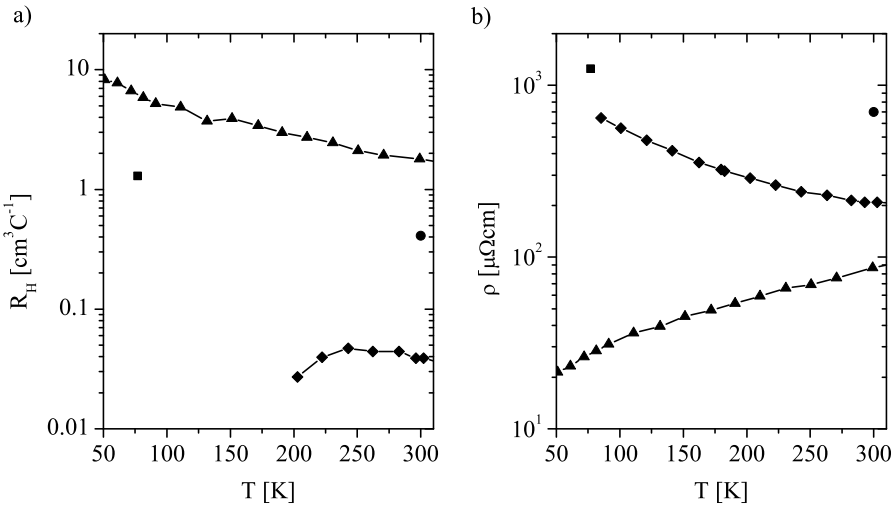

Figure 4.3: Hall coefficient and specific resistance vs. temperature obtained from literature. Data from Schmidt et al. [46] (blocks) by thermal evaporation, Kim et al. [110] (dots) by RF magnetron sputtering, Partin et al. [113] (triangles) by MBE and Boffoue et al. [108] (diamonds) by pulsed laser deposition.

$R_{\mathrm{H}} = 0.41$ cm^{3}C^{-1} and $\rho = 700$ $\mu\Omega$cm measured at room temperature. Partin et al. [113] investigated the electrical properties as a function of the temperature of Bi deposited by molecular beam epitaxy (MBE) on barium fluoride single crystals. Another extensive survey of the specific resistance and Hall coefficient as a function of temperature is published by Boffoue et al. [108] who deposited Bi films by pulsed laser deposition on glass substrates at room temperature.

The Hall coefficients and specific resistances measured as a function of temperature of Partin et al. and Boffoue et al. are shown in figure 4.3 together with the data points from Schmidt et al. and Kim et al. The Hall coefficient data presented in the paper of Boffoue et al. shows very small Hall coefficients which moreover exbihit a change of sign as a function of temperature. In figure 4.3a) only the positive part the date set is shown. The sign change is attributed to the orientation of the crystallites which are perpendicular and along the trigonal axis and a mixing of two components of the Hall coefficient can occur. From a Hall coefficient and specific resistance point of view MBE is the best deposition technique for Bi since it results in the highest Hall coefficients and the lowest specific resistances. One should however note that the films deposited by MBE on barium fluoride single crystals are epitaxial films and the measured values approach those of bulk Bi. In the research presented in this thesis the films are deposited on SiO_2 which means that the characteristic values obtained by MBE deposition are out of reach since no epitaxial films can be obtained. Although there is a difference in the specific resistance and Hall coefficient for thermal evaporation and RF-magnetron sputtering

one should note that these parameters are not given at the same temperature and are therefore not directly comparable. The PLD samples show a smaller specific resistance than the other techniques but on the other hand the Hall coefficient is very small and changing sign as a function of temperature. Due to availability and the fact that the difference between sputtering and evaporation is not very large RF-sputtering of Bi films is further investigated.

4.2.1 Deposition Setup and Substrate Material

The optimum deposition conditions for RF-sputtering of Bi were investigated by a visual inspection as well as electrical characterization. A Bi target with a purity of 99.999% was used. As mentioned, reports in literature show that the best film quality was obtained when the substrate was slightly heated and therefore a heater was mounted in the system. The sputtering process is carried out in an Ar environment. In the deposition study the substrate temperature, sputtering power and Ar pressure are varied.

The deposition was carried out for 5 temperature values between 373 and 413 K. The choice for this temperature range is based on the results from literature [107, 110, 112, 113]. Two values, 100 and 200 W, for the sputtering power were used. Higher power values were not possible due to limitations in the power management of the system. For lower powers it was not possible to create a plasma. Three argon process pressures, 5×10^{-3}, 2.5×10^{-2} and 5×10^{-2} mbar, were used. In principle films were deposited for every combination of the temperature, sputtering power and process pressure except for a power of 100 W with a pressure of 5×10^{-3} mbar since it was not possible to create a plasma for this condition.

As shown in figure 4.1 the largest part of the Bi sensor is deposited on top of an SiO_2 layer. Therefore the growth experiments were carried out on thermally oxidized Si substrates. These substrates contain a SiO_2 film of several hundreds of nanometers. For comparison, native oxide has a typical thickness of only $\sim$2 nm. In principle there is no direct reason to expect any effect of the thickness of the SiO_2 layer but since in the actual device the SiO_2 layer will have a more comparable thickness to the thermally oxidized substrates this choice was made.

4.2.2 Visual Investigation

The deposited Bi samples were analyzed by means of SEM imaging. In figure 4.4a) and 4.4b) two typical SEM images are displayed. These particular images are both for samples deposited in a 5×10^{-2} mbar Ar environment with a sputtering power of 100 W and at a temperature of 373 K and 388 K, respectively. To get a better depth perspective the sample is tilted to a 45° angle.

In these images a transition in morphology is visible. The film shown in figure 4.4a) contains small particles with a diameter of $\sim$100 nm together with larger particles of $\sim$1 μm with a density of $\approx 7.5 \times 10^4$ mm^{-2}. In the image shown in figure 4.4b) the size distribution of the particles is more narrow with a typical diameter of $\sim$ 400 nm. Although the difference in deposition temperature is only

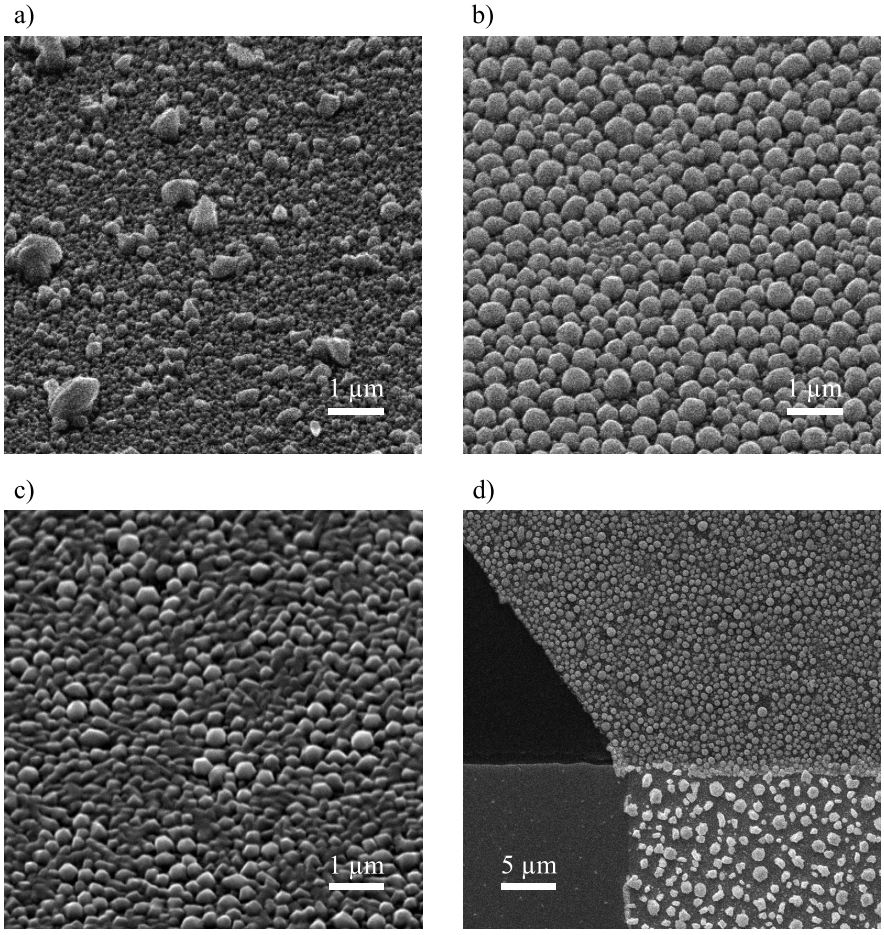

Figure 4.4: SEM images for deposited Bi layers at an Ar pressure of 2.5×10^{-2} mbar and a sputtering power of 100 W at a temperature of a) 373 K and b) 388 K. c) SEM image of a special randomly occurring growth for $T \geq 388$ K. d) SEM image of a part of the Bi Hall sensor showing one of the current leads of YBCO/Au in the bottom of the figure connected to the Hall sensor on the right extending to the top of the image.

15 K there is a large change in morphology. For deposition temperatures below 373 K the growth stayed comparable to the one shown in figure 4.4a) and for deposition temperatures above 388 K the growth stayed comparable to the one shown in figure 4.4b). Both images show strong indication for island or Volmer Weber growth. In this growth mode there is insufficient bonding between the particles and the substrate which is also confirmed by the fact that the films easily come off the substrate. An increase in substrate temperature increases the surface diffusion of the particles and allows coalescence of small particles to larger particles

with a narrower spread in size. Although the images in figure 4.4a) and 4.4b) show the results for the same sputtering power and argon pressure the transition in growth is observed for the whole mentioned power and argon pressure range and occurred at the same temperature. The deposition time used for all deposited films is 10 min. Film thickness analysis by alpha stepper and AFM measurements showed that the various power and pressure settings affected the film thickness which ranges from 220 nm to 490 nm. Changes in the deposition temperature did however not show significant alterations in the film thickness. Figure 4.4c) shows a growth mode that occurred at random power and pressure setting for $T \geq 388$ K and is irreproducible. The typical grain size is comparable to the situation shown in figure 4.4b) however a smoother film where the grains seem to be more connected is occurring. One might expect that when the film thickness is increased the voids between the grains are filled which can result in the situation shown in figure 4.4c). However no relation could be found between the thickness of the film and the occurrence of this growth.

Figure 4.4d) shows a typical SEM image of a part of the Bi Hall device at one of the current connections. In the bottom part of the figure the current lead of YBCO/Au is visible. At the right part of this connection the overlap with the Bi layer starts and the sensor extends to the top of the image where the underlying layer is SiO_2. This image clearly shows that the material on which the the Bi layer is deposited strongly influences coalescence of the particles and the adhesion to the surface. On the current connection the Bi film exhibits a growth comparable to the one shown in figure 4.4a) while on the SiO_2 film the growth is more comparable to figure 4.4b). This means that one can optimize the growth of Bi on one underlying layer but the results on other materials is badly predictable. The Bi film in this device is structured with a lift-off photolithography process which removed the smaller particles on the YBCO/Au surface only leaving the larger particles. Still there existed an electrical connection between the YBCO/Au and the Bi which is most likely accomplished on the edge of the YBCO/Au strip.

To summarize: the visual inspection shows that the deposited films are, irregardless of the deposition conditions, rough exhibiting two distinct types of growth depending on the substrate temperature during deposition. Variations of the film thickness, which is a by-product of variations of the sputtering power and argon pressure, do not show any indication that thicker films will be smoother and moreover one should note that thicker films will decrease the device sensitivity when applied in Hall sensors and is therefore undesirable. From the analysis presented in this section it is not possible to determine which deposition conditions are optimal and electrical investigation is necessary.

4.2.3 Electrical Investigation

The deposited Bi layers have also been electrically investigated by van der Pauw and Hall measurements [114]. These measurements provide the sheet resistance and Hall coefficient of the material from which the carrier density and mobility can be derived.

Several attempts have been made to establish electrical connections to the samples. Bi is a rather soft material which complicates the electrical connection. Samples were mounted in a probe station where electrical connections to the sample are established with conducting needles. Due to the softness of the Bi the layer was easily damaged. Moreover the contact resistances were high and unpredictable due to minor movements of the needles. In a second attempt the standard measurement needles were replaced by a kind that had springs especially meant for applications where the surface should not be damaged by scratches. The results of measurements with these needles were comparable with the measurement with the standard needles which means that the material is extremely soft.

Wire bonding connection showed unmeasurable high contact resistances. Further inspection with an optical microscope showed that although the wire is bonded correctly to the surface, the Bi in the near vicinity of the bond is removed. Electrical connections were established by adding a drop of conducting silver glue to the bond connection. As a variation on this method thin copper wires were simply glued on the surface which showed reasonably good controllable electrical connections to the film. Moreover Bi has the strong tendency to nucleate and is not showing strong adhesion to the substrate which makes the film rather vulnerable.

A few experiments were carried out in a Quantum Design physical properties measurement system (PPMS) [115]. In this system the sample temperature can be varied from room temperature to ~ 2 K and a magnetic field up to 9 T can be applied to the sample. In the PPMS system several measurements have been performed at different temperatures. These experiments always showed a change in specific resistance and Hall coefficient with temperature, however the change was always comparable. That means that the sample with the highest Hall coefficient at room temperature also shows the highest Hall coefficient at 77 K. In principle the characteristic values at 77 K are of importance since this is the operation temperature of the device. However by characterizing the Bi films at room temperature the optimum deposition conditions can also be found. Because the measurements in the PPMS required quite a long time, further characterization of the samples was performed at room temperature in a different system.

The sample is glued on a printed circuit board (PCB) and thin copper wires were glued on the surface with silver glue. The PCB is placed in between two permanent magnets with a magnetic field of 720 mT in the 5 cm gap between the magnets. The Hall measurements were carried out at three field values, two in the magnetic field, one for each direction, and one without the magnets. For each field value Hall measurements are performed for all possible connection configurations. The van der Pauw measurements are carried out at zero field. In principle two measurements are required to perform the van der Pauw calculation. For the van der Pauw measurements all eight possible connection configurations, which results in four sets of two measurements, were performed [116].

The van der Pauw measurements showed large differences between the two measured resistance values and also between the four sets of measurements, in some cases even up to one order of magnitude. Since the films were grown on square samples of 5×5 mm^2 and the connections are placed carefully in the

corners of the sample this was not expected. The large difference in resistance values is an indication that there might exists strong anisotropy in the resistance however is it not systematic. This is also confirmed by the Hall measurements which showed large offset voltages. Offset voltages can arise due to misalignment of the voltage readout connections, however the values were much larger what can be expected. Besides misalignment in the connections, the large differences in specific resistance and Hall coefficient can also arise from inhomogeneities in the film thickness. Since the sample is small compared to the size of the plasma of the sputter deposition this is not likely. Due to the large spread it is impossible to give accurate specific resistance and Hall coefficient values. One should also note that an important parameter in the calculations of the specific resistance and the Hall coefficient is the film thickness which is difficult to determine.

Despite all this there is a trend visible in the data, the specific resistance and Hall coefficient of the optimum sputtering power and argon pressure versus the temperature during deposition are displayed in figure 4.5. The highest Hall coefficient is obtained for a power of 100 W, at a pressure of 5×10^{-2} mbar and with a deposition temperature of 388 K and is 0.19 $\mathrm{cm^3C^{-1}}$ measured at room temperature. At these deposition conditions the maximum specific resistance of 685 $\mu\Omega$cm was also obtained. For all deposition conditions investigated, increasing the temperature to $T \geq 398$ K meant a strong decrease in specific resistance to ~ 50 $\mu\Omega$cm. At the same time the Hall coefficient decreased to $\sim 10^{-4}$ $\mathrm{cm^3C^{-1}}$. At $T = 373$ K irregardless of the deposition conditions the Hall coefficient and specific resistance are larger than for $T \geq 398$ K but in no case larger than the

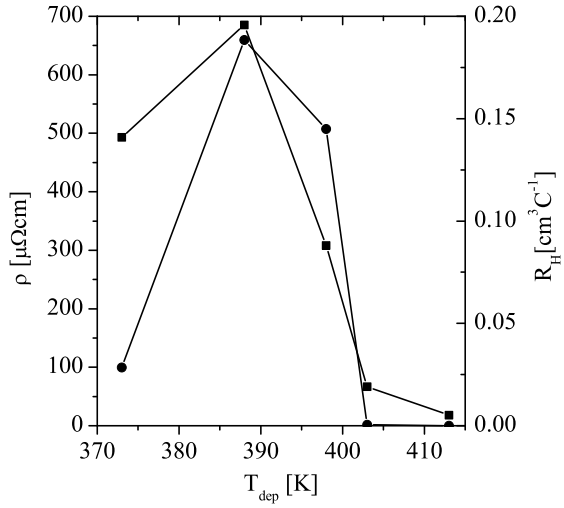

Figure 4.5: Specific resistance (squares) and Hall coefficient (dots) of the optimal sputtering power and argon pressure versus the temperature during deposition measured at room temperature.

values at $T = 388$ K.

Comparison of the found specific resistance with the data presented in figure 4.3b) shows that there exists good agreement between this value and the value obtained by RF-magnetron sputtering presented by Kim et al. Comparison of the Hall coefficient on the other hand, shows that the value presented in this thesis is a factor ~ 2 lower than the value of Kim et al. At 77 K the specific resistance and the Hall coefficient are obtained from an actual Bi Hall device hybrid magnetometer and were found to be $\rho \approx 1540$ $\mu\Omega$cm and $R_{\mathrm{H}} = 0.34$ cm^{3}C^{-1} respectively. Again the specific resistance has a comparable value with literature, now with the work of Schmidt et al. and the Hall coefficient is a factor of ~ 4 lower. The question rises what is causing this large difference. As mentioned in the work of Boffoue et al. the Hall coefficient is very low and is even changing sign when the temperature is decreased. In the same work the specific resistance is showing a trend which is comparable to other work. The low Hall coefficient in the work of Boffoue et al. is, as mentioned, attributed to the crystal structure which is for a large part perpendicular to the trigonal axis, which is the (003) direction, and for a small part (012) oriented. X-ray diffraction (XRD) analysis in the work of Kim et al. shows that there exists a strong preference for the (012) direction and there are very small (003) and (104) reflections. XRD analysis on the films presented here show a wide variety of reflections and there exists no strong preferential growth orientation. This might be a possible explanation for the reasonably good correspondence of the specific resistance and the rather weak correspondence of the Hall coefficient. It is unclear what is causing this difference. Basically the deposition technique is not very different but a possible explanation might be found in the substrate material. Although glass substrates, used in the work of Kim et al. and SiO_2 of thermally oxidized Si substrates used here are not very different but visual differences in growth of Bi deposited on thermally oxidized substrates and on deposited SiO_2 were noticed.

From a sensor point of view Bi is in principle a suitable material. In the next chapter in section 5.3 the results of the characterization presented here are applied in a Bi Hall device hybrid magnetometer. On the other hand the Hall coefficients obtained with this material are not exceptionally high and therefore the use of semiconductor materials is considered in the next section.

4.3 Silicon Doping by Implantation

Implantation of dopants in Si is a widely applied technique in semiconductor industry. Doping materials are typically group III or V materials depending if a p-type or n-type material is required. Doping implantation in SOI for applications in the semiconductor industry is of special interest because it enables high-speed complementary metal-oxide semiconductor (CMOS) devices. The parasitic capacitances can be reduced by utilizing the substrate [117].

Doping of SOI wafers is also of interest for application in a doped Si Hall device hybrid magnetometer. By implanting a SOI sample locally, via a photo

lithography mask, a well defined region can be given the desired doping density as derived in chapter 3. Because the thickness of the top Si layer of the SOI sample is well defined and wafers are available in a wide variety of thicknesses also the thickness of the resulting Hall device can be chosen at will.

Doping implantation itself is a rather straightforward procedure. Dopant can come from a target which can be a feed gas containing the desired species like BF_3 or AsH_3 or from a solid material that is heated. The atoms are ionized in an arc chamber and the desired ions are selected by mass separation which is much like the principle used in a mass spectrometer. The ion beam is focused with electrostatic lenses and accelerated with a linear accelerator. Typical acceleration energies lie between 5 – 200 keV. The wafer is homogeneously doped by scanning the beam uniformly over the wafer. The dose can be determined by measuring the ion current and penetration depth can be determined precisely by controlling the electrostatic field of the accelerator.

When an ion enters the wafer it starts to loose energy and the ion is considered to be implanted when it lost all its energy. Two mechanism for energy loss can be held responsible which are ion–electron interactions also known as Coulomb scattering and lattice interactions. During implantation the wafer is in most cases tilted a few degrees. If the incoming ions would penetrate the wafer parallel to the major crystal axis some ions would be able to travel deep in the material since the energy loss due to lattice interactions is very small. This effect is known as channeling. After the implantation process the substrate material is partially damaged and the dopant atoms do not occupy vacant lattice sites. By annealing the crystal structure is repaired and the doping is electrically activated.

Numerous papers have been published where doping implantation in SOI wafers is investigated [118–123]. This includes analyses on the depth profile of the implanted doping and the activation of the doping by thermal annealing. There are several methods to analyze the depth profile [124] but the most widely applied technique is secondary ion mass spectroscopy (SIMS). With this technique the chemical composition of the material is measured with a mass spectrometer while the surface is etched away. The doping activation is often characterized by Hall and resistance measurements which provides carrier mobility and density data that can be compared with bulk Si values.

This research is focused on implantation of arsenic (As) and boron (B) which yields an n-type and p-type semiconductor, respectively. As mentioned the Si is damaged by the doping implantation process and the material can in principle be repaired by an anneal step. There should however be at least a part of the Si top layer still crystalline to act as an recrystallization seed. In general B doping does not cause insurmountable problems. This material is relatively light and does not cause too much damage to the Si substrate. Even up to high implantation energies and thin Si top layers, the layer can still be recrystallized [118, 123]. In [123] B doping is investigated at energies ranging from 1–6.5 keV with a dose of 3×10^{14} cm^{-2}. When the samples were annealed at sufficiently high temperatures between 750 and 900 °C the active dose of boron is similar to that of bulk Si. Doping of As on the other hand poses much more problems. There have been numerous

reports that mention incomplete recrystallization which demonstrates itself by a decreased electrical activity with an increased doping density [118, 121]. In [118] SOI is doped with As at implantation energies between 50 and 125 keV with a dose of 2×10^{15} cm^{-2}. Electrical investigation showed incomplete recrystallization after the anneal step at 1000 °C.

In [119] samples were doped at 10 and 40 keV with a dose of 5×10^{15} cm^{-2}. At the lowest of the doping energies the top Si layer recrystallized after an anneal step at 850 °C for 30 min. For the higher implantation energy of 40 keV TEM imaging showed a polycrystalline top Si layer. Another drawback of As doping is shown in [120, 125, 126] where TEM images show that As has the tendency to pile up at the Si/SiO_2 interface after annealing. Nevertheless As doping is possible with good recrystallization by limiting the dose and acceleration energy.

In chapter 3 an optimum As dopant density of $N_D = 4 \times 10^{15}$ cm^{-3} was calculated. If one assumes that all the doping is concentrated in the top Si layer, which has a thickness of 50 nm, this would mean that a dose of 2×10^{10} cm^{-2} would be required. This is far from the values of the cited articles where unrepairable amorphization occurred. In practice this dose value is higher since the doping profile is stretched out and reaches into the underlying SiO_2 layer. Nevertheless it is unlikely that such high values are required and since n-type semiconductor is preferred from a sensitivity and device resistance point of view both doping of Si with As as well as with B are further investigated.

The optimum dopant dose obtained in chapter 3 is a theoretical value. Experimental values obtained from literature show that in practice the optimal dopant dose should be higher, $\approx 2 \times 10^{17}$ cm^{-3} [127, 128]. For the largest part the difference can be attributed to the mobility. Compared to the mobility graph shown in figure 3.2b) the transition from mobility characterized by lattice vibrations to impurity scattering is occurring at higher doping levels. For the graph shown in figure 3.5a) this means that the minimum in the device resistance is also shifting to higher doping densities. Therefore the aim is to obtain a doping level of 2×10^{15} cm^{-3} in the simulations and experiments described in this section. Note that also for this dopant dose the threshold values for amorphization are in principle not reached.

4.3.1 Simulations

In order to determine the optimal parameters the implantation process was simulated using the Athena simulation package from Silvaco [129]. This package implements various simulation methods like Monte Carlo simulations and table interpolation methods. The Monte Carlo simulation mode uses a statistical calculation of the position of implanted ions in the material and as such determines the final location of every implanted ion. The table interpolation method uses data from experiments conducted at University of Texas, where various materials were implanted at different energies. The resulting doping profiles from these experiments were then measured by SIMS. The simulation interpolates between these data points and is a lot faster than the Monte Carlo method. Therefore the

table-interpolated simulations were used by default.

A number of parameter sweeps were made to determine the optimum circumstances for ion implantation. In addition to an exploration of the implantation parameters, the package is capable of simulating annealing procedures. The effect of implant doses, acceleration voltage, oxide layer thickness, anneal temperatures and anneal times are simulated by changing one parameter at a time. For all simulations a setup was used with a 50 nm top Si layer on a 150 nm thick SiO_2 layer and a Si bulk of about 800 μm. The simulations are carried out for both B and As doping and the wafer is tilted 7 degrees.

In figure 4.6 implantation profiles of As and B for various acceleration voltages are displayed. In these simulations the acceleration voltage is varied, whilst keeping the other implantation parameters constant. The dose for As implantation is 4×10^{14} cm^{-2} and for B is 5×10^{12} cm^{-2}. For all graphs holds that when the acceleration voltage is increased, the peak of the doping profile shifts further into the material.

The available ion implanter from High Voltage Engineering [130] works with energies typically between 30 and 500 keV. The graphs in figure 4.6a) and 4.6c) show that the required doping profiles require much smaller acceleration energies. An additional layer of SiO_2 is added on top of the sample. Because the dopant is implanted through the top SiO_2 layer, the acceleration energy can be increased to within the specifications of the apparatus. In figure 4.6b) and 4.6d) a 95 nm SiO_2 is added to the structure. This additional layer also yields the benefit of a more homogeneous implantation profile in the Si which is beneficial to the electrical properties of the material. In figure 4.6b) it can be seen that the concentration of As ions in both the grown oxide and in the top of the buried oxide layer is higher than in the 50 nm Si layer. This can be attributed to the nuclear stopping power which is higher for SiO_2 than for Si. The mean implantation depth of the As ions is significantly smaller than that of the B ions. When implanting without oxide at 30 keV, the peak concentration of the As ions is in the Si while for the B ions the peak lies deep in the buried oxide. This can be attributed to the size of the ions. The As ions larger than the B ions and are therefore encountering much more scattering. It can be seen that the height of the peak is decreasing for higher acceleration voltages. Since the amount of dopant introduced into the material is constant, the integral over the doping profile is equal for all acceleration voltages. When the acceleration voltage is increased, the ions penetrate deeper into the material and the width of the distribution increases. It can be seen in figure 4.6d) that the shape of the concentration profile in the Si layer depends on the part of the distribution that lies in the Si layer. The shape differs for the cases where the peak lies in the deposited oxide, the silicon layer or the buried oxide.

From these simulations it can concluded that an acceleration voltage of 80 keV and a dose of 4×10^{14} cm^{-2} for As is optimal for this purpose, and 30 keV and a dose of 2.5×10^{12} cm^{-2} for B. These values are for the samples on which a 95 nm SiO_2 layer is grown before ion implantation.

In order to electrically activate the implanted dopant material, the samples need to be annealed. This means thermal energy is added to the dopant ions,

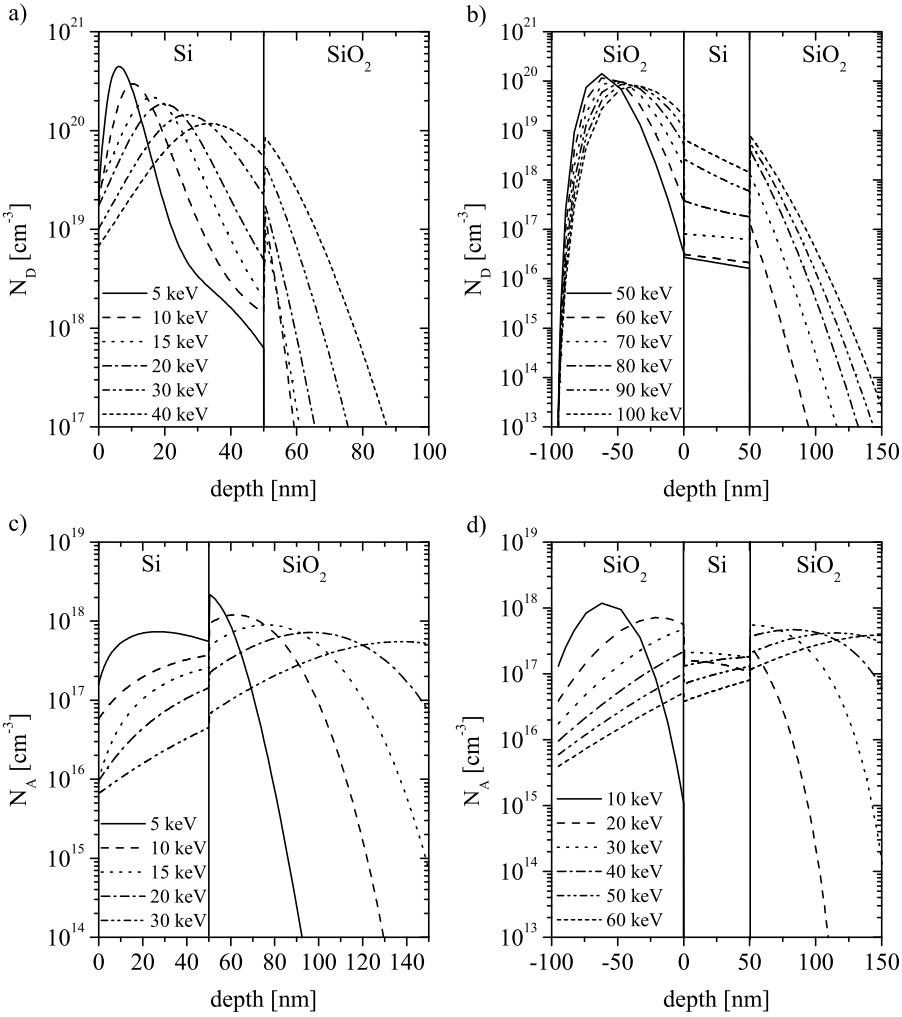

Figure 4.6: Doping density vs. depth for As with a dose of 4×10^{14} cm^{-2} shown in a) and b) and B with a dose of 5×10^{12} cm^{-2} shown in c) and d) for several acceleration energies in a SOI wafer with a 50 nm top silicon layer and a 150 nm SiO_2 layer. In b) and d) an additional 95 nm thick SiO_2 layer is added to obtain practical acceleration energies within the range of the apparatus. For all simulations an implantation angle of 7 degrees is chosen.

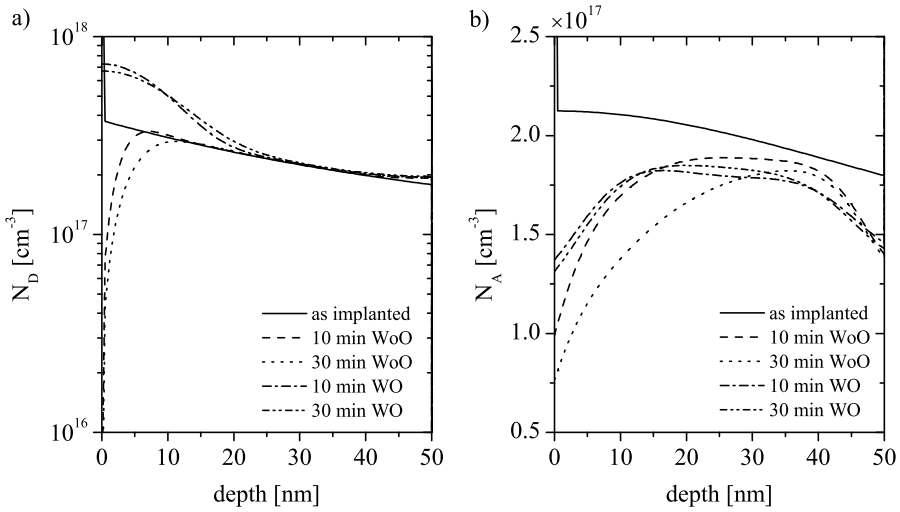

Figure 4.7: Simulation of the doping depth profile in the top 50 nm Si for a) As doping and b) B doping. The graphs show the results before annealing and for a 10 min and 30 min anneal step with the oxide layer removed before annealing (WoO) and with the oxide still in place during annealing (WO).

enabling them to diffuse and occupy vacant lattice sites. The longer the samples are annealed, the more diffusion can occur. The amount of energy introduced into the sample also influences the dopant activation. Reports in literature show that at a temperature of 900 °C the largest part of the dopant becomes electrically active. That means that not all dopant atoms are active but a further increase of the temperature does not provide further electrical activation [121, 123]. It is possible to perform the anneal procedure in-situ with the deposition of the superconducting YBCO flux concentrator and the maximum temperature this system can reach is about this temperature in vacuum.

In figure 4.7 several anneal procedures are shown for As in figure 4.7a) and B in figure 4.7b). Note the logarithmic scale for the As doping and the linear scale for the B doping. The graphs show the situation after implantation and for 10 min and 30 min anneal times with and without the SiO_2 present.

The results for the As doped situation shows that when annealing with the grown oxide still on top, ions move from the grown oxide layer into the silicon layer. The same happens with the buried oxide layer, but shows a lower change in concentration due to a lower concentration in the buried oxide. There is not much difference between 10 and 30 min. All ions that move from the oxide into the Si must come from the neighboring layers. If the oxide is stripped off before annealing, diffusion out of the material at the surface of the silicon layer will occur, lowering the net dopant concentration in the silicon.

When a similar annealing step is applied to the B doped samples, the resulting

doping profile will be more parabolic as can be seen in figure 4.7b). The boron concentration is at a maximum in the center of the silicon layer between the two oxide layers. It looks that some ions migrate into the buried oxide layer, which results in a lower concentration in the lower 10 nm of the silicon, whilst more is lost in the top of the silicon layer. If the grown oxide layer is still on the sample during annealing, there is not much difference between 10 and 30 min anneal steps.

The effect of annealing happens fast and afterwards no big changes occur in the doping profile. One should however note that simulations do not provide any information on the electrical activation of the material but merely on the distribution of it. Reports in literature show that there is a significant difference in the electrical activity between 10 min and 30 min anneal time with the best results for the latter [123]. If the oxide is stripped off before annealing, the concentration will be lower after the annealing step. Both As and B simulations show that the effect of annealing is optimal with the grown oxide still on the sample.

4.3.2 Measurements

Samples of Si[100] SOI wafers were doped with the mentioned doping density and acceleration energy. SOI wafers were used with a 50 nm top Si layer and a 150 nm SiO_2 interlayer, the same as in the simulations. The wafers are SIMOX SOI wafers from a modified low dose (MLD) process and the wafers contain only a little intrinsic doping. The doping is boron which results in a specific resistivity of 10 – 20 Ωcm.

The characterization of the layers is comparable to that of the Bi films. This means van der Pauw measurements were carried out to obtain the specific resistance and Hall measurements for the Hall coefficient from which together the carrier density and mobility can be derived. Since the carrier density and mobility are strongly temperature dependent, the characterization is carried out in the PPMS system for several temperatures. The samples used in these experiments were not supplied with a photo resist mask so the whole wafer is doped. Electrical connections were made by wire bonding directly on the Si. Two samples were prepared for both dopant materials where one was annealed with the SiO_2 layer on top and the second one without the SiO_2.

Measurements on the B doped samples showed in both cases, annealed with and without oxide, resistance values which were unmeasurable high irregardless of the temperature. The measurements on the As doped sample did give measurable resistance values. No significant difference was observed between the two As samples which were annealed with and without the oxide layer. The results presented here are of the substrate where the oxide layer was removed before annealing.

In figure 4.8 the carrier density and mobility as a function of temperature are displayed. When one assumes a single dopant type, n or p, then a decrease in the carrier density can be expected when the temperature decreases. The material is then in the freeze out range and with decreasing temperature not all dopant atoms are excited and attributing to the carrier density. From that point of view the small increase of charge carriers below 100 K cannot be explained. Above

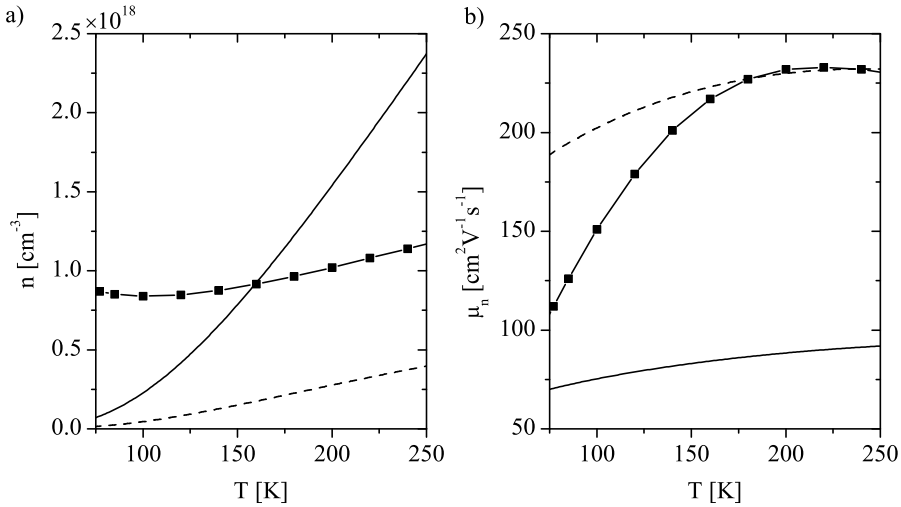

Figure 4.8: Measurements (solid line with squares) of the a) carrier density and b) mobility for an As doped SIMOX SOI wafer where the SiO_2 top layer is removed before annealing. The solid line represents a model fit of the carrier density at 160 K and corresponds to a doping density of $N_D \approx 2.4 \times 10^{19}$ cm^{-3}. The dashed line represents a fit of the mobility at the maximum values and corresponds with a doping density of $N_D \approx 1.55 \times 10^{18}$ cm^{-3}.

this temperature an increase of the carrier density with the temperature is visible. Attempts were made to fit the theoretical expression for the carrier density, of equation (3.5), with the data. Results showed that, irregardless of the dopant density in the model, there exists a large difference in the slope of the carrier density with respect to the temperature. That means, one is able to obtain the correct carrier density for a certain temperature but the corresponding dopant density does not provide a good fit for other temperatures. An example is given in figure 4.8 where the solid line indicates a fit of the carrier density at 160 K. The model values presented here correspond to a doping density of $N_D = 2.4 \times 10^{19}$ cm^{-3}. It was possible to obtain a reasonable fit for the mobility of equation (3.9) with a doping density of $N_D \approx 1.55 \times 10^{18}$ cm^{-3} which is shown as the dotted line in figure 4.8. Comparison between the model values of the carrier density for the fit of the mobility shows that the slope above 100 K is in good agreement however the model values lie far below the measured data points.

In general it can be concluded that there exists a rather weak correspondence between the model values of the carrier density and mobility with the measurements. When one assumes that there is a single carrier type an increase of the carrier density below 100 K can not be expected. These effects can be observed when there exists a mix of both n and p type carriers. In principle this is the case since the SOI contains a small B doping however the density is much lower

than the As density and such large differences can therefore not be expected. As mentioned it is known that As implanted in Si is not fully activated after thermal annealing. This might give an indication for the weak corresponding model value fits and the measurements.

Although the fitting of the data with the model does not provide satisfactory results, the overall conclusion is forced upon that the dopant density in the material is much too high. Based on the carrier mobility fit $N_D \approx 1.55 \times 10^{18}$ cm^{-3} and based on the carrier density fit $N_D \approx 2.4 \times 10^{19}$ cm^{-3} which should be compared with $N_D \approx 2 \times 10^{17}$ cm^{-3} where was aimed for. As already mentioned in the simulations, the maximum of the As doping profile was aimed to be in the covering SiO_2 layer while in the case of the B doping the maximum should be in the Si top layer. Since no conduction was found in the B doping and the carrier density is too high in the case of As doping, the covering SiO_2 layer appears to be more transparent for the doping implantation than expected based on the simulations. Or in other words the doping is implanted deeper in the substrates than expected, causing the maximum of the B doping in the SiO_2 interlayer or even deeper in the Si substrate and the maximum of the As doping in the Si top layer.

Nevertheless a Hall coefficient of $R_H = 7.2 \times 10^{-6}$ m^{3}C^{-1} was obtained at 77 K which should be compared with $R_H = 1.3 \times 10^{-6}$ m^{3}C^{-1} of Bi as shown in [46] or $R_H = 0.34 \times 10^{-6}$ m^{3}C^{-1} which was obtained in a Bi based device presented further on in this thesis in section 5.3.2. Since the Hall coefficient of doped Si is already higher with far from optimal implantation parameters there appears to be a large potential for this type of Hall sensors. In a second run of implantation of experiments the acceleration voltage was varied between 30 and 70 keV. The resistance of the samples doped with the highest acceleration voltage showed a very large increase and it was not possible to obtain good Hall and van der Pauw measurements from these samples. This can be caused by the method of contacting the sample, which is wire bonding, or the sample size, which is 1 cm^2 and much larger than the actual sensor.

4.4 YBCO Deposition on Silicon

YBCO deposition on Si is an interesting area of research because it enables the integration of semiconductors and superconductors in hybrid devices and so in hybrid magnetometers based on a doped Si Hall device and a YBCO flux concentrator. Thin film pulsed laser deposition of YBCO on for example STO substrates is a straightforward process nowadays which results in good quality films with critical temperatures up to $T_c = 92$ K. This particular substrate has a good lattice match with YBCO and more over has a quite comparable thermal expansion coefficient (TEC) to that of YBCO. In this section pulsed laser deposition (PLD) of YBCO on Si and in particular on SOI wafers is discussed.

For YBCO deposition on Si, SOI wafers are preferred over conventional Si wafers. Due to the large differences in the TECs, strain will cause cracks in the deposited film deteriorating the superconducting properties. In the deposition

on conventional Si substrates the thickness of the film is limited to $\sim$ 50 nm in. Thicker films exhibit cracks and show degraded superconducting characteristics [131, 132]. When SOI wafers are used the strain is relaxed to the SiO_2 interlayer [133] and YBCO film thicknesses of over $\sim$400 nm can be realized [105]. In table 4.1 the TECs of YBCO and Si are given [134, 135]. In [134] only a single value for the TEC of YBCO is mentioned and this is assumed to be linear with temperature. In [135] the TEC of Si is given for numerous temperatures between $\sim$300 K and $\sim$1500 K and is shown not to be linear with temperature. Two values are mentioned in table 4.1, one close to the deposition temperature and the other close to room temperature. The temperature during deposition is 780 °C and at this temperature the difference in the TEC between the two materials is about a factor of 3. For lower temperatures this value is even increasing.

Despite the fact that the SiO_2 interlayer in SOI substrates relaxes the stress, direct deposition of YBCO on SOI results in poor films. Interdiffusion of oxygen from the YBCO will deteriorate the superconducting properties. Reasonably good results have been obtained by deposition of YBCO on a buffer layer of YSZ [133] and CeO_2/YSZ [105]. The choice for the second buffer layer is based on better lattice match of the materials. Moreover it is known that there is, to some extent, interdiffusion of oxygen between YSZ and YBCO and this is prevented by a CeO_2 layer. In table 4.1 an overview of the lattice parameters of the different materials is given. YBCO grows diagonally on top of the other material and therefore the parameters of epitaxy are displayed. Here a^* is the diagonal lattice parameter given by $a^*=a/\sqrt{2}$. For YBCO the mean lattice parameter $\overline{a}$ of the a and b direction is given. From this data one can calculate that the mismatch between YBCO and CeO_2 is only 0.52% compared to 5.7% between YSZ and YBCO [136]. The critical temperature in both cases is $T_c \approx 88$ K [105, 133]. The films which have been deposited with only a single buffer layer of YSZ show cracks [133]. These are not visible in the films with the YSZ/CeO_2 buffer layers. The critical current density of the YBCO/CeO_2/YSZ films is $J_c = 2\times10^6$ Acm^{-2} [105]. In [137] the critical current density of a YBCO/YSZ film is determined of a 6 μm wide strip and was found to be $\sim2\times10^4$ Acm^{-2}.

Table 4.1: Lattice parameters, parameters of epitaxy and thermal expansion coefficients of Si, YSZ, CeO_2 and YBCO.

Material	Lattice par. [nm]	Par. of epitaxy [nm]	TEC $\times10^{-6}$ [K^{-1}]
Si	a = 0.5428	a^* = 0.384	2.69 @ 63 °C 4.27 @ 786.5 °C
YSZ	a = 0.514	a^* = 0.364	9.7
CeO_2	a = 0.541	a^*=0.383	12.6
YBCO	a = 0.38185 b = 0.38856 c = 1.16805	$\overline{a}$ = 0.385	13.4

Table 4.2: Pulsed laser deposition conditions of YSZ, CeO_2 and YBCO.

Deposition conditions	YSZ	CeO_2	YBCO
Temperature [°C]	800	800	780
Atmosphere	Ar, O_2 (32 s)	O_2	O_2
Pressure [mbar]	0.02	0.02	0.25
Repetition rate [Hz]	7	7	4
Energy Density [mJcm^{-2}]	2.1	2.1	1.4
spot size [mm^2]	3.35	3.35	5.56

As was already shown in chapter 3 it is desirable to have a high critical current density. This permits a narrower constriction, given a certain maximum magnetic field, and this improves the coupling with the sensor. Since the critical current density differs 2 orders of magnitude between the films with and without the second CeO_2 buffer layers, the deposition of YBCO/CeO_2/YSZ on SOI is further investigated. Different SOI samples were used where the Si top layer thicknesses range from 300 nm up to several tens of micrometers. For comparison also some depositions were carried out on conventional Si samples.

The first buffer layer deposited on Si is YSZ. Si typically contains a native oxide layer of a few nanometers. This layer is amorphous and one could therefore expect that this layer has to be removed. In literature papers have appeared where the native oxide layer is removed by HF etching but there are also papers where the native oxide is left untouched [133]. The initial stage of YSZ deposition is the decomposition of SiO_2 to SiO, the formation of ZrO_2 and the desorption of SiO [138, 139]. The deposition conditions used for the layers are given in table 4.2. The YSZ deposition is performed in two steps. First the deposition is carried out in an Ar atmosphere which "consumes" the native oxide layer and introduces the YSZ[100] growth. After 32 s the deposition is stopped and the Ar atmosphere is replaced by O_2 [140]. The deposition is then continued until the desired thickness of the YSZ film is reached. Note that the duration of the initial deposition in the Ar environment is independent on the total duration of the deposition. The CeO_2 film is deposited under the same conditions as the YSZ layer however only the O_2 atmosphere is used. The YBCO deposition involves slightly different parameters under a higher pressure and with different energy density, spot size and repetition rate.

Figure 4.9a) shows a typical X-ray diffraction (XRD) measurement for in this case a SOI sample with an top layer thickness of ∼300 nm. This measurement shows all the YBCO[001] reflections in the scan range. This suggests strong c-axis oriented growth. At about 61.8 and 65.8 degrees two small additional peaks are visible around the YBCO[008] reflection which are caused by the X-ray filament. No difference could be observed between the XRD measurements of the films deposited on SOI and on Si wafers. Rocking curves of some of the reflections were made. The full width half maximum (FWHM) value of the YSZ[200] was

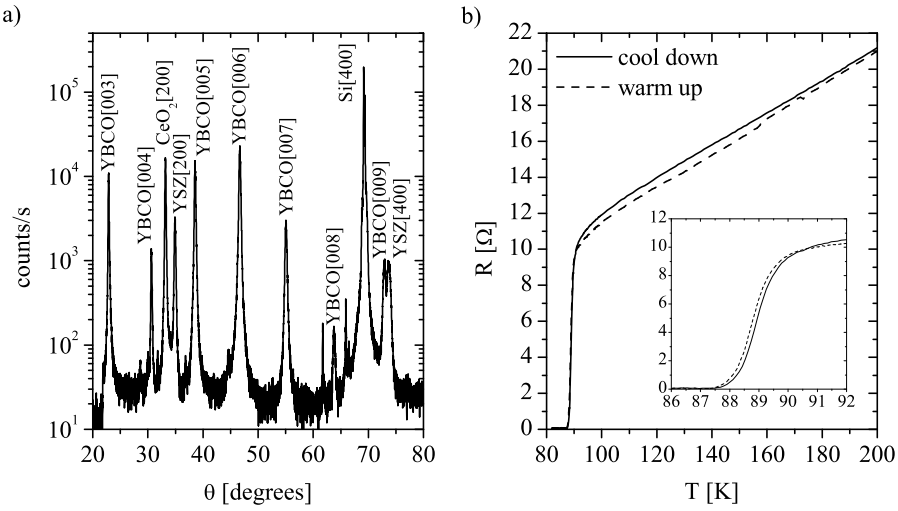

Figure 4.9: a) Typical XRD measurement of a YBCO/CeO_2/YSZ film on a 300 nm SOI wafer. The measurement shows all the YBCO[001] reflections which means that the superconductor is strongly c-axis oriented. b) Temperature dependent resistance measurements of the corresponding film revealing a critical temperature of 87.5 K.

determined to be 0.93°, of the CeO_2[200] 0.99° and of the YBCO[005] 1.57°. These values are comparable to those that can be found in literature [133].

Both samples were used in resistance vs. temperature (RT) measurements. In the case of the YBCO film deposited on conventional Si the resistance was in the Mega Ohm range at room temperature and was increasing instead of decreasing for lower temperatures. Optical analysis of this sample showed a high density of cracks along the crystal axis of the sample, probably caused by the relatively large difference in TECs between substrate and the buffer layers and superconducting film. The film on the SOI substrate on the other hand did not show any cracks. This sample shows superconductivity at 87.5 K with a transition region of 3K. The RT measurement is displayed in figure 4.9b). The electrical connection were made to the sample with a clamping mechanism. The resistance value as displayed in the graph is an actual measured resistance but since the film is not structured into a specific shape no absolute resistivity values can be obtained from this measurement. The graphs shows two curves, one while cooling down and one while warming up the sample. In the inset the region around the critical temperature is shown. A small difference between the two data sets can be observed. This can be attributed to a small temperature difference between the sample and the temperature sensor in this system which are not exactly at the same location. In the resistance above the critical temperature also a difference between cool down and warm up can be noticed. This difference is, with respect to the temperature,

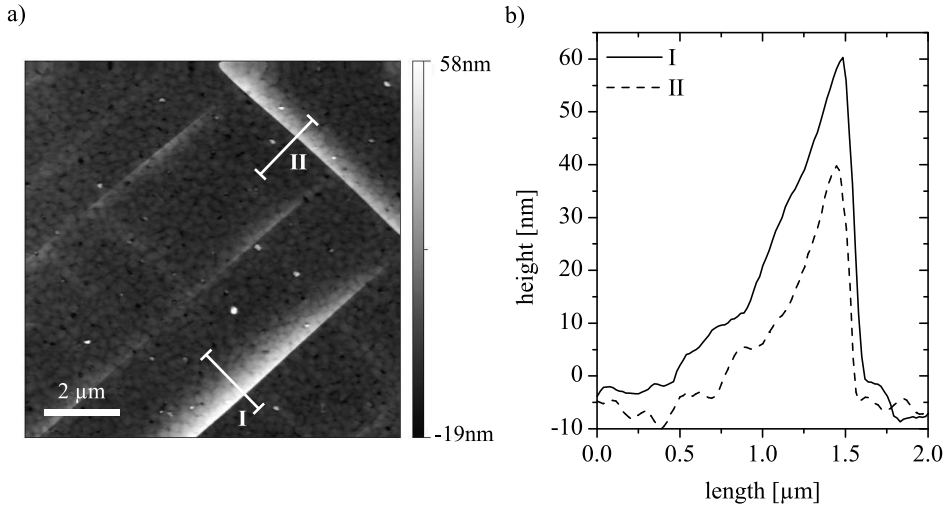

Figure 4.10: AFM image of a YBCO/CeO_2/YSZ film deposited on a SOI substrate with a 50 nm top layer b) Height profiles at two positions of the AFM image shown in a) indicated with I and II.

larger and can not be attributed to the placement of the temperature sensor and the sample. This might be attributed to thermal stress which causes additional cracks during cooling. To exclude the possibility of further cracking the sample was thermo cycled 5 times from room temperature to 77 K but no further changes, that means changes in the the T_c and resistance value above T_c, could be observed.

Finally deposition experiments were carried out on SOI films with a 50 nm top layer which are the substrates that will be used for the doped Si Hall device hybrid magnetometer. The same deposition settings were used as in the discussed experiments. These samples did not show superconductivity and optical inspection showed what appeared to be cracks in the film. Closer inspection with an atomic force microscope (AFM) showed the results displayed in figure 4.10. Figure 4.10a) shows the actual AFM image whereas figure 4.10b) depicts the height profiles at two positions, I and II, as indicated in figure 4.10a). As mentioned in previous experiments on for example conventional Si wafers, cracks were observed in the YBCO. This was attributed to the large difference in the TECs of YSZ, CeO_2 and YBCO compared to Si. The TECs of the oxides are all significantly larger than the TEC of Si. This means that when after deposition the material is cooled down the deposited layers all shrink faster than the Si and the film cracks and leaves spaces between resulting grains. The AFM image in this case imposes the conclusion that the opposite is happening and the Si layer underneath the deposited films is buckling and since the covering layers all shrink faster, is pushed upwards which results in the grains which on one side bend upwards.

A better matching of the layer thicknesses could prevent this. The deposition times used in these experiments were 10 min for YSZ, 5 min for CeO_2 and 8 min

for YBCO. Based on previous pulsed laser deposition characterizations of these materials it was assumed to result in film thicknesses of 100 nm, 50 nm and 240 nm for YSZ, CeO_2 and YBCO respectively. An attempt was made to measure the thickness of the total three layers of materials by X-ray reflectometry however due to the number of layers and the roughness of the film this was not possible. A film of YSZ was deposited under the mentioned deposition conditions and duration. The film thickness of the film was measured with X-Ray reflectometry and showed a film thickness of ≈220 nm. With the given deposition time this means a deposition rate of 22 nm min^{-1}. This means that the deposition rate is over a factor of 2 larger than expected. The YBCO thickness was measured after a photo lithography process and H_3PO_4 etching. The step height of this sample was measured with an alpha stepper and showed a film thickness of ∼170 nm which means a deposition rate of 21 nm min^{-1}. The thickness of the CeO_2 was not measured since no selective etchant was found. However since it is deposited under the same conditions as the YSZ film the deposition rate is estimated to be the same.

It may be expected that the total stack of these materials had a thickness of approximately 500 nm on top of a 50 nm Si layer. Due to this large difference in thickness one can expect a buckling of the Si top layer. Since the previous depositions were carried out on much thicker SOI wafers this effect was not visible in those samples. In [105] good films of YBCO were deposited on 30 nm and 15 nm thick YSZ and CeO_2 films respectively. The deposition duration of the YSZ film was decreased to 3 min which should result in a 66 nm film and of the CeO_2 film to 1 min which means a 22 nm film. The deposition duration of the YBCO film was not changed. The resulting films did not show any indication of cracking or buckling of the film. The T_c of the film was measured by the already mentioned clamping technique. Moreover the film was structured into narrow strips and the J_c and T_c were measured.

In figure 4.11 a four point RT measurement is displayed on a 10 μm wide strip. In the graph two lines are visible one while cooling down and one while warming up. As in the case of the RT measurement of figure 4.9, here also a small temperature difference between sensor and sample causes slightly deviating critical temperatures. In both cases the transition region is about 3 K wide. The critical offset temperature is about 88.5 K for the cool down graph and about 90 K for the warming up. The same critical temperatures were measured for the unstructured film with the clamping technique. The critical current of the strip is 0.5×10^6 Acm^{-2}.

4.5 Summary

Some critical production steps in the fabrication of hybrid magnetometers are highlighted. An overview of the production process is given for the Bi as well as the doped Si based hybrid magnetometer.

RF-sputter deposition of Bi is discussed which includes characterization by optical inspection as well as electrical measurements. The general conclusion is

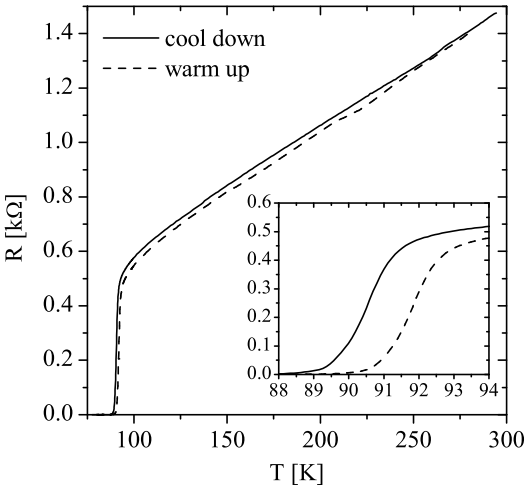

Figure 4.11: Temperature dependent resistance of a YBCO/CeO_2/YSZ film with thicknesses of 170, 22 and 66 nm respectively on a 50 nm SOI wafer.

that Bi grows in a rather rough and droplet like fashion. Moreover the deposition on different underlying materials shows strong variation in the growth which is problematic in the device realization. The electrical characterization of the films was difficult due to a large anisotropy in the films.

Doping implantation into Si is discussed which includes simulations and electrical characterization. From simulations the optimum doping conditions were obtained. In order to have realistic values for the acceleration voltage within the doping implanter's operation range, an additional SiO_2 layer was grown on top of the substrates. Electrical characterization of the doped samples showed that the doping was implanted too deep in the material which suggests that the covering SiO_2 is more transparent for the doping than expected based on the simulations. Nevertheless the obtained Hall coefficient with these sub-optimal doping conditions is higher than for Bi.

The deposition of YBCO on SOI substrates is discussed. YBCO is deposited by pulsed laser deposition with two buffer layers of YSZ and CeO_2. The buffer layers are added to obtain the desired YBCO growth direction and for a better lattice match. The films were characterized by XRD analysis and electrically with T_c and J_c measurements. The results showed that the buffer layers should be as thin as possible in order to prevent thermal stress in the underlying Si layer. The T_c and J_c measurements were comparable to values in literature.

CHAPTER

5

Hybrid Magnetometers in Practice

Abstract

The sensitivity of Hall devices can be enhanced by flux concentration. However due to vortex movement induced noise in the flux concentrator, the device resolution can be limited. The noise due to vortex movement is derived and compared with the intrinsic noise of the Hall sensor. Bi Hall device hybrid magnetometers have been characterized. Besides the characteristic values the measurements showed additional features that can be attributed to the strips in the concentrator which are meant to prevent vortex trapping in the concentrator. The doped Si Hall device hybrid magnetometer are equipped with a double concentrator layout. The characterization of these devices is impeded by difficulties in the connection between the Hall sensor and the electrodes.

5.1 Introduction

In this chapter the operation of hybrid magnetometers in practice is treated. It consists of a discussion on the vortex movement induced noise and the characterization of the Bi and doped Si based hybrid magnetometers.

In the first section the effect of thermally induced vortex movement on the field resolution of the device is presented. During the cooling process of the device in an unshielded environment, flux vortices can be trapped in the superconducting body. Thermal hopping of these vortices give rise to $1/f$ noise. In chapter 2 the critical magnetic induction of thin film strips is determined. The critical field provides an upper limit, below which superconducting sensors like SQUIDs and hybrid magnetometers can effectively be operated. In chapter 3 the design of hybrid magnetometers is discussed. In a follow up, based on the findings in chapter 2, slotted and unslotted concentrator designs were considered in chapter 3. In the derivation presented here the vortex movement induced noise is determined of an unslotted flux concentrator. Since the critical field of such a relatively large area of superconducting film is practically zero, a number of vortices will be trapped in the superconducting body. The noise level is determined by the cooling field and the film quality.

In the second section the characterization of the Bi based Hall devices is presented. This includes a description of the measurement method in which field sweeps are applied to the device beyond the maximum magnetic field. This results in hysteresis graphs which reveal the device operation with and without an active concentrator. The measurements include investigation of the effect of the bias current on the maximum magnetic field range and the coupling between concentrator and the sensor. Moreover the effect of temperature on the maximum magnetic field range is investigated and the effect of the slotted washers on the device behavior.

The third section contains the results on the doped Si Hall sensor based hybrid magnetometers. In this section the fabrication is discussed with a focus on the connection between the electrodes and the Hall element. The etching of the contact holes is performed by means of Ar ion etching which exhibit some specific drawbacks which make it more difficult to connect electrodes on the sensor.

5.2 Vortex Movement Induced Noise

In the theoretical derivation presented in chapter 3 the coupling between flux concentrator and Hall sensor was optimized in order to maximize the device sensitivity. As shown in chapter 3 the flux concentrator can enhance the sensitivity of the device up to several orders of magnitude depending on the desired maximum magnetic field. However, it is important that the concentrator itself does not produce excess noise which in its turn limits the device field resolution. Noise can arise from the thermal movement of trapped vortices in the superconducting body and has been observed in $YBa_2C_3O_{7-\delta}$ (YBCO) films [141–143]. The effect

of flux movement on the induced noise has been investigated in flux transformers coupled to SQUIDs [144] and directly coupled magnetometers based on SQUIDs [145, 146].

The induced noise caused by thermal movement of trapped vortices in the superconducting body of hybrid magnetometers is determined. A distinction should be made between direct and indirect noise contributions. In the first case, the Hall sensor directly senses the movement of the vortex, since the field lines have to close around the concentrator and hereby couple field to the sensor. In the latter case, the motion of vortices induces a screening current in the flux concentrator and this current induces magnetic field on the Hall sensor. In [144] a situation is considered of a flux transformer with an input coil directly above a SQUID. Analyzes of both the direct, as well as the indirect noise, in [144] showed that the indirect noise contribution is much larger and the direct noise contribution can be neglected. Since the concentrator in the hybrid magnetometers considered here is next to the sensor, the direct noise influence is believed to be even smaller. Relatively, the ratio between indirect and direct noise is believed to be comparable and therefore the analyzes in this section focus on the indirect noise contribution.

Because of symmetry it is more straightforward to derive an expression for the noise of square washer concentrators. This is because one of the parameters in the model, the width of the concentrator, is equal on all sides in a square washer layout and therefore an expression for this situation is derived here. Since the length scales of the double concentrator layout are in the same order of magnitude as the single square one, the noise contribution for the double concentrator will be in the same order of magnitude.

Consider a vortex displacement δr across a square-washer flux concentrator of width $w = (D - d)/2$, where D, and d, are the outer and inner dimensions of the concentrator, respectively. This displacement produces a flux change of $\delta\Phi \approx \Phi_0 \delta r/w$. For N uncorrelated vortices per unit area in the superconducting body of the flux concentrator, each with spectral density $S_\mathrm{r}(f)$ for radial motion, the spectral density of flux noise is [144]:

$$S_\Phi = N S_\mathrm{r}(f) \int_\mathrm{A} \left(\frac{\partial \Phi}{\partial \mathrm{r}} \right)^2 \mathrm{d}A, \tag{5.1}$$

where A is the area of the concentrator for which holds $A = D^2 - d^2$. Substitution of the expression for $\delta\Phi$ in equation (5.1) and integration over the area A yields [145]:

$$S_\Phi = 4 N S_\mathrm{r}(f) \Phi_0^2 \left(\frac{D + d}{D - d} \right). \tag{5.2}$$

Given the total induction of the concentrator expression for the screening current noise $S_{\mathrm{I_{scr}}}$ can be obtained for which holds:

$$\sqrt{S_{\mathrm{I_{scr}}}} = \sqrt{S_\Phi}/L_{tot}. \tag{5.3}$$

The effective field noise on the Hall sensor can now be determined by substituting

$\sqrt{S_{\mathrm{I_{scr}}}}$ for I_{scr} in equation (3.17). When the effective field noise $\sqrt{S_{\mathrm{B_{y,eff}}}}$ is inserted in equation (3.11) for B_y the noise is expressed in the Hall voltage.

Consider a square washer device where the concentrator has an outer diameter of $D = 8$ mm and an inner diameter of $d = 3$ mm. The effective area of this concentrator is $A_{\mathrm{eff}} = 2.4 \times 10^{-5}$ m^2 as can be calculated with equation (3.23). The total inductance is $L_{\mathrm{tot}} = 5.98$ nH calculated with equation (3.21) and with a slit inductance of 0.4 pHμm^{-1}. High quality films of YBCO on well matching substrates like STO typically show a $1/f$ noise of $4NS_{\mathrm{r}}(1\mathrm{Hz}) \leq 10^{-9}$ Hz^{-1} at a cooling field of 50 μT [143, 145]. For the analyzes presented here we take the upper limit of this range, $4NS_{\mathrm{r}}(1\mathrm{Hz}) = 10^{-9}$ Hz^{-1}. Substitution of this value and the dimensions of the concentrator in equation (5.2) yields a flux noise of $S_\Phi = 2.2 \times 10^{-9}$ Φ_0^2Hz^{-1}. Suppose we take a flux concentrator with a maximum magnetic field $B_{\mathrm{max}} = 5$ μT. One can calculate with equation (3.24) that the width of of the constriction is 5 μm when the critical current density is 2×10^6 Acm^{-2} and the thickness of the concentrator is $d_{\mathrm{YBCO}} = 200$ nm. Note however that this device can be cooled down in a 50 μT field and it can measure variations of ± 5 μT around this value. The flux noise is substituted in equation (5.3) and the resulting current noise in equation (3.17). This yields the effective field noise on the sensor which is substituted in equation (3.11) which gives the noise in the Hall voltage. For a Hall device with dimensions, $l = 400$ μm, $b = 250$ μm and $d = 50$ nm, power density $P_{\mathrm{d}} = 100$ kWm^{-2} and a Hall coefficient of $R_{\mathrm{H}} = 6.8 \times 10^{-3}$ m^{3}C^{-1}, the noise in the Hall voltage is $\sqrt{S_{\mathrm{V_H}}} = 1.6$ pVHz$^{-1/2}$. The Hall coefficient taken here is the same as was obtained in chapter 3 for an optimal As doped Si film.

This noise term should be compared with the intrinsic noise of the Hall sensor. The dominant noise source of Hall sensors is the Johnson noise [147] which is given by:

$$\sqrt{S_{\mathrm{V_J}}} = \sqrt{4k_{\mathrm{B}}TR_{\mathrm{V}}} \tag{5.4}$$

where T is the temperature, k_{B} the Boltzmann constant and R_{V} being the device resistance between the voltage contacts. This resistance depends on the magnetic field but here we take the zero field resistance value. The resistance between the current connections was calculated in chapter 3 to be 283 kΩ, which corresponds with the optimum doping density and the already mentioned Hall coefficient. Finite element simulations were performed on a Hall device with the already mentioned dimensions and resistance. When the voltage contacts have a width of 10 μm, the simulations show that the resistance between the voltage connections is $R_{\mathrm{V}} = 819$ kΩ. This value is larger than the resistance between the current contacts which is caused by the relatively narrow voltage contacts. This resistance value substituted in equation (5.4) gives a Johnson noise of $\sqrt{S_{\mathrm{V_J}}} = 59$ nVHz$^{-1/2}$ at $T = 77$ K.

This noise is over 4 orders of magnitude larger than the thermally induced vortex motion noise. Note however that the value for the flux noise is based on high quality films and is given at $f = 1$ Hz in a moderate field of 50 μT. In [143] it is shown that the flux noise can be a few orders of magnitude larger for films with lower critical current densities and critical temperatures. However for larger

cooling fields, lower frequency, sub optimal film qualities and a smaller maximum field range, the noise caused by vortex motion can be closer to the value of the Johnson noise but it is not likely that it will be larger.

5.3 Characterization of Bi Based Devices

Several devices with Bi Hall devices and YBCO flux concentrators have been produced with the production procedure described in section 4.1.1. The dimensions with respect to the concentrator and the sensor were in all cases the same however variations in the design incorporated slotted and solid washers. In figure 5.1 two SEM images show typical examples of a solid washer device in figure 5.1a) and slotted washer device in 5.1b). Due to the maximum scan range of the apparatus not the whole device is imaged. The square concentrator has a diameter of 8 mm. The slotted washer strips of figure 5.1b) have a width of 35 μm. In the bottom parts of the images the sensors are visible. On the left and on the right bottom part the bias current connection pads can be seen. In the hole of the concentrator and in the center bottom part of the image the voltage readout pads are visible.

5.3.1 Measurement Setup and Procedure

The samples were characterized in a helium flow cryostat. With this system the sample can be cooled down to a temperature of choice between room temperature and ~5 K. The insert of the system contains electrical filters to shield noise sources outside of the system. Moreover around the sensor a can is mounted of BSCCO, a high T_c superconductor which becomes superconducting at ~95 K, which provides a superconducting shield. Directly above the sample, inside the superconducting can, a small coil is mounted which provides the desired ambient magnetic field. The current for the field coil is provided by a low noise current source. The bias

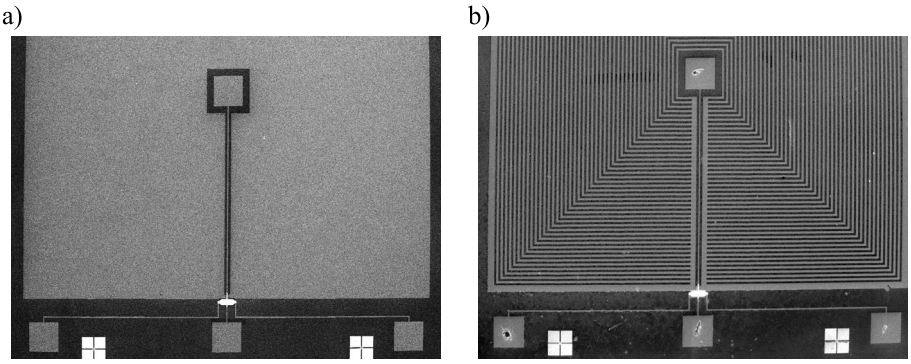

Figure 5.1: Scanning electron microscope (SEM) images of Bi Hall device based hybrid magnetometers with a) a solid washer and b) a slotted washer with 35 μm strips.

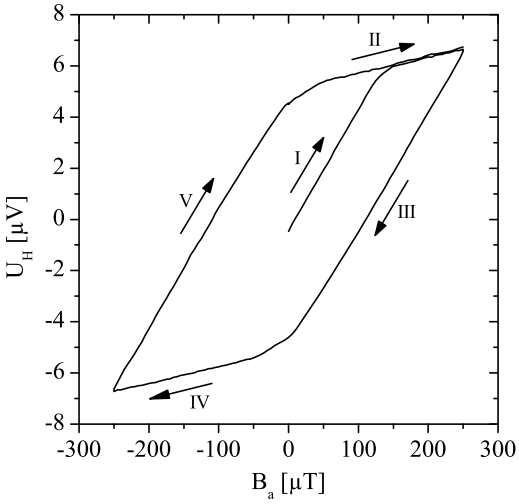

Figure 5.2: Example of a typical magnetic field sweep measurement. The field is swept to values beyond the maximum field and can provide most of the device characteristics. The order in which the measurement is carried out is indicated with I to V.

current of the sensor is also generated by a low noise current source and the voltage readout is done with a sensitive volt meter, capable of measuring voltages in the nanovolt range.

The characterization of the samples is carried out by means of magnetic field sweeps. Typical data of such a measurement is displayed in figure 5.2. In these kinds of measurements the sensor is operated to beyond its maximum field range, revealing the operation with and without the flux concentrator. This particular graph shows the measurement of a slotted washer concentrator device with a strip width of 6 μm. The temperature during the measurement is 80 K with a bias current through the Hall sensor of 5 mA. For clarity the offset voltage of $\approx$2.9 mV is removed.

In the graph two ranges of operation can be observed. The measurement starts in the middle of the hysteresis figure. When the magnetic field is increased, the sensor is in operation. That means that the flux concentrator is focusing the field on the sensor and the sensor itself is also sensing the field. This is indicated in the graph with I. By increasing the field the screening current in the concentrator is also increased up to a point where the critical current density of the constriction, which is the narrowest part in the concentrator, is reached. From this field value onwards every increase of the field will not result in a further increase of the screening current. This region is indicated with II in figure 5.2. Due to the fact that the concentrator is not a continuous loop of superconducting material anymore, flux quanta can enter the hole of the concentrator. When a flux quanta

is entering the hole, the screening current is lowered effectively to the point where it becomes superconducting again. So in fact in this region the screening current is constant at a value just below the critical current. At the end of the region indicated with II the field starts to decrease and the regime indicated with III is entered. At this point a number of flux quanta are in the hole of the ring and a decrease in field will result in a decrease in screening current while the number of flux quanta in the hole stays the same. This means that the concentrator is working however an offset is induced by the flux quanta that are trapped in the hole. Somewhere halfway this regime the screening current will become zero, and further on flow in the opposite direction. In between the regimes III and IV the critical current in this direction is reached and during operation in the regime indicated with IV will stay the same, comparable to II but with a screening current that flows in the opposite direction. In IV the flux quanta which were in the hole will leave the hole again and somewhere halfway will enter the hole again in the opposite direction. The field value is decreased again towards zero and in the regime indicated with V the concentrator is working again.

This type of measurement is interesting because it can provide almost all device characteristics. The slope of the regions indicated with II and IV give a measure for the Hall coefficient R_H. The quotient of the slopes in II and IV with III and V gives the concentrator gain. The field range of region III and V indicate the dynamic range of the device and the slope in these regions give the device sensitivity. It should however be noted that the device should preferably operated in the region indicated with I. In this region the device is in the Meissner regime and it is completely reversible. Although in regions III and V the concentrator is attributing to the sensitivity the device is not completely stable due effects like flux creep. The hysterisis measurements are merely a convenient way to retrieve the characteristic device properties.

5.3.2 Results

Both devices with solid washers and slotted washers were characterized. In this section the characterization of a slotted washer device with a strip width of 6 μm is discussed [148]. In general the behavior of the slotted and solid washer devices was comparable however the slotted washer devices showed some additional features which will also be highlighted in this section.

In figure 5.3 typical field sweep measurements are displayed. In figure 5.3a) field sweeps at 77 K are shown for 3 values of the bias current I_b whereas in figure 5.3b) the bias current was 7.5 mA and the temperature is varied. For clarity the offset voltage is in all cases subtracted.

Comparison of the offset voltage and the voltage change induced by a variation of the applied magnetic field shows that the offset voltage is very large, much larger than the Hall voltage. Typical Hall voltages are $\sim$10 μV while the offset voltage is $\sim$3 mV. An explanation for the large offset can be either a misalignment of the voltage contacts or an anisotropy in the resistance. Perfect alignment of the voltage contacts, that means perfectly opposite of each other, should result in an

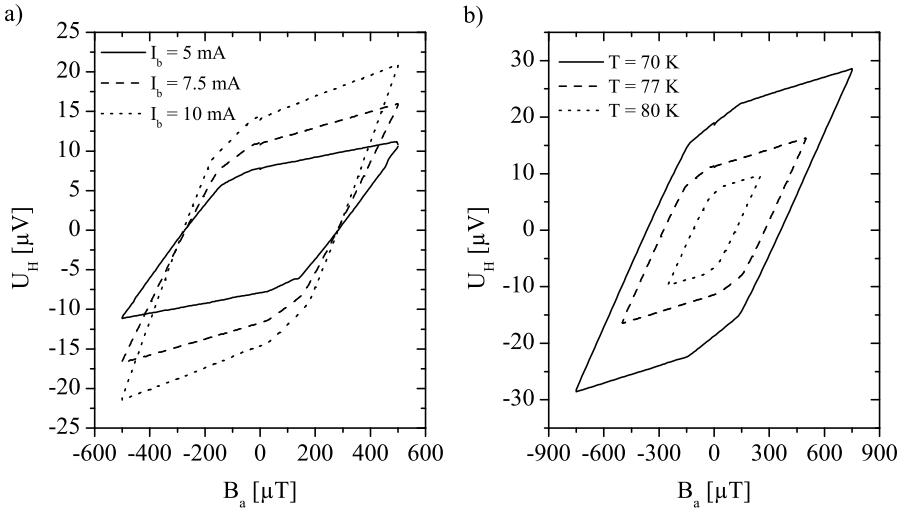

Figure 5.3: Hall voltage vs. applied field characteristics. a) At $T = 77$ K for bias currents of $I_\mathrm{b} = 5, 7.5$ mA. This graph shows an increase in the device sensitivity with and without the concentrator linear with the bias current. b) For $I_\mathrm{b} = 7.5$ mA at $T = 70$, 77 and 80 K. The effective field range is decreased by increasing the temperature.

absence of the offset voltage. The width of the contacts in these devices is 20 μm, which is a relatively easy to make width with a photo lithography process. The resistance of the device between the current connections is $R = 172.5\ \Omega$. Given a typical bias current of $I_\mathrm{b} = 7.5$ mA the voltage drop over the device is $V = 1.29$ V. With a device length of $l = 250$ μm the voltage drop per unit of length is 5.2 mVμm^{-1}. This means that the misalignment should be ~ 0.5 μm to obtain the voltage offset encountered in this device. Although the total width of the contacts is much larger than this value a misalignment of ~ 0.5 μm due to the photo lithography process is very plausible. Nevertheless a possible anisotropy in the resistance should not be excluded based on the findings presented in section 4.2.

Figure 5.3a) shows that the device sensitivity can be improved by increasing the bias current since it results in steeper voltage versus field characteristics. This effect is visible in both the region where the concentrator is effective and above the maximum field of operation. This can be explained by the fact that the sensor is operating in both regimes and the concentrator only below B_max.

As mentioned the temperature is varied between 70 and 80 K in figure 5.3b) while the bias current through the sensor is 7.5 mA. Obviously the maximum field is increasing with decreasing temperature. This can be attributed to an increase

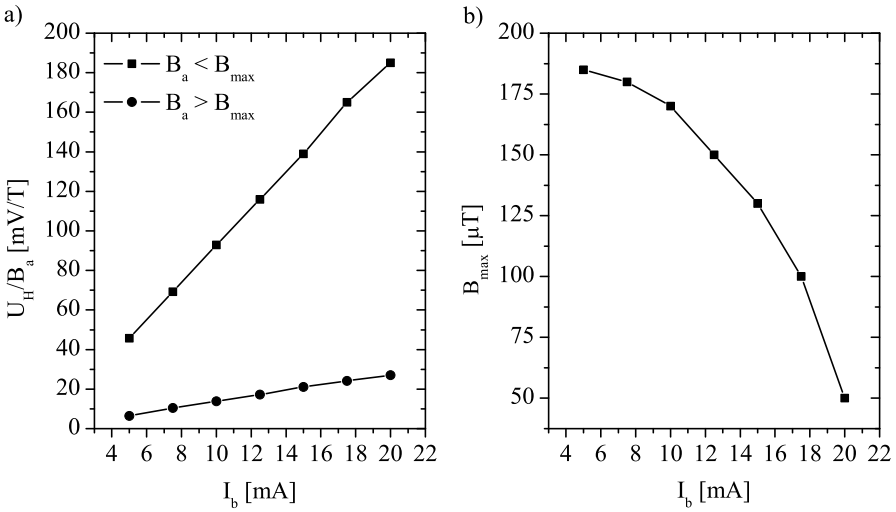

Figure 5.4: a) Device sensitivity vs. bias current with the concentrator ($B_\mathrm{a} < B_\mathrm{max}$) (squares) and without ($B_\mathrm{a} > B_\mathrm{max}$) (dots). In both cases the sensitivity increases linear with the bias current. b) maximum magnetic field vs. the bias current. Due to heating, by an increase of the bias current, the effective constriction width is decreased which also decreases the maximum magnetic field.

of the critical current density J_c. The maximum magnetic induction is increasing from ± 118 μT at 80 K to ± 310 μT at 70 K. At 77 K the maximum field is ± 170 μT. With equations (3.22), (3.23) and (3.24) one can calculate that the critical current density in the constriction equals $J_\mathrm{c} = 3.53 \times 10^6$ Acm^{-2} at 77 K. This is a normal value for the critical current density for YBCO films on STO substrates. The change in Hall coefficient between 70 and 80 K is small from $R_\mathrm{H} = 3.36 \times 10^{-7}$ m^{3}C^{-1} to $R_\mathrm{H} = 3.42 \times 10^{-7}$ m^{3}C^{-1}

In order to obtain a high sensitivity the bias current is varied. In principle the sensitivity should be linear dependent on the bias current. Figure 5.4a) shows that the sensitivity with and without the concentrator is indeed increasing linear. However by increasing the bias current the dissipation in the sensor is also increased. Since the constriction is positioned directly next to the sensor it is heated up due to the dissipation. Partly the constriction is not superconducting anymore and the effective width of the constriction is decreased. This effect should be observable in two ways. First of all the maximum magnetic field is decreased since the effective width of the constriction is decreased as shown in equation (3.24). In fact the decrease of B_max should be linear dependent on the effective width of the constriction. Figure 5.4b) clearly shows that indeed the maximum field is strongly decreased with increasing bias current. Secondly the heating causes the screening current to flow further away from the sensor which should result in a decrease in coupling, or in other words: gain. Figure 5.4a) shows that both the sensitivity

Table 5.1: Device properties of the device presented in this thesis and the device of [46].

Property	This Thesis	Work by Schmidt et al. [46]
R_{I^+,I^-} [Ω]	172.5	750
ρ [$\mu\Omega$cm]	$\approx$1540	1250
I_b [mA]	14.2	6.8
R_H [m^3C^{-1}]	3.4×10^{-7}	13×10^{-7}
P [mW]	35	35
Gain	6	20
U_H/B_a [VT^{-1}]	0.13	0.8
width constriction [μm]	70	20

of the sensor by itself and with the concentrator is at first sight increasing linear with the bias current. Closer inspection however shows that the gain is decreased by $\sim$10% in the plotted range. Compared to the decrease in maximum field this change is quite small. Suppose one assumes based on figure 5.4b) that at $I_b = 5$ mA no heating effects are observed and the maximum magnetic field is $B_{max} = 185\ \mu$T. At $I_b = 20$ mA the maximum magnetic field is only $B_{max} = 48\ \mu$T which means that the effective width decreased by a factor of 3.85. This means that the effective width of the concentrator is 18.7 μm and the gap between the sensor and the part where the supercurrent is flowing is 51.3 μm. The small decrease in coupling can be attributed to the fact that the coupling is already weak since it results in a gain of only 6.

As mentioned the device exhibits two regimes of operation, one where the concentrator is effective and one above the maximum magnetic field where only the sensor is effective. Closer inspection of figure 5.3 shows however, that there appears to be an intermediate regime. This regime shows a sensitivity larger than the sensitivity of the bare sensor but smaller than of the device with the active concentrator. This is believed to be is caused by the current distribution in the concentrator in combination with the strips. The current in a washer with a hole is not homogeneous. At the inside and on the outside the current density is higher [98]. Since the constriction is wider than the strips in the concentrator, 70 μm and 6 μm respectively, it is possible that the strips reach their critical current while the constriction is still superconducting. This is causing a change in the effective area and induction that results in a deterioration of the device sensitivity while the concentrator is in fact still working. This effect is not observed in this extend in the solid washer devices. The solid washer has in principle double the amount of material in the washer and so locally the screening current density is only half the value compared to the slotted washer version.

In table 5.1 the device properties are summarized combined with the experimental values of Schmidt et al. [46]. In this table R_{I^+,I^-} is the resistance between the current connections. Since the device presented here had only two current

connections it was not possible to perform a 4–point measurement. This means that the resistance here is an approximated value which most likely contains a small contact resistance part. In the paper of Schmidt et al. the dissipation in the device was 35 mW. Based on the device resistance a value for the bias current was obtained of $I_b = 14.2$ mA. The data presented in figure 5.4a) is interpolated to obtain a value for the device sensitivity.

Comparison of the device presented in this thesis with the device presented in [46] shows that the device presented here is less sensitive. This can for a part be attributed to the Hall coefficient. Although the specific resistance is more or less the same the Hall coefficient differs a factor of $\approx$4. Moreover the gain differs quite a lot. This is caused by the wider constriction which means that the device presented here has a larger dynamic range.

The device presented here shows sensitivities in the order of $\sim 10^{-1}$ V/T. That means that in order to obtain 10 pT resolution, which is required in space missions, one should measure voltages in the order of 10 fV. This is a challenging and nearly impossible task. Even though the coupling between concentrator and the Hall element can be improved this type of Hall element can not perform the task. As shown in chapter 3 doped Si Hall devices can have much better sensitivities. Doped Si sensors combined with an improvement in the coupling between the concentrator and the Hall sensor can result in the desired device sensitivity.

5.4 Characterization of Doped Si Based Devices

Devices based on the doped Si Hall device and YBCO flux concentrators have been fabricated with the production procedure described in section 4.1.2. In figure 5.5 two SEM images of the device are shown. The figure shows a device with solid washers where the ratio between the length and width of the hole is the same as outer dimensions of the concentrator comparable with the design shown in figure 3.7b). In figure 5.5a) a large part of the device is shown. On the left and right of this image the two concentrators are shown. These extend for a part outside the image and have a size of 4×8 mm^2. The voltage readout electrode extend on the left and right to the center of the concentrator holes. The current electrodes are situated in between the two concentrators and extend to the top and bottom to outside the image. In figure 5.5b) a magnification of the central part of the device is shown. In between the two voltage readout electrodes on the left and right the two constrictions are visible which have a width of 20 μm. The Hall sensor itself is not visible since it is basically the same material as the substrate.

As mentioned in section 4.1.2 the concentrator is structured by a photolithography process and wet etching in an H_3PO_4 solution. A 0.5 % solution was used for 15 s which structured the concentrators and completely removed the YBCO film at the position where the Hall sensor should be contacted by the electrodes. Electrical contact should be established by etching contact holes through the remaining YSZ/CeO_2 layer. The etch rate of YSZ is determined to be 19 nm/min. This is in reasonable correspondence with values found in [149]. In the same article

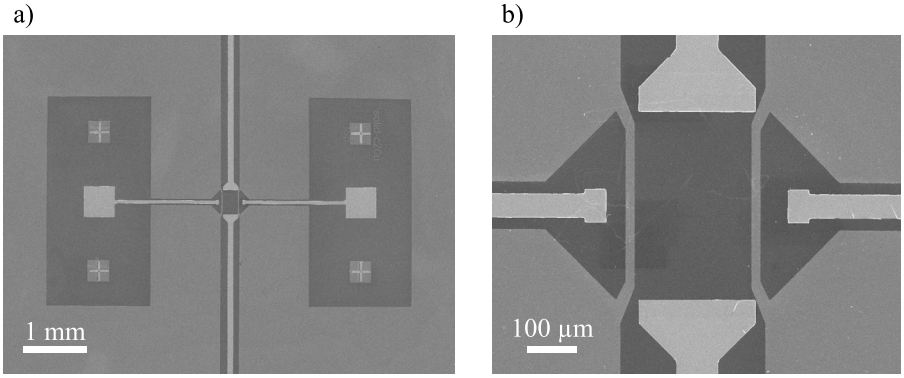

Figure 5.5: SEM images of the doped Si based hybrid magnetometer a) Overview of a large part of the device showing the two concentrators on the left and right. The sensor is positioned in the middle. b) Part of the device around the sensor area. On the left and right the voltage readout electrodes are visible and the bias current electrodes on the top and bottom.

the etch rates for CeO_2 and Si have been determined. The etch rate for the CeO_2 is the same as for YSZ, the etch rate for Si is over 40 % larger. The etch rate of the used system appeared to be rather irreproducible, for the YSZ and CeO_2 layers it varied up to a factor of 2.

The samples used in these experiments were doped with As in the same run as the samples used in the analyzes presented in section 4.3.2. In this doping run samples with and without masks where doped where the unstructured samples were used in the measurements of section 4.3.2 an the structured ones for the characterization presented here. Since the doping in this run was rather high as discussed in section 4.3.2 it should be relatively easy to establish a good electrical connection with the doped layer.

In a first device holes were etched based on the characterization of the etch rate. The holes should go through the YSZ/CeO_2 layer which uncovers the doped Si layer. Preferably the etching process should stop there and should not go through the Si layer completely. Resistivity measurements between the voltage and bias current connections showed unmeasurable high resistance values.

In a second sample the etching procedure was divided into a number of steps. After each step the resistivity was measured between the contact holes by means of a probe station. The measurements were carried out with soft needles which contained springs in order to prevent insurmountable damage to the contacts. Again resistivity was unmeasurable high in between all etching steps. Depth profiling with an alpha stepper showed that after a number of etching steps the contact holes reached to just below the Si layer which does not facilitate in a proper contact with the doped layer. However, the etching is performed under a 45° angle while the sample is constantly rotated which results in contact holes with sloped sides [150]. Therefore deposition of electrodes in the contact holes should in prin-

ciple make contact with the doped region. Electrodes of Ti covered with Au were deposited by sputtering. Measurements showed that the resistivity between the current contacts is ∼200 kΩ and no Hall effect was observed at room temperature.

At room temperature the specific resistance of the doped Si layer is based on the experimental findings presented in section 4.3.2 $\rho = 2.18 \times 10^{-4}$ Ωm. With equation (3.3) and the device dimensions $l = 400$ μm, $b = 250$ μm and $d = 50$ nm the Hall sensor resistance between the current contacts should be $R \approx 7$ kΩ which is much smaller then the measured value.

As mentioned the samples used in these experiments are doped in the same run as the results presented in section 4.3.2 and showed reproducible results. It is therefore unlikely that there can exist such differences in resistance values between the samples discussed here and the samples used in section 4.3.2. As mentioned the measurements in the probe station showed unmeasurable high resistances after every step of etching. Based on the findings in the etch rates characterization it is unlikely that a single step of etching went through the whole Si layer. The unmeasurable high resistance in between the etch steps can in principle be caused by the flexible needles which might not exercise enough force on the Si surface to obtain good contact. The needles were cleaned in an etching solution which makes it unlikely that the unmeasurable high values can be attributed to the probes. A second possibility is that the Si surface is damaged by the Ar ion bombardment. The etching process can drastically modify both structural and electrical properties of the Si near the surface due to amorphization [151, 152]. In principle recrystallization by annealing is possible. However the superconducting properties of the YBCO film are destroyed by raising the temperature to above ∼ 200 °C. Since the ion bombardment is performed under an angle of 45° the side walls of the contact hole can be damaged as well, which can explain the high resistance values.

The electrodes in this device, only make electrical contact on the sidewalls of the contact holes, which is most likely not resulting in the optimal electrical connection. Because the etch rate is showing strong deviations on the characterized value and is badly predictable combined with the fact that the etch rate for Si is significantly higher than for YSZ and CeO_2 it is at the moment rather challenging to reach the desired contact hole depth. This problem can be overcome by performing an element analyzes during etching, like for example SIMS. In this way the material which is etched away is known and one is able to determine the point when the Si layer emerges and the etching process is stopped. This however is not overcoming the possible amorphization of the surface. To prevent this an other technique to uncover the Si needs to be used. One can for example think of a wet etching technique, however no selective wet etchant for YSZ and CeO_2 was found. A second possibility would be to make the contact holes with a liftoff technique. Usually photo resist is used for this approach however this material is not suitable for depositions at high temperatures, like YBCO and the buffer layers. As an alternative to photoresist one can take a material which is deposited at room temperature, which is not reacting with Si and which can selectively be etched with for example a wet etching technique. A third possibility would be to make the con-

tacts to the Hall sensor before the concentrator is deposited. Since the electrodes do not touch the concentrator, the growth quality of the YSZ/CeO_2/YBCO layer on the electrodes is not important. Metals with a high melting temperature would be good canditate materials. Moreover the metal should be rather inert since it is exposed to oxygen at a high temperature during the pulsed laser deposition of the concentrator.

It was not possible to actually characterize these doped Si Hall device hybrid magnetometers because it was not possible, with the techniques used, to establish an electrical connection with the Hall sensor. More research on the material science aspects on connecting the Hall device without degrading the flux concentrator has to be conducted in order make this type of device operational. In theory however this type of devices has potential and solving the connection difficulties is not an unsurmountable task. As was shown in section 5.2 the intrinsic noise voltage is $\sqrt{S_{V_J}} = 59$ nVHz$^{-1/2}$ at $T = 77$ K. With a sensitivity of 23 VT^{-1}, which was theoretically determined in chapter 3, this yields a field resolution of $\sqrt{S_{\Phi_J}} = 2.6$ nTHz$^{-1/2}$. Note that this is the field resolution of just the sensor without a contribution of the concentrator. For a moderate maximum magnetic field the concentrators, the gain of these structures can easily be ∼25. This results in an overall field sensitivity of $\sqrt{S_{\Phi_{tot}}} \approx 100$ pTHz$^{-1/2}$. This means that, given that this device has a maximum magnetic field of ~ 5 μT, the dynamic range is $\sim 10^4$.

Given the dimensions and power consumption of the device these sensors are a promising alternative to other small vector magnetometers like micro flux gate sensors. The device resolution should also be compared with the typical resolution of sensors used in space. In chapter 1 is stated that vector magnetometers used in space have a typical field resolution of $\sim$ 5pTHz$^{-1/2}$. This field resolution can not be reached with a realistic constriction width and maximum magnetic field. In all the simulations presented in this thesis a distance of 100 nm between the sensor and the constriction is assumed. Certainly for the doped Si device with a doulble concentrator layout this is a rather pessimistic value since the constriction can in principle be directly next to, or even over the sensor. Decreasing this distance and a further reduction of the maximum magnetic field to 1 μT yields a field resolution that is one order of magnitude larger than the aimed value.

5.5 Summary

In this chapter the characterization of the hybrid magnetometer devices is discussed. This is preceded by a discussion on the expected $1/f$ noise characteristics of the device cooled down in a background magnetic induction. The results show that for high quality YBCO films on well matching substrates like STO for moderate magnetic inductions the $1/f$ noise contribution is much smaller than the intrinsic Johnson noise of the Hall sensor. Since the noise increases drastically for lower quality films, what can be expected for YBCO on SOI substrates, and for higher magnetic inductions this noise contribution can become important.

The characterization of the Bi device shows in general the expected values.

Due to the fact that the Hall coefficient is lower than the values that can be found in literature and the coupling between the concentrator and sensor is not very strong the device is not showing unrivaled sensitivity. A maximum sensitivity of ~ 180 mVT^{-1} is observed. Variations of the bias current show a strong influence on the maximum magnetic field. This can be attributed to heating which limits the maximum screening current through the constriction because a part of the constriction is not superconducting anymore. The devices are characterized by field sweeps beyond the maximum magnetic field resulting in two regimes of operation. The devices with slotted concentrators showed an intermediate regime of operation. This can most likely be attributed to the current distribution in the concentrator. A part of the strips on the outside of the washer reach their critical current at a lower field value than the constriction which alters the effective area and total inductance and therefore the field sensitivity. This can be attributed to the current distribution in the concentrator. A part of the strips on the outside of the washer reach their critical current at a lower field value than the constriction which alters the effective area and total inductance and therefore the field sensitivity.

The doped Si devices showed problems with contacting the Hall device. Contact is made by Ar ion etching holes through the buffer layers of YSZ/CeO_2 into the Si top layer. The resistance values measured are two orders of magnitude larger than expected and moreover no Hall effect could be observed. This can probably be attributed to amorphization of the top Si layer which is caused by the Ar ion etching process. To overcome this problem the contact holes should be constructed by a lift off photo lithography process.

Nevertheless these device have potential. The expected field accuracy can easily be ~ 100 pTHz$^{-1/2}$ with a dynamic range of $\sim 10^4$. Compared with for example miniaturized flux gate sensors this shows a large improvement.

References

[1] A. H. Morrish, *The physical properties of magnetism*, John Wiley & Sons, Inc, 1965.

[2] W. Gilbert, *De Magnete*, London, 1600.

[3] D. J. Stevenson, *Planetary magnetic fields*, Earth Planet. Sci. Lett. **208**, 1 (2003).

[4] C. T. Russell, *Outer planet magnetospheres: a tutorial*, Adv. Space Res. **33**, 2004 (2004).

[5] C. T. Russell, *The dynamics of planetary magnetospheres*, Planet. Space Sci. **49**, 1005 (2001).

[6] C. T. Russell, *Planetary magnetospheres*, Rep. Prog. Phys. **56**, 687 (1993).

[7] M. Purucker, D. Ravat, H. Frey, C. Voorhies, T. Sabaka, and M. H. Acuña, *An altitude-normalized magnetic map of Mars and its interpretation*, Geophys. Res. Lett. **27**, 2449 (2000).

[8] D. J. Stevenson, *Mars' core and magnetism*, Nature **412**, 214 (2001).

[9] M. H. Acuña, *Space-based magnetometers*, Rev. Sci. Instrum. **73**, 3717 (2002).

[10] N. A. Schwadron et al., *Comparison of Interstellar Boundary Explorer Observations with 3D Global Heliospheric Models*, Science **326**, 966 (2009).

[11] M. G. Kivelson, K. K. Khurana, J. D. Means, C. T. Russell, and R. C. Snare, *The Galileo magnetic field investigation*, Space Sci. Rev. **60**, 357 (1992).

[12] D. Huddleston, C. Russell, M. Kivelson, K. Khurana, and L. Bennett, *The location of the Jovian bow shock and magnetopause: Galileo initial results*, Adv. Space Res. **21**, 1463 (1998).

[13] M. K. Dougherty, S. Kellock, D. J. Southwood, A. Balogh, E. J. Smith, B. T. Tsurutani, B. Gerlach, K. H. Glassmeier, F. Gleim, C. T. Russell, G. Erdos, E. M. Neubauer, and S. W. H. Cowley, *The Cassini magnetic field investigation*, Space Sci. Rev. **114**, 331 (2004).

[14] H. Backes, F. M. Neubauer, M. K. Dougherty, N. Achilleos, N. Andre, C. S. Arridge, C. Bertucci, G. H. Jones, K. K. Khurana, C. T. Russell, and A. Wennmacher, *Titan's magnetic field signature during the first Cassini encounter*, Science **308**, 992 (2005).

[15] A. L. Albee, R. E. Arvidson, F. Palluconi, and T. Thorpe, *Overview of the Mars Global Surveyor mission*, Journ. Geophys. Res. Plan. **106**, 23291 (2001).

[16] A. Balogh, T. J. Beek, R. J. Forsyth, P. C. Hedgecock, R. J. Marquedant, E. J. Smith, D. J. Southwood, and B. T. Tsurutani, *The magnetic field investigation on the Ulysses mission - Instrumentation and preliminary scientific results*, Astron. Astrophys. Suppl. **92**, 221 (1992).

[17] D. A. Lohr, L. J. Zanetti, B. J. Anderson, T. A. Potemra, J. R. Hayes, R. E. Gold, R. M. Henshaw, F. F. Mobley, and D. B. Holland, *NEAR magnetic field investigation, instrumentation, spacecraft magnetics and data access*, Space Sci. Rev. **82**, 255 (1997).

[18] B. J. Anderson, M. H. Acuña, D. A. Lohr, J. Scheifele, A. Raval, H. Korth, and J. A. Slavin, *The magnetometer instrument on MESSENGER*, Space Sci. Rev. **131**, 417 (2007).

[19] O. V. Nielsen, J. R. Petersen, F. Primdahl, P. Brauer, B. Hernando, A. Fernandez, J. M. G. Merayo, and P. Ripka, *Development, construction and analysis of the Ørsted fluxgate magnetometer*, Meas. Sci. Technol. **6**, 1099 (1995).

[20] D. Duret, J. Bonzom, M. Brochier, M. Frances, J. M. Leger, R. Odru, C. Salvi, T. Thomas, and A. Perret, *Overhauser magnetometer for the Danish Ørsted satellite*, IEEE Trans. Magn. **31**, 3197 (1995).

[21] D. Duret, J. M. Leger, M. Frances, J. Bonzom, F. Alcouffe, A. Perret, J. C. Llorens, and C. Baby, *Performances of the OVH magnetometer for the Danish Ørsted satellite*, IEEE Trans. Magn. **32**, 4935 (1996).

[22] E. Friis-Christensen, H. Luehr, D. Knudsen, and R. Haagmans, *SWARM - An earth observation mission investigating geospace*, Adv. Space Res. **41**, 210 (2008).

[23] H. Aschenbrenner and G. Goubau, *Eine anordnung zur Registierung rascher magnetischer Störungen*, Hochfreqenztechn. Elektroak. **47**, 177 (1936).

[24] E. D. van Breukelen, A. R. Bonnema, W. J. Ubbels, and R. J. Hamann, *Delfi-C3 Delft university of technology's nanosatellite*, in *Proceedings of the 4S symphosium: small satellites, systems and services*, 2006.

[25] J. B. Kuo and S. C. Lin, *Low-voltage SOI CMOS VLSI devices and circuits*, John Wiley & Sons, Inc, 2001.

[26] P. D. D. Schwindt, S. Knappe, V. Shah, L. Hollberg, J. Kitching, L. A. Liew, and J. Moreland, *Chip-scale atomic magnetometer*, Appl. Phys. Lett. **85**, 6409 (2004).

[27] P. D. D. Schwindt, B. Lindseth, S. Knappe, V. Shah, J. Kitching, and L. A. Liew, *Chip-scale atomic magnetometer with improved sensitivity by use of the M-x technique*, Appl. Phys. Lett. **90**, 081102 (2007).

[28] C. W. Griffith, R. Jimenez-Martinez, V. Shah, S. Knappe, and J. Kitching, *Miniature atomic magnetometer integrated with flux concentrators*, Appl. Phys. Lett. **94**, 023502 (2009).

[29] I. K. Kominis, T. W. Kornack, J. C. Allred, and M. V. Romalis, *A subfemtotesla multichannel atomic magnetometer*, Nature **422**, 596 (2003).

[30] P. Ripka, S. Kawahito, S. O. Choi, A. Tipek, and M. Ishida, *Micro-fluxgate sensor with closed core*, Sens. Act. A **91**, 65 (2001).

[31] P. A. Robertson, *Microfabricated fluxgate sensors with low noise and wide bandwidth*, Electron. Lett. **36**, 331 (2000).

[32] P. Ripka, *Advances in fluxgate sensors*, Sens. Act. A **106**, 8 (2003).

[33] P. Ripka (ed.), *Magnetic sensors and magnetometers*, Artech House, 2001.

[34] D. Robbes, *Highly sensitive magnetometers – a review*, Sens. Act. **129**, 86 (2006).

[35] D. Robbes, C. Dolabdjian, S. Saez, Y. Monfort, G. Kaiser, and P. Ciureanu, *Highly sensitive uncooled magnetometers: State of the art. superconducting magnetic hybrid magnetometers, an alternative to SQUIDs?*, IEEE Trans. Appl. Supercond. **11**, 629 (2001).

[36] J. Mester et al., *Gravitational Experiments in Space: Gravity Probe B and STEP*, Nucl. Phys. B (Proc. Suppl.) **134**, 147 (2004), Proceedings of the Second International Conference on Particle and Fundamental Physics in Space (SpacePart '03).

[37] J. G. Bednorz and K. A. Muller, *Possible high T_c superconductivity in the Ba-La-Cu-O system*, Zeitschrift fur physik B **64**, 189 (1986).

[38] M. K. Wu, J. R. Ashburn, C. J. Torng, P. H. Hor, R. L. Meng, L. Gao, Z. J. Huang, Y. Q. Wang, and C. W. Chu, *Superconductivity at 93 K in a new mixed-phase Y-Ba-Cu-O compound system at ambient pressure*, Phys. Rev. Lett. **58**, 908 (1987).

[39] D. Koelle, R. Kleiner, F. Ludwig, E. Dantsker, and J. Clarke, *High-transition-temperature superconducting quantum interference devices*, Rev. Mod. Phys. **71**, 631 (1999).

[40] E. Hall, *On a New Action of the Magnet on Electric Currents*, Am. Journ. Mathemat. **2**, 287 (1879).

[41] P. Grünberg, R. Schreiber, Y. Pang, M. B. Brodsky, and H. Sowers, *Layered magnetic structures: evidence for antiferromagnetic coupling of Fe layers across Cr interlayers*, Phys. Rev. Lett. **57**, 2442 (1986).

[42] J. Daughton, J. Brown, E. Chen, R. Beech, A. Pohm, and W. Kude, *Magnetic-field sensors using GMR multilayer*, IEEE Trans. Magn. **30**, 4608 (1994).

[43] N. Smith, A. M. Zeltser, D. L. Yang, and P. V. Koeppe, *Very high sensitivity GMR spin-valve magnetometer*, IEEE Trans. Magn. **33**, 3385 (1997).

[44] Z. H. Qian, D. X. Wang, J. M. Daughton, M. Tondra, C. Nordman, and A. Popple, *Linear spin-valve bridge sensing devices*, IEEE Trans. Magn. **40**, 2643 (2004).

[45] M. Schneider, R. Castagnetti, M. G. Allen, and H. Baltes, *Integrated flux concentrator improves CMOS magnetotransistors*, in *MEMS '95, Proceedings. IEEE*, pages 151–, 1995.

[46] F. Schmidt, S. Linzen, F. Schmidl, M. Mans, and P. Seidel, *Development of a thin-film high-temperature superconductor Hall magnetometer*, Supercond. Sci. Technol. **15**, 488 (2002).

[47] S. Linzen, F. Schmidt, F. Schmidl, M. Mans, O. Hesse, F. Nitsche, G. Kaiser, S. Muller, and P. Seidel, *A thin film HTSC-Hall magnetometer - development and application*, Physica C **372**, 146 (2002).

[48] M. Pannetier, C. Fermon, G. Le Goff, and E. Kerr, *Ultra-sensitive mixed sensors - Design and performance*, Sens. Act. A **129**, 247 (2006).

[49] M. Pannetier, C. Fermon, G. Le Goff, J. Simola, and E. Kerr, *Femtotesla Magnetic Field Measurement with Magnetoresistive Sensors*, Science **304**, 1648 (2004).

[50] M. Pannetier, C. Fermon, G. Le Goff, J. Simola, E. Kerr, M. Welling, and R. J. Wijngaarden, *Ultra-sensitive field sensors - An alternative to SQUIDs*, IEEE Trans. Appl. Supercond. **15**, 892 (2005).

[51] A. Barone (ed.), *Principles and applications of superconducting quantum inteference devices*, World Scientific Publishing, 1992.

[52] P. P. P. M. Lerou, G. C. F. Venhorst, C. F. Berends, T. T. Veenstra, M. Blom, J. F. Burger, H. J. M. ter Brake, and H. Rogalla, *Fabrication of a micro cryogenic cold stage using MEMS-technology*, Journ. Micromech. Microeng. **16**, 1919 (2006).

[53] E. Dantsker, S. Tanaka, P. A. Nilsson, R. Kleiner, and J. Clarke, *Reduction of 1/f noise in high-T_c dc superconducting quantum interference devices cooled in an ambient magnetic field*, Appl. Phys. Lett. **69**, 4099 (1996).

[54] A. B. M. Jansman, M. Izquierdo, J. Flokstra, and H. Rogalla, *Slotted high-T_c dc SQUID magnetometers*, IEEE Trans. Appl. Supercond. **9**, 3290 (1999).

[55] J. R. Kirtley, M. B. Ketchen, C. C. Tsuei, J. Z. Sun, W. J. Gallagher, L. S. Yu-Jahnes, A. Gupta, K. G. Stawiasz, and S. J. Wind, *Design and Applications of a Scanning SQUID Microscope*, IBM Journal of Research and Development **39**, 655 (1995).

[56] W. Meissner and R. Ochsenfeld, *Ein neuer effekt bei eintritt der Supraleitfä higkeit*, Naturwissenschaften **21**, 787 (1933).

[57] C. P. Poole, H. A. Farach, and J. Creswick, *Superconductivity*, Academic Press, 1995.

[58] G. Blatter, M. V. Feigel'man, V. B. Geshkenbein, A. I. Larkin, and V. M. Vinokur, *Vortices in high-temperature superconductors*, Rev. Mod. Phys. **66**, 1125 (1994).

[59] A. Gurevich and G. Ciovati, *Dynamics of vortex penetration, jumpwise instabilities, and nonlinear surface resistance of type-II superconductors in strong rf fields*, Phys. Rev. B **77**, 104501 (2008).

[60] E. Dantsker, S. Tanaka, and J. Clarke, *High-T_c superconducting quantum interference devices with slots or holes: Low 1/f noise in ambient magnetic fields*, Appl. Phys. Lett. **70**, 2037 (1997).

[61] A. Chwala, R. IJsselsteijn, T. May, N. Oukhanski, T. Schuler, V. Schultze, R. Stolz, and H. G. Meyer, *Archaeometric prospection with high-T_c SQUID gradiometers*, IEEE Trans. Appl. Supercond. **13**, 767 (2003).

[62] S. Lee, W. Myers, H. Grossman, H.-M. Cho, Y. Chemla, and J. Clarke, *Magnetic gradiometer based on a high-transition temperature superconducting quantum interference device for improved sensitivity of a biosensor*, Appl. Phys. Lett. **81**, 3094 (2002).

[63] D. Doenitz, R. Straub, R. Kleiner, and D. Koelle, *Microscopic analysis of low-frequency flux noise in $YBa_2Cu_3O_{7-\delta}$ direct current superconducting quantum interference devices*, Appl. Phys. Lett. **85**, 5938 (2004).

[64] A. Crisan, A. Pross, D. Cole, S. J. Bending, R. Wördenweber, P. Lahl, and E. H. Brandt, *Anisotropic vortex channeling in $YBa2Cu3O7--\delta$ thin films with ordered antidot arrays*, Phys. Rev. B **71**, 144504 (2005).

[65] D. Koelle, R. Gross, R. Straub, S. Keil, M. Fischer, M. Peschka, R. P. Huebener, and K. Barthel, *Vortex imaging by low-temperature scanning electron microscopy and correlation with low-frequency noise in YBCO DC SQUIDs*, Physica C **332**, 148 (2000).

[66] J. R. Clem, *Vortex Exclusion from Superconducting Strips and SQUIDs in Weak Perpendicular Ambient Magnetic Fields*, Bull. Am. Phys. Soc. **43**, 401 (1998), Paper K36.06, and unpublished work.

[67] K. K. Likharev, *The formation of a mixed state in planar superconducting films*, Sov. Radiophys **14**, 919 (1971).

[68] G. Stan, S. B. Field, and J. M. Martinis, *Critical Field for Complete Vortex Expulsion from Narrow Superconducting Strips*, Phys. Rev. Lett. **92**, 097003 (2004).

[69] E. Bronson, M. P. Gelfand, and S. B. Field, *Equilibrium configurations of Pearl vortices in narrow strips*, Phys. Rev. B **73**, 144501 (2006).

[70] M. Tinkham, *Effect of Fluxoid Quantization on Transitions of Superconducting Films*, Phys. Rev **129**, 2413 (1963).

[71] V. G. Kogan, *Pearls vortex near the film edge*, Phys. Rev. B **49**, 15874 (1994).

[72] G. M. Maksimova, *Mixed state and critical current in narrow semiconducting films*, Phys. Solid State **40**, 1607 (1998).

[73] M. Tinkham, *Introduction to Superconductivity, 2nd Edition*, McGraw-Hill, New York, 1996.

[74] K. H. Kuit, J. R. Kirtley, W. van der Veur, C. G. Molenaar, F. J. G. Roesthuis, A. G. P. Troeman, J. R. Clem, H. Hilgenkamp, H. Rogalla, and J. Flokstra, *Vortex trapping and expulsion in thin-film $YBa_2Cu_3O_{7-\delta}$ strips*, Phys. Rev. B **77**, 134504 (2008).

[75] A. A. B. Brojeny, Y. Mawatari, M. Benkraouda, and J. R. Clem, *Magnetic fields and currents for two current-carrying parallel coplanar superconducting strips in a perpendicular magnetic field*, Supercond. Sci. Technol. **15**, 1454 (2002).

[76] M. Benkraouda and J. R. Clem, *Magnetic hysteresis from the geometrical barrier in type-II superconducting strips*, Phys. Rev. B **53**, 5716 (1996).

[77] M. Benkraouda and J. R. Clem, *Critical current from surface barriers in type-II superconducting strips*, Phys. Rev. B **58**, 15103 (1998).

[78] V. G. Kogan, *Interaction of vortices in thin superconducting films and the Berezinskii-Kosterlitz-Thouless transition*, Phys. Rev. B **75**, 64514 (2007).

[79] A. G. P. Troeman, *NanoSQUID magnetometers and high resolution scanning SQUID microscopy*, PhD thesis, University of Twente, 2007.

[80] www.hypres.com.

[81] S. M. Maurer, N. C. Yeh, and T. A. Tombrello, *Vortex pinning by cylindrical defects in type-II superconductors: Numerical solutions to the Ginzburg-Landau equations*, Phys. Rev. B **54**, 15372 (1996).

[82] J. Y. Lee and T. R. Lemberger, *Penetration depth $\lambda(T)$ of $YBa_2Cu_3O_{7-\delta}$ films determined from the kinetic inductance*, Appl. Phys. Lett. **62**, 2419 (1993).

[83] E. Il'ichev, L. Dörrer, F. Schmidl, V. Zakosarenko, P. Seidel, and G. Hildebrandt, *Current resolution, noise, and inductance measurements on high-T_c dc SQUID galvanometers*, Appl. Phys. Lett. **68**, 708 (1996).

[84] K. H. Kuit, J. R. Kirtley, J. R. Clem, H. Rogalla, and J. Flokstra, *Vortex Trapping and Expulsion in Thin-Film Type-II Superconducting Strips*, IEEE Trans. Appl. Supercond. **19**, 3537 (2009).

[85] H. Weinstock, *SQUID Sensors: Fundamentals, Fabrication and Applications*, Kluwer Academic, 1996.

[86] H. J. Barthelmess, M. Halverscheid, B. Schiefenhovel, E. Heim, M. Schilling, and R. Zimmermann, *Low-noise biomagnetic measurements with a multichannel dc-SQUID system at 77 K*, IEEE Trans. on Appl. Supercond. **11**, 657 (2001).

[87] M. Pannetier-Lecoeur, C. Fermon, N. Biziere, J. Scola, and A. L. Walliang, *RF Response of Superconducting-GMR Mixed Sensors, Application to NQR*, IEEE Trans. Appl. Supercond. **17**, 598 (2007).

[88] H. Ibach and H. Luth, *Solid-State Physics: An Introduction to Principles of Materials Science*, Springer, 2^{nd} edition, 1995.

[89] S. Sze, *Semiconductor Devices: Physics and Technology*, John Wiley & Sons, Inc, 2^{nd} edition, 2002.

[90] T. T. Mnatsakanov, M. E. Levinshtein, L. I. Pomortseva, and S. N. Yurkov, *Universal analytical approximation of the carrier mobility in semiconductors for a wide range of temperatures and doping densities*, Semicond. **38**, 56 (2004).

[91] H. P. Baltes and R. S. Popovic, *Integrated semiconductor magnetic-field sensors*, Proc. IEEE **74**, 1107 (1986).

[92] J. Haesler and H. J. Lippmann, *Hall Generators with small linearity error*, Sol. State Electron. **11**, 173 (1968).

[93] F. Kuhrt and H. J. Lippmann, *Hallgeneratoren*, Springer-Verlag, 1986.

[94] F. Grover, *Inductance calculations, working formulas and tables*, Dover, 1962.

[95] D. Drung, *Sensor und A/D-Wandlerstufe auf einem Chip zur Präzissionmessung von Magnetfeldgradienten mit Josephson-Kontakten*, PhD thesis, Universität Fridericiana Karlsruhe, 1988.

[96] J. M. Jaycox and M. B. Ketchen, *Planar coupling scheme for ultra low noise DC SQUIDs*, IEEE Trans. Magn. **17**, 400 (1981).

[97] M. B. Ketchen, W. J. Gallagher, A. H. Kleinsasser, S. Murphy, and J. R. Clem, *SQUID '85*, Springer-Verlag, 1985.

[98] A. B. M. Jansman, *High-T_c dc-SQUIDs for use in a background field*, PhD thesis, University of Twente, 1999.

[99] G. K. Celler and S. Cristoloveanu, *Frontiers of silicon-on-insulator*, Journ. Appl. Phys. **93**, 4955 (2003).

[100] K. H. Kuit, W. van de Camp, S. Waanders, H. Rogalla, and J. Flokstra, *Hybrid magnetometers based on a doped silicon-on-insulator Hall device and a $YBa_2Cu_3O_{7-\delta}$ flux concentrator*, Supercond. Sci. Technol. **22**, 114006 (2009).

[101] H. Toepfer, T. Ortlepp, and H. F. Uhlmann, *Statistical modeling of inductances in high-T_c superconductor electronic structures*, Phys. C **350**, 201 (2001).

[102] http://www.comsol.com.

[103] http://www.sonnetsoftware.com.

[104] A. R. Kerr, *Surface Impedance of Superconductors and Normal Conductors in EM Simulators*, MMA Memo **No. 245** (1999).

[105] L. Kang, Z. F. Di, S. Z. Yang, Y. J. Feng, and P. H. Wu, *Epitaxial growth of $YBa_2Cu_3O_7/CeO_2/YSZ$ thin films on silicon-on-insulator substrates*, Supercond. Sci. Technol. **15**, 320 (2002).

[106] M. Ohring, *The Materials Science of Thin Films*, Academic Press, 1992.

[107] M. O. Boffou, B. Lenoir, H. Scherrer, and A. Dauscher, *Pulsed laser deposition of bismuth in the presence of different ambient atmospheres*, Thin Solid Films **322**, 132 (1998).

[108] M. O. Boffoue, B. Lenoir, A. Jacquot, H. Scherrer, A. Dauscher, and M. Stolzer, *Structure and transport properties of polycrystalline Bi films*, Journ. Phys. Chem. Sol. **61**, 1979 (2000).

[109] J. C. G. de Sande, T. Missana, and C. N. Afonso, *Optical properties of pulsed laser deposited bismuth films*, Journ. Appl. Phys. **80**, 7023 (1996).

[110] D. H. Kim, S. H. Lee, J. K. Kim, and G. H. Lee, *Structure and electrical transport properties of bismuth thin films prepared by RF magnetron sputtering*, Appl. Surf. Sci. **252**, 3525 (2006).

[111] F. Y. Yang, K. Liu, C. L. Chien, and P. C. Searson, *Large Magnetoresistance and Finite-Size Effects in Electrodeposited Single-Crystal Bi Thin Films*, Phys. Rev. Lett. **82**, 3328 (1999).

[112] S. Cho, Y. Kim, A. J. Freeman, G. K. L. Wong, J. B. Ketterson, L. J. Olafsen, I. Vurgaftman, J. R. Meyer, and C. A. Hoffman, *Large magnetoresistance in postannealed Bi thin films*, Appl. Phys. Lett. **79**, 3651 (2001).

[113] D. L. Partin, J. Heremans, D. T. Morelli, C. M. Thrush, C. H. Olk, and T. A. Perry, *Growth and characterization of epitaxial bismuth films*, Phys. Rev. B **38**, 3818 (1988).

[114] L. J. v. d. Pauw, *A method of measuring specific resistivity and Hall effect of disks of arbitrary shape*, Philips Res. Rep. **13**, 1 (1958).

[115] http://www.qdusa.com/products/ppms.html.

[116] S. A. Campbell, *The Science and Engineering of Microelectronic Fabrication (2^{nd} edition)*, Oxford, 2001.

[117] J. P. Normand, *Silicon-on-Insulator technology: Material to VLSI*, Kluwer Academic, 1997.

[118] H. Norstrom, T. Johansson, J. Vanhellemont, and K. Maex, *A study of high-dose As and BF_2 implantations into SIMOX materials*, Semicond. Sci. Technol. **8**, 630 (1993).

[119] A. Suzuki, H. Nakamura, T. Izumi, T. Onda, and T. Hara, *Annealing behavior of defects introduced in SOI structure by arsenic ion implantation (ESR and PAS studies)*, Mat. Chem. Phys. **54**, 67 (1998).

[120] A. Ogura and M. Hiroi, *Depth profiles of As and B implanted into Si-on-insulator substrates*, Thin Solid Films **397**, 56 (2001).

[121] R. M. de Oliveira, M. Dalponte, and H. Boudinov, *Electrical activation of arsenic implanted in silicon on insulator (SOI)*, Journ. Phys. D **40**, 5227 (2007).

[122] L. Ottaviano, M. Italia, G. Mannino, V. Privitera, M. Herden, and T. Feudel, *Electrical activation of B and As implants in Silicon On Insulator (SOI) wafers*, Mat. Sci. Eng. B **114**, 260 (2004).

[123] A. F. Saavedra, K. S. Jones, M. E. Law, K. K. Chan, and E. C. Jones, *Electrical activation in silicon-on-insulator after low energy boron implantation*, Journ. Appl. Phys. **96**, 1891 (2004).

[124] E. Ishida and S. B. Felch, *Study of electrical measurement techniques for ultra-shallow dopant profiling*, Journ. Vac. Sci. Technol. B **14**, 397 (1996).

[125] C. Y. Wong, C. R. M. Grovenor, P. E. Batson, and R. D. Isaac, *Arsenic segregation to silicon silicon-oxide interfaces*, Journ. Apll. Phys. **58**, 1259 (1985).

[126] Y. Sato, J. Nakata, K. Imai, and E. Arai, *Arsenic Pileup at the SiO_2/Si Interface*, Journ. Electrochem. Soc. **142**, 655 (1995).

[127] F. J. Morin and J. Maita, *Electrical Properties of Silicon Containing Arsenic and Boron*, Phys. Rev. **96**, 28 (1954).

[128] R. Carlson, *Electrical Properties of Near-Degenerate Boron-Doped Silicon*, Phys. Rev. **100**, 1075 (1955).

[129] http://www.silvaco.com/products/process_ simulation/athena.html.

[130] http://www.highvolteng.com.

[131] S. Linzen, J. Krausslich, A. Kohler, P. Seidel, B. Freitag, and W. Mader, *Unusual crystal structure of non-superconducting $YBa_2Cu_3O_{7-x}$ films on buffered silicon substrates*, Phys. C **290**, 323 (1997).

[132] Y. J. Tian, S. Linzen, F. Schmidl, A. Matthes, H. Schneidewind, and P. Seidel, *On ageing and critical thickness of $YBa_2Cu_3O_7$ films on Si with CeO_2/YSZ buffer layers*, Thin Solid Films **338**, 224 (1999).

[133] P. Wang, J. Li, W. Peng, K. Chen, P. L. Lang, J. Y. Xiang, Y. F. Chen, X. P. Xu, H. Y. Tian, and D. N. Zheng, *Epitaxial growth of $YBa_2Cu_3O_{7-\delta}$ thin films on silicon-on-insulator substrates by pulsed laser deposition*, Supercond. Sci. Technol. **17**, 804 (2004).

[134] J. Kawashima, Y. Yamada, and I. Hirabayashi, *Critical thickness and effective thermal expansion coefficient of YBCO crystalline film*, Phys. C **306**, 114 (1998).

[135] Y. Okada and Y. Tokumaru, *Precise determination of lattice parameter and thermal expansion coefficient of silicon between 300 and 1500 K*, Journ. Appl. Phys. **56**, 314 (1984).

[136] A. N. Khodan, J. P. Contour, D. Michel, O. Durand, R. Lyonnet, and M. Mihet, *ZrO_2-CeO_2 and CeO_2-La_2O_3 film growth on oxide substrates and their applications in oxide heterostructures*, Journ. Crys. Gr. **209**, 828 (2000).

[137] P. Wang, J. Li, W. Peng, Y. F. Chen, and D. N. Zheng, *Investigation of the strain relaxation and ageing effect of $YBa_2Cu_3O_{7-\delta}$ thin films grown on silicon-on-insulator substrates with yttria-stabilized zirconia buffer layers*, Supercond. Sci. Technol. **19**, 51 (2006).

[138] S. J. Wang, C. K. Ong, L. P. You, and S. Y. Xu, *Epitaxial growth of yittria-stabilized zirconia oxide thin film on natively oxidized silicon wafer without an amorphous layer*, Semicond. Sci. Technol. **15**, 836 (2000).

[139] S. J. Wang and C. K. Ong, *Epitaxial Y-stabilized ZrO_2 films on silicon: Dynamic growth process and interface structure*, Appl. Phys. Lett. **80**, 2541 (2002).

[140] M. D. Nguyen, R. J. A. Steenwelle, P. M. te Riele, J. M. Dekkers, D. H. A. Blank, and G. Rijnders, *Growth and properties of functional oxide thin films for PiezoMEMS*, in *Proc. EUROSENSORS XXII*, 2008.

[141] M. J. Ferrari, M. Johnson, F. C. Wellstood, J. Clarke, P. A. Rosenthal, R. H. Hammond, and M. R. Beasley, *Magnetic flux noise in thin-film rings of $YBa_2Cu_3O_{7-\delta}$*, Appl. Phys. Lett. **53**, 695 (1988).

[142] M. J. Ferrari, M. Johnson, F. C. Wellstood, J. Clarke, D. Mitzi, P. A. Rosenthal, C. B. Eom, T. H. Geballe, A. Kapitulnik, and M. R. Beasley, *Distribution of flux-pinning energies in $YBa_2Cu_3O_{7-\delta}$ and $Bi_2Sr_2CaCu_2O_{8+\delta}$ from flux noise*, Phys. Rev. Lett. **64**, 72 (1990).

[143] M. J. Ferrari, M. Johnson, F. C. Wellstood, J. J. Kingston, T. J. Shaw, and J. Clarke, *Magnetic flux noise in copper oxide superconductors*, Journ. Low Temp. Phys. **94**, 15 (1994).

[144] M. J. Ferrari, J. J. Kingston, F. C. Wellstood, and J. Clarke, *Flux noise from superconducting $YBa_2Cu_3O_{7-\delta}$ flux transformers*, Appl. Phys. Lett. **58**, 1106 (1991).

[145] H.-M. Cho, R. McDermott, B. Oh, K. Kouznetsov, A. Kittel, J. Miller, J.H., and J. Clarke, *Low-frequency noise in field-cooled, directly coupled magnetometers*, IEEE Trans. Appl. Supercond. **9**, 3294 (1999).

[146] F. P. Milliken, S. L. Brown, and R. H. Koch, *Magnetic field-induced noise in directly coupled high T_c superconducting quantum interference device magnetometers*, Appl. Phys. Lett. **71**, 1857 (1997).

[147] G. Boero, M. Demierre, P. A. Besse, and R. S. Popovic, *Micro-Hall devices: performance, technologies and applications*, Sens. Act. A **106**, 314 (2003).

[148] K. H. Kuit, J. R. Kirtley, H. Rogalla, and J. Flokstra, *Vortex Trapping in Hybrid Magnetometers*, Sens. Lett. **7**, 289 (2009).

[149] J. H. Kim and A. M. Grishin, *Wet and dry etching of* $La_{0.67}(Sr,Ca)_{0.33}MnO_3$ *films on Si*, Thin Solid Films **515**, 587 (2006).

[150] M. J. Madou, *Fundamentals of microfabrication: the science of miniaturization*, CRC Press, 2002.

[151] R. S. Williams, *Low-energy Ar ion-bombardment damage of Si, GaAs and InP surfaces*, Sol. State Commun. **41**, 153 (1982).

[152] L. J. Huang, W. M. Lau, H. T. Tang, W. N. Lennard, I. V. Mitchell, P. J. Schultz, and M. Kasrai, *Near-surface structure of low-energy-argon-bombarded Si(100)*, Phys. Rev. B **50**, 18453 (1994).

Summary

Magnetic field mapping of planets and the galaxy has been subject of research for numerous years, starting in the 1950s. Space missions carrying magnetometers are used for planetary research to give insight not only in the remanent magnetic field on the surface of the planet but also in the dynamics of the core deep down. Furthermore there is interest in the magnetic field of the solar system as a whole where the global interaction between the solar wind and the interstellar medium is investigated.

Magnetic field sensor configurations on board spacecrafts consist, in most cases, of a vector and a scalar sensor. The absolute accuracy of the vector magnetometer is in general insufficient and a calibration with an absolute scalar magnetometer is required. As a vector magnetometer usually a fluxgate sensor is used and optically pumped and free precession magnetometers are often used to measure the scalar field. Since spacecrafts nowadays are becoming smaller, strong demands on the size, weight and power consumption have to be imposed on the used magnetometers. Small scalar optically pumped magnetometers based on micro vapor cells possess the required sensitivity and also meet the other demands. Small vector magnetometers like micro fluxgates do not possess the required sensitivity.

Other vector magnetometers like Hall sensors or giant magneto resistances (GMR) are small, light weight and have a low power consumption but do not possess the desired sensitivity. The sensitivity can be enhanced by applying magnetic flux concentration by means of a high-T_c flux concentrator. These hybrid devices have been developed with both bismuth (Bi) Hall sensors and GMR's and are showing promising sensitivities. The integration of semiconductors and superconductors, like a doped silicon (Si) Hall device and a high-T_c flux concentrator,

is believed to result in a further improvement of the sensitivity what makes it suitable for space applications.

Magnetic field sensors constructed from superconducting films, like for example SQUIDs and hybrid magnetometers, which are used in unshielded environments can exhibit high $1/f$ noise characteristics. This noise is caused by the thermally activated movement of trapped flux vortices in the superconducting body. By dividing the body into narrow strips this noise can be suppressed since the strips have a critical magnetic field below which no vortex trapping occurs.

Theoretical models for this critical field of thin film superconducting strips from literature did not show good correspondence with available experimental data. A new improved model for the critical field is derived which includes the pairing energy of a vortex anti-vortex pair. Whether or not a vortex gets trapped in a strip is determined by the Gibbs free energy. This energy exhibits a dip in the center of a superconducting strip for applied inductions above a certain critical value. In the theoretical model presented in this thesis the depth of the resulting potential well is assumed to equal the amount of energy required to create a vortex anti-vortex pair. Since this energy and the Gibbs free energy have the same temperature dependency, material properties like the Pearl length and the coherence length cancel out. The resulting expression shows only a strip width dependency. Due to a slight modification on the expression of the Gibbs free energy, as it is presented in literature, it was also possible to directly derive an expression for the vortex density above the critical field.

Direct experimental verification with a scanning SQUID microscope (SSM) on $YBa_2Cu_3O_{7-\delta}$ (YBCO) and niobium (Nb) strips showed excellent agreement between critical field model values and measurements. No differences between the critical fields in Nb and YBCO were found. It can therefore be concluded that no material dependency exists in the critical field. Measurements on the vortex density above the critical field showed reasonable agreement with the model. Besides the density also the distribution of the vortices has statistically been analyzed. From a sensor point of view this is not directly relevant since vortices are unwanted but the analyzes give insight in defects in the material. The vortices are trapped in the center of the strips for relatively low inductions and in two parallel rows for higher inductions. The field where the transition from a single row to two parallel rows of vortices occurred corresponds with values obtained from literature. Moreover the trapping in Nb showed a more homogeneous distribution in the longitudinal direction of the strip and a smaller spread around the center in the lateral direction. This is evidence that the YBCO strips contain much more and more severe defects compared to Nb.

The results of the research on vortex trapping in thin film superconducting strips has been applied in concentrators of hybrid magnetometers. A theoretical model for the optimization of the sensor, the concentrator and the combination of both is derived. As a sensor a doped Si Hall device is considered. Compared to previous work with Bi Hall devices, doped Si can have much higher Hall coefficients. Parameters such as the carrier density and mobility vs. the temperature have been investigated. Several dopants are compared and an optimal doping density

is obtained where attention is paid to the resulting device sensitivity and resistivity. A double concentrator layout is considered which gives a better coupling to the sensor compared to a single concentrator. In the case of two concentrators the screening current in one of these concentrators is lower than for a single large concentrator since the amount of flux that is collected is smaller. Therefore the width of the constriction can be decreased. This is beneficial because a narrower constriction provides better coupling to the sensor. The total area of the device is kept the same which is on a square substrate of 1 cm^2. This means that in the case of the double concentrator layout the concentrators should be rectangular. From literature no analytical expressions for the inductance and effective area for a rectangular layout could be obtained and therefore finite element simulations are used to determine these properties. To test the simulations it was also applied on square washers for which analytical expression do exist and good correspondence between model and simulation was obtained.

The fabrication process of hybrid magnetometers in general comprehends well developed techniques. Some of the challenging production steps are highlighted. For the Bi hybrid magnetometer RF sputtering of Bi is investigated. The resulting films were rather rough which in principle is not a problem as long as a closed current path can be realized. An optimization study to obtain the optimum deposition conditions has been performed where the substrate temperature, sputtering power and process pressure were widely varied. Visual inspection by scanning electron microscopy (SEM) imaging showed that between 373 K and 388 K a clear difference in growth could be observed. Electrical investigations showed that the best films, that means with the highest Hall coefficient, could be obtained at 388 K. The obtained values correspond reasonably well with values found in literature where other deposition techniques were used.

Doping implantation in Si and YBCO growth on Si were investigated for application in the doped Si Hall device hybrid magnetometer. The doped Si devices are constructed on silicon on insulator (SOI) substrates. This has the advantage that a well defined homogeneous doped region can be created with respect to the Si doping. Secondly, the thermal stress due to rather large differences in the thermal expansion coefficients between Si and YBCO can be relaxed in the SiO_2 inter layer.

By means of simulations the optimum dose and acceleration voltage for implantation were determined. In order to be in the ion implanter's range of acceleration energies a SiO_2 film was sputtered on the SOI substrate before it was implanted. Samples were doped with arsenic (As) and boron (B). The sputtered SiO_2 layer appeared to be more transparent than expected based on the simulations. The As doping was much too high and the B doping much too low, even that low that electrical characterization was not possible. Nevertheless the Hall coefficient obtained from the As doped samples with sub optimal implantation parameters showed already and improvement of a factor of 2–4 with the Bi Hall sensor based devices.

YBCO films on SOI wafers were grown with pulsed laser deposition. Yttrium stabilized Zirconia (YSZ) and CeO_2 were used as buffer layers to provide the

correct growth orientation and lattice match and to prevent diffusion of oxygen. It was possible to deposit high quality film which showed critical temperatures and current densities that were comparable to values obtained from literature. Since the SOI substrates used had a very thin top Si layer of 50 nm buckling of the Si layer was observed. By limiting the thickness of the buffer layers it was possible to prevent this.

As mentioned the sensitivity of Hall devices can be enhanced by flux concentration. However due to vortex movement induced noise in the flux concentrator the device resolution can be limited. This noise is derived and compared with the intrinsic noise of the Hall sensor. $1/f$ noise in YBCO films has experimentally been determined in several papers. Substitution of the spectral noise contribution term from literature in the model showed that when high quality films, deposited on well matching substrates are used, vortex induced noise should not be dominant. The noise of YBCO films deposited on SOI substrate was never experimentally determined. Although it is likely that the noise will be higher than for films deposited on well matching substrates it is not likely that noise in these films will dominate the noise in the device.

Bi Hall device hybrid magnetometers have been characterized. Several hybrid magnetometers were produced with and without slotted washers. Besides the characteristic values the measurements on the slotted washer devices showed additional features which can be attributed to the strips in the concentrator. Compared with previous work on Bi Hall device hybrid magnetometer the characteristic values obtained here do not reach those found in literature. This can be attributed to a lower Hall coefficient and for the biggest part to a weak coupling between Hall sensor and concentrator. The device presented in this thesis has a much higher maximum magnetic field and has a wider constriction which causes weaker coupling.

The characterization of the doped Si based devices is impeded by difficulties in the connection between the Hall sensor and the electrodes. The Hall sensor has to be connected via contact holes made with Ar ion milling. The milling is probably damaging the Si which becomes amorphous for a small part on the surface. This results in very high contact resistances which impedes the operation. To prevent this another way of contacting the device has to be found. It might also be possible to connect the doped region before the concentrator is deposited.

Samenvatting

(Summary in Dutch)

Vanaf de jaren 50 is het meten van het magnetisch veld van planeten en de melkweg het onderwerp van onderzoek geweest. Ruimtevaartmissies die sensoren voor het magnetische veld aan boord hebben, worden gebruikt bij planetair onderzoek om inzicht te geven in het remanente magnetisch veld aan het oppervlak van de planeet maar ook naar de dynamica van de kern diep in de planeet. Verder is er interesse in het magnetisch veld van het zonnestelsel als geheel, waar de interactie tussen de zonnewind en het interstellaire medium wordt onderzocht.

De configuratie van sensoren voor het magnetische veld in ruimtevaartuigen bestaat in veel gevallen uit een vector- en een scalaire sensor. Over het algemeen is de absolute veldgevoeligheid van een vectormagnetometer niet toereikend en is een calibratie met een absolute scalairmagnetometer vereist. Als vectormagnetometer wordt doorgaans een "fluxgate" sensor gebruikt. Een optisch gepompte of een vrije precessie magnetometer wordt doorgaans toegepast om het scalaire veld te meten. Tegenwoordig worden ruimtevaartuigen steeds kleiner, wat strenge eisen oplegt aan de afmetingen, het gewicht en de vermogensopname van de toegepaste magnetometer. Kleine optisch gepompte scalaire magnetometers gebaseerd op micro gascellen, bezitten de vereiste gevoeligheid en hebben bovendien de andere vereiste eigenschappen. Kleine vector magnetometers zoals micro fluxgates bezitten niet de vereiste gevoeligheid.

Andere vector sensoren zoals Hall sensoren of "gigantische magneto weerstanden" (GMR) zijn klein, lichtgewicht en hebben een lage vermogensopname, maar bezitten ook niet de gewenste gevoeligheid. De gevoeligheid kan worden ver-

beterd door fluxconcentratie toe te passen door middel van een hoge-T_c fluxconcentrator. Deze hybride apparaten zijn ontwikkeld met bismuth (Bi) Hall sensoren en GMRs en laten veelbelovende gevoeligheden zien. De integratie van half- en supergeleiders zoals een gedoteerd silicium (Si) Hall element met een hoge-T_c flux concentrator wordt gezien als een mogelijkheid voor een verdere verbetering van de gevoeligheid, wat deze sensoren geschikt maakt voor ruimtevaarttoepassingen.

Magnetisch veld sensoren die worden toegepast in een niet afgeschermde omgeving en die geconstrueerd zijn uit supergeleidende films, zoals bijvoorbeeld SQUIDs en hybride magnetometers, kunnen hoge $1/f$ ruis karakteristieken vertonen. Deze ruis wordt veroorzaakt door de thermisch geactiveerde beweging van ingevangen flux vortices in het supergeleidende deel. Door dit te verdelen in dunne strips wordt deze ruis onderdrukt, doordat de strips een kritisch veld hebben waar beneden geen vortices worden gevangen.

Theoretische modellen uit de literatuur voor het kritische veld van dunne film supergeleidende strips lieten geen goede overeenstemming zien met de beschikbare experimentele data. Een nieuw theoretisch model voor het kritisch veld is opgesteld, waarbij de paarenergie van een vortex anti-vortex paar wordt meegenomen. Of een vortex nu wel of niet wordt ingevangen, wordt bepaald door de Gibbs vrije energie. Deze energie heeft een minimum in het centrum van de strip als een veld wordt aangelegd boven een bepaalde kritische waarde. In het model dat gepresenteerd wordt in dit proefschrift wordt aangenomen dat de diepte van de resulterende energiebarrière even groot is als de energie die het kost om een vortex anti-vortex paar te creëren. Doordat deze energie en de Gibbs vrije energie dezelfde temperatuurafhankelijkheid hebben, heffen materiaaleigenschappen zoals de Pearl-lengte en de coherentielengte elkaar op. De resulterende uitdrukking laat alleen een breedte afhankelijkheid zien. Door een kleine modificatie van de Gibbs vrije energie zoals deze in de literatuur beschreven staat was het mogelijk om direct een uitdrukking af te leiden voor de vortex dichtheid boven het kritische veld.

Directe experimentele tests met een scannende SQUID microscoop (SSM) op $YBa_2Cu_3O_{7-\delta}$ (YBCO) en niobium (Nb) strips lieten een goede overeenstemming zien tussen waarden van het kritisch veld model en de metingen. Omdat er geen verschil in het kritisch veld tussen Nb en YBCO werd waargenomen, kan de conclusie worden getrokken dat het kritisch veld niet materiaalafhankelijk is. Metingen aan de vortexdichtheid boven het kritisch veld waren redelijk in overeenstemming met het model. Naast de dichtheid is ook de verdeling statistisch geanalyseerd. Vanuit het oogpunt van toepassing in een sensor is dit minder relevant, omdat vortices ongewenst zijn. De analyse geeft echter inzicht in de defecten in het materiaal. Voor relatief lage inducties bevinden de vortices zich in het centrum van de strip en voor hogere inducties in twee parallelle rijen. Het veld waarbij de overgang van een enkele rij naar twee parallelle rijen plaatsvindt is in overeenstemming met waarden uit de literatuur. Verder is de verdeling in Nb strips homogener in de longitudinale richting. Tevens is de spreiding rond het centrum kleiner in de laterale richting. Dit duidt erop dat de YBCO strips meer en ernstigere defecten bevatten vergeleken met Nb.

De resultaten van het onderzoek naar ingevangen vortices in dunne-film su-

pergeleidende strips zijn toegepast op de concentrators van de hybride magnetometers. Een theoretisch model is afgeleid waarmee de sensor, de concentrator en de combinatie van deze twee kan worden geoptimaliseerd. Als sensor is een gedoteerd Si Hall-element beschouwd. In vergelijking met eerder werk met Bi-Hall elementen kan gedoteerd Si veel hogere Hall coëfficiënten hebben. Parameters zoals de ladingsdragerdichtheid en mobiliteit versus de temperatuur zijn onderzocht. Verschillende doteringen zijn vergeleken en een optimale dopingdichtheid is verkregen, waarbij gelet is op de resulterende gevoeligheid en de weerstand. Een ontwerp met een tweetal concentrators is beschouwd omdat dit resulteert in een betere koppeling naar de sensor in vergelijking met een ontwerp waarbij één concentrator wordt gebruikt. In het geval van een situatie met een tweetal concentrators is de afschermstroom in één van de concentrators lager omdat de hoeveelheid flux die wordt verzameld kleiner is. Hierdoor kan de breedte van de constrictie beperkt worden. Dit resulteert in een betere koppeling naar de sensor. De totale oppervlakte van het apparaat welke is geplaatst op een 1×1 cm^2 substraat is constant gehouden. In het geval van een ontwerp met twee concentrators betekent dit dat de concentrators rechthoekig moeten zijn. In de literatuur werden geen analytische uitdrukkingen voor de inductie en het effectieve oppervlak gevonden. Daarom zijn deze eigenschappen bepaald met eindige elelementen simulaties. Om de simulaties te testen zijn deze ook toegepast op vierkante concentrator ontwerpen, waar wel analytische uitdrukkingen voor bestaan. Een vergelijking liet een goede overeenstemming tussen het theoretisch model en simulatie zien.

Het fabricage proces van hybride magnetometers omvat over het algemeen welbekende technieken. Sommige van de minder triviale productiestappen zijn beschreven in dit proefschrift. Voor de Bi hybride magnetometer is het RF-sputteren van Bi onderzocht. Ongeacht de depositiecondities waren de films redelijk ruw, wat in principe niet direct een probleem is zolang maar een gesloten stroompad gerealiseerd kan worden. Een optimalisatiestudie naar de optimale depositie condities is uitgevoerd waar parameters zoals de substraattemperatuur, sputtervermogen en de procesdruk uitgebreid zijn gevarieerd. Visuele inspectie met een scannende electronenmicroscoop (SEM) laat zien dat tussen 373 K en 388 K een duidelijke verandering van de groei optreedt. Electrische karakterisering laat zien dat de beste films, met de hoogste Hall-coëfficiënt, bij een temperatuur van 388 K verkregen werden. De gevonden waarden corresponderen redelijk met waarden die te vinden zijn in de literatuur, waar andere depositietechnieken gebruikt zijn.

De implantatie van dotering in Si en de groei van YBCO op Si zijn onderzocht voor toepassing in gedoteerd Si hybride magnetometers. Deze sensoren worden geconstrueerd op "silicium op isolator" (SOI) substraten. Dit heeft als voordeel dat bij de implantatie een goed gedefinieerd en homogeen gedoteerd gebied kan worden gecreëerd en dat bij de depositie de thermische spanning, veroorzaakt door grote verschillen in de thermische uitzettings coëfficiënten tussen Si en YBCO, kan worden opgevangen in de SiO_2 tussenlaag.

Door middel van simulaties zijn de optimale dosis en versnelspanning voor implantie bepaald. Om een versnelspanning te kunnen gebruiken die in het bereik

het ionimplantatieapparaat ligt is een SiO_2 film op het SOI substraat gesputterd voor de implantatie. Er zijn substraten geïmplanteerd met arseen (As) en boor (B). De gesputterde SiO_2 laag bleek transparanter te zijn dan verwacht op basis van de simulaties. De As dotering was te hoog en de B dotering te laag, zelfs zo laag dat electrische karakterisering niet mogelijk was. Desalniettemin was de Hall-coëfficiënt van de met As gedoteerde substraten met suboptimale implantatie parameters een factor 2–4 hoger dan die van de Bi Hall-sensoren.

YBCO films zijn op SOI wafers gegroeid door middel van gepulste laser depositie. Yttrium gestabiliseerd zirconium oxide (YSZ) en CeO_2 films zijn gebruikt als bufferlagen om de juiste groeioriëntatie en roosterconstante te introduceren en om diffusie van zuurstof te voorkomen. Het was mogelijk om films van een goede kwaliteit te deponeren die kritische temperaturen en stroomdichtheden hadden die vergelijkbaar zijn met resultaten uit de literatuur. Doordat de SOI substraten een toplaag van 50 nm hadden, wat heel dun is, trok de Si laag krom. Door de dikte van de bufferlaag te beperken, was het mogelijk om dit te voorkomen.

Zoals gezegd kan de gevoeligheid van een Hall-element verbeterd worden door fluxconcentratie toe te passen. Echter, de resolutie van het apparaat kan beperkt worden door ruis die wordt veroorzaakt wordt door de beweging van vortices. Deze ruis is afgeleid en vergeleken met de intrinsieke ruis van de Hall sensor. De $1/f$ ruis van YBCO films is experimenteel bepaald en beschreven in verschillende artikelen. De spectrale ruis term uit de literatuur is gesubstitueerd in het afgeleide model. Wanneer er sprake is van films van een hoge kwaliteit gedeponeerd op goed passende substraten is de ruis door vortices in principe niet dominant. De ruis van YBCO films op SOI substraten is nooit experimenteel bepaald. Hoewel het waarschijnlijk is dat de ruis hiervan hoger is dan van de eerder genoemde films, is het niet waarschijnlijk dat de ruis in deze films zal domineren.

Hybride magnetometers met Bi Hall-elementen zijn gekarakteriseerd. Verschillende ontwerpen, met en zonder sleuven in de concentrator, zijn gerealiseerd. Naast de karakteristieke waarden, lieten metingen aan de apparaten met de sleuven additionele artefacten zien, die toegeschreven kunnen worden aan de strips in de concentrator. In vergelijking met eerder werk worden niet de karakteristieke waarden uit de literatuur gehaald. Dit kan worden toegeschreven aan een lagere Hall coëfficiënt en voor het grootste deel aan een zwakke koppeling tussen Hallsensor en concentrator. Het apparaat wat in dit proefschrift wordt beschreven heeft echter een veel groter maximaal veld met een bredere constrictie wat de zwakkere koppeling veroorzaakt.

De karakterisering van gedoteerde Si hybride magnetometers is belemmerd door moeilijkheden bij het maken van contacten naar de Hall-sensor. Contact met de sensor wordt gerealiseerd door middel van contactgaten die met Ar-ionetsen worden gemaakt. Waarschijnlijk wordt het Si door het etsen beschadigd en een klein deel aan het oppervlak wordt amorf. Dit resulteert in extreem hoge contactweerstanden, die de werking van het apparaat belemmeren. Om dit te voorkomen moet er gezocht worden naar een andere manier om contact te maken met de sensor. Tevens is het wellicht mogelijk om het gedoteerde gedeelte te contacteren voordat de concentrator gedeponeerd wordt.

Dankwoord

(Acknowledgements)

Het onderdeel van het proefschrift wat u nu voor zich heeft is, zonder enige twijfel, verreweg het meest gelezen gedeelte. Met het schrijven van dit dankwoord besef ik dat er een einde komt aan een periode van iets meer dan 4 jaar bij de vakgroep lage temperaturen. Het moment is dan ook aangebroken om nog eens met veel plezier op deze vier jaar terug te kijken en te concluderen dat ik hier een geweldige tijd heb gehad. De ontspannen sfeer, gezellige momenten bij de koffietafel en de collegialiteit hebben er voor gezorgd dat ik vier jaar lang met plezier aan het werk ging. Ik wil iedereen van de vakgroep lage temperaturen bedanken voor deze geweldige tijd. Een aantal mensen dien ik echter in het bijzonder te noemen.

Horst en Jaap, bedankt dat jullie mij de mogelijkheid hebben gegeven om dit onderzoek uit te voeren. Jaap, je dagelijkse begeleiding was een grote steun in de rug. Onze uitgebreide besprekingen hebben me vaak net het zetje in de juiste richting gegeven.

John it has been a great honor to be able to work with you. Without a doubt this thesis would not have looked the same without your input. I found our collaboration very inspiring and I learned a lot from you. Often people ask me if the B_{K} critical field is named after me and I have to admit that it should be accredited to you. It has been great fun working with your SSM when it was still operational and I'm sure it will be very usefull to our group now it is working again.

Een groot woord van dank gaat ook uit naar het ondersteunend personeel. Dick en Frank, de manier waarop jullie het lab draaiende weten te houden is

bewonderenswaardig. Voor praktische vraagstukken was een bezoekje aan jullie kamer altijd erg nuttig en daarbij ook nog gezellig. Dick, ik vond onze Japan experience voor en na de ISEC 2009 conferentie geweldig. Het was af en toe een beetje gestoei met Japanse navigatie systemen, hotel kamers zonder bedden, en het protocol voor het nemen van een bad maar dan heb je tenminste het gevoel dat je er echt bent geweest. Een woord van dank ook voor Ans en Inke voor de secretariële ondersteuning en Harry voor de vele liters vloeibaar helium.

Een aantal studenten hebben meegewerkt aan dit project en een woord van dank aan allen ben ik verschuldigd. Wolter Hoving heeft tijdens zijn afstudeerproject de eerste ontwerpen van hybride magnetometers gemaakt en de eerste metingen gedaan. Wiemer van de Veur en Cor Molenaar hebben tijdens hun bachelorproject samen met John Kirtley gewerkt aan de eerste SSM metingen van dunne strips. Het resultaat hiervan heeft bijgedragen aan een publicatie in Physical Review B. Bob Rots heeft voor zijn stage zich bezig gehouden met Bi depositie. Wilco Vessies en Michael Garcia hebben tijdens hun bachelorproject gekeken of het mogelijk is om de koppeling tussen de concentrator en het Hall-element te vergroten. Yves Lionet is voor zijn stage bij ons gekomen en heeft gewerkt aan de optimalisatie van YBCO groei op SOI wafers. Wilco van der Camp en Sebastiaan Waanders hebben in hun bacheloropdracht simulaties en metingen verricht aan gedoteerde SOI wafers. Het werk van Yves, Wilco en Sebastiaan heeft bijgedragen aan een publicatie in Superconducting Science and Technology. Wiemer vond het na zijn bachelorproject nog niet genoeg en hij werkt op dit moment in zijn afstudeeronderzoek aan de gedoteerde Si hybride magnetometers. Wiemer, ik heb er alle vertrouwen in dat het gaat lukken en dat je alle onderdelen van het onderzoek weet samen te voegen tot een werkend device. Heel veel succes!

Een woord van dank gaat ook naar mijn kamergenoten, Johannes, Martin, Reinder en sinds kort de nieuwste aanwinst van de groep: Cor. Johannes, afgezien van het feit dat je nogal snurkt was het gezellig om met jou verschillende conferenties te bezoeken. Het hoogtepunt was denk ik wel de ASC 2008 in Chicago. Ons roadtripje aansluitend was kort maar krachtig. Het was flink ver rijden maar dat is niet echt een straf in Amerika. Met de boot onder de Niagara watervallen en slenteren door Manhattan was zeer de moeite waard. Ik heb ervan genoten! Aico, Mark, Jeroen, Maarten, Joost, Vedran, Joska, Kees, Sybolt, Aleksandar, Alexander, Ariando, Karthi, Sander, Bernard, Marcel, Pieter, Hendrie, Harald, Hans, Gerard, Menno en alle andere AIO's, postdocs en vaste staf, bedankt voor de gezelligheid tijdens en na werktijd. Sybolt, hartelijk dank dat we bij jou de start van de tweede etappe van de Vuelta mochten bekijken, betere plekken waren er niet. Alexander, ik hoop dat we volgend jaar weer een schaatstochtje kunnen maken, het begint al een traditie te worden. Jeroen, hartelijk dank voor je hulp bij de cover. Het is dan wel geen 3D maar ik kan wel zeggen dat ik een echte Huijben op de cover heb. Joost, hartelijk dank dat je er 's ochtends al vroeg was voor een bakje koffie.

Voldoende ontspanning in de weekenden is tijdens een promotieonderzoek noodzakelijk en hiervoor zijn vrienden, familie en schoonfamilie heel erg belangrijk. Peter en Wietse, met jullie op vakantie en de kroeg onveilig maken was elke keer weer

een avontuur. Ik hoop dat we dat nog vaak gaan doen. Het is een eer dat jullie mijn paranimfen willen zijn. Maarten, na dit schaatsseizoen weet ik het zeker: er komt een dag dat we de elfstedentocht kunnen schaatsen. Ik hoop dat we de komende zomer flink wat kilometers op de nieuwe fietsen kunnen maken, ik heb er nu al zin in. Ik vond het geweldig om je paranimf te zijn. Met Marieke kreeg ik er ook nog een vriendengroep gratis bij. Marieke L, Frank, Nadine, Nico, Leonie, Maarten H, Jorien, Matthijs, Martijn, hartelijk dank voor de gezellige momenten bij Murphys.

Pap en mam, hartelijk dank voor al jullie steun. Jullie hebben me altijd de mogelijkheid gegeven om te doen wat ik leuk vond en wat mij het beste leek. Door jullie heb ik altijd de motivatie gevonden om door te zetten en mijn doel te bereiken. Af en toe keken jullie wel een beetje glazig als ik weer eens uitweidde over de wondere wereld van flux vortices die gevangen zitten in dunne film supergeleidende stripjes maar zonder jullie was dit werk er niet gekomen. Dit proefschrift is voor jullie!

En dan rest het om nog één iemand te bedanken, mijn allerliefste Marieke. Bedankt voor al je steun en je onvoorwaardelijke liefde. Het was bijzonder prettig om na een dag werken aan dit proefschrift bij je thuis te komen, te horen over de kinderen in je klas, en aan iets anders te kunnen denken dan aan wetenschap. Daar heb jij voor gezorgd! Na het voltooien van dit proefschrift breekt er een nieuwe fase aan in ons leven. We zijn natuurlijk al gaan samenwonen en binnenkort vinden we hopelijk allebei een nieuwe baan. Ik heb er heel veel zin in, en ik ben heel benieuwd wat de toekomst ons zal brengen. De wereld ligt aan onze voeten!

Kristiaan Kuit
Enschede, maart 2010